

PEDRO SIMÕES COSTA

INTERFACE-RESOLVED SIMULATIONS OF DENSE
TURBULENT SUSPENSION FLOWS

**INTERFACE-RESOLVED SIMULATIONS OF DENSE
TURBULENT SUSPENSION FLOWS**

PROEFSCHRIFT

ter verkrijging van de graad van doctor
aan de Technische Universiteit Delft,
op gezag van de Rector Magnificus prof. ir. K.C.A.M. Luyben,
voorzitter van het College voor Promoties,
in het openbaar te verdedigen op dinsdag 19 December 2017 om 15:00 uur

door

Pedro SIMÕES COSTA

Mestre em Engenharia Mecânica
Universidade Técnica de Lisboa – Instituto Superior Técnico
geboren te Lissabon, Portugal.

Dit proefschrift is goedgekeurd door de promotors:

Promotor: prof. dr. ir. J. Westerweel

Promotor: prof. dr. ir. B. J. Boersma

Copromotor: dr. ir. W.-P. Breugem

Samenstelling promotiecommissie:

Rector Magnificus,	voorzitter
prof. dr. ir. J. Westerweel,	Technische Universiteit Delft
prof. dr. ir. B. J. Boersma,	Technische Universiteit Delft
dr. ir. W.-P. Breugem,	Technische Universiteit Delft

Onafhankelijke leden:

prof. dr. dipl.-ing. A. Soldati,	Technische Universität Wien
prof. dr. J. G. M. Kuerten,	Technische Universiteit Eindhoven
prof. dr. ir. W. S. J. Uijtewaal,	Technische Universiteit Delft
prof. dr. ir. C. Vuik,	Technische Universiteit Delft

This research was supported by the Portuguese Foundation for Science and Technology, under the grant SFRH/BD/85501/2012.

Cover by: Alexis Ierides

Printed by: Gildeprint - Enschede

Copyright © 2017 by P. Costa, all rights reserved

ISBN 978-94-92516-99-2

An electronic version of this dissertation is available at
<http://repository.tudelft.nl/>.

to my mother Lina

CONTENTS

SUMMARY	ix
SAMENVATTING	xi
1 INTRODUCTION	1
1.1 Background	2
1.2 Objectives and strategy	12
1.3 Outline	14
2 METHODS	15
2.1 Governing equations	16
2.2 Navier-Stokes solver	17
2.3 Immersed-boundary method	18
2.4 Short-range particle-particle and particle-wall interactions	21
2.5 Computational implementation and parallelization	22
2.5.1 Fluid flow solver	22
2.5.2 Particle treatment	25
2.5.3 Applicability of our method	32
2.5.4 Validations and scaling performance	32
2.5.5 Benchmark – numerical simulation of particle-laden decaying homogeneous isotropic turbulence	35
3 COLLISION MODELING	43
3.1 Introduction	44
3.2 Dry collisions	47
3.2.1 Physics	47
3.2.2 Modeling	50
3.3 Effects of the interstitial fluid	54
3.3.1 Lubrication effects	54
3.3.2 Piezoviscous effects	57
3.4 Numerical implementation	57
3.5 Results from collision simulations	59
3.5.1 Bouncing motion of a solid sphere colliding onto a planar surface in a viscous liquid	59
3.5.2 Wet head-on collisions	62
3.5.3 Oblique collisions	65
3.6 Conclusions and outlook	67
4 SCALING LAWS FOR DENSE PARTICLE SUSPENSIONS IN WALL-BOUNDED TURBULENCE	69
5 FINITE-SIZE EFFECTS IN TURBULENT SUSPENSION TRANSPORT	81

5.1	Introduction	82
5.2	Computational setup	84
5.3	Results	85
5.4	Conclusions and outlook	105
6	CONCLUSIONS & FUTURE PERSPECTIVES/OUTLOOK	107
6.1	Conclusions	108
6.2	Outlook	110
	REFERENCES	115
	ACKNOWLEDGMENTS	127
	CURRICULUM VITÆ	129
	LIST OF PUBLICATIONS	131

SUMMARY

Transport of particles by a carrier fluid is an important, ubiquitous process. Few of many obvious examples are the blood flow that feeds oxygen to the different parts of our bodies, wind-assisted pollination, sediment transport in sand storms, avalanches, or rivers, cloud formation, and pyroclastic flows. In industry one can think of the flocculation/sedimentation processes in the treatment of drinking water, circulating fluidized bed reactors, sediment transport in land reclamation works, and more.

The scientific community has been studying particle-laden turbulent flows, mostly for cases where the flow is dilute and the particles are very small. For dense flows laden with *finite size* particles – particles with a size larger than the smallest turbulent scales – some basic, and yet very important questions remain unanswered. Questions like: ‘*in a turbulent suspension flow of finite size particles with given set of properties, what is the power required to sustain the flow?*’ and ‘*Where do particles tend to accumulate?*’.

The present work seeks to extend the current fundamental knowledge of these flows with original results for a complex, and yet quite idealized case: turbulent channel transport of dense, neutrally-buoyant finite size spheres. The mathematical properties of the governing equations for this system require massively-parallel numerical simulations for achieving the three-dimensional and time-resolved detail, necessary to shed light on the research questions postulated above.

This thesis is divided in two parts. The first part deals with the development and validation of a numerical algorithm capable of performing state-of-the-art numerical simulations of dense turbulent transport of finite size particles. In the second part, results from numerical simulations are presented to understand the dynamics of turbulent channel transport of finite size particle suspensions.

The starting point was the second-order immersed-boundary method (IBM) described by Breugem [18]. We implemented a new parallelization strategy that increased the computational performance to such an extent so that high-fidelity numerical simulations with $\mathcal{O}(10^9)$ Eulerian grid cells and $\mathcal{O}(10^6)$ finite size particles were possible. We also developed a method for short-range particle-particle and particle-wall interactions, improved the model for lubrication interactions, and incorporated a simple, yet realistic, model for oblique particle-particle/-wall collisions. Three types of inter-particle interactions are taken into account: (1) long- and (2) short-range hydrodynamic interactions, and (3) solid-solid contact. The collision model was validated against several benchmark experiments.

We performed simulations of turbulent suspension transport. Our results allowed us to extend well-know scaling laws for the mean velocity and overall drag as a function of the flow governing parameters, derived by von Kármán and Prandtl in the 1920s for single-phase turbulent flow, to the case of a finite size particle suspension. The key is to split

the suspension flow into two regions: the core region where it behaves like a fluid with an effective viscosity higher than that of the suspending fluid, and a thin *particle-wall layer* along each wall. In the particle-wall layer, particles highly influence the distribution of wall shear stresses. This is characterized by extreme events (both much higher and much lower than the mean). Based on these observations we provide a scaling for the particle-to-fluid slip velocity as a function of the flow governing parameters. In regard to particle dispersion, single-point dispersion is dominated by particle-turbulence (and not particle-particle) interactions, while differences in two-point dispersion and collisional dynamics are consistent with a picture of shear-driven interactions.

SAMENVATTING

Het transport van deeltjes door een vloeistof is een belangrijk en veel voorkomend proces. Enkele van de duidelijke voorbeelden zijn de bloedstroom die zuurstof vervoert naar verschillende delen van ons lichaam, door de wind gedreven bestuiving, sediment transport in zandstormen, grondverschuivingen, of rivieren, de vorming van bewolking en een pyroclastische stroom. In de industrie kan men denken aan flocculatie/sedimentatieprocessen in drinkwaterzuivering, het circuleren van een gefluïdiseerde-bed-reactor, sediment transport voor landaanwinning, enzovoorts.

De wetenschappelijke gemeenschap heeft turbulente stromingen geladen met deeltjes met name bestudeerd in het geval dat de stroming verdund is en de deeltjes zeer klein zijn. Voor geconcentreerde stromingen geladen met deeltjes met een eindige grootte – deeltjes met een afmeting groter dan de kleinste turbulentieschalen – blijven een aantal basale, maar zeer belangrijke vragen onbeantwoord. Vragen zoals: *‘Wat is de energie die nodig is om een stroming van een turbulente suspensie met deeltjes van een eindige grootte met een gegeven set aan eigenschappen voort te blijven stuwten?’* en *‘Waar neigen deeltjes te accumuleren?’*

Het huidige werk zoekt naar het vergroten van de huidige fundamentele kennis van dit soort stromingen door middel van originele resultaten voor een complexe, maar alsnog tamelijk geïdealiseerde casus: turbulent transport van een hoogbeladen suspensie van bolletjes met een neutraal drijfvermogen in een kanaal. De mathematische eigenschappen van de geldende vergelijkingen van dit systeem vereisen intensieve parallele numerieke simulaties om het driedimensionale en tijd opgeloste detail te bereiken dat nodig is om een licht te werpen op de onderzoeksvragen die hierboven zijn geformuleerd.

Dit proefschrift bestaat uit twee delen. Het eerste deel behandelt de ontwikkeling en validatie van een numeriek algoritme dat in staat is om de modernste numerieke simulaties van geconcentreerd turbulent transport van deeltjes met een eindige grootte uit te voeren. In het tweede deel worden de resultaten van numerieke simulaties gepresenteerd, met als doel het dynamisch gedrag van het turbulente transport van suspensies van deeltjes met een eindige grootte in een kanaal te begrijpen.

Het startpunt was een tweede-orde nauwkeurig Immersed Boundary Method (IBM), beschreven door Breugem [18]. We hebben een nieuwe parallellisatiestrategie geïmplementeerd die de rekenprestatie dusdanig heeft verbeterd dat accurate numerieke simulaties met $\mathcal{O}(10^9)$ Euleriaanse roostercellen en $\mathcal{O}(10^6)$ deeltjes met eindige grootte mogelijk zijn. We hebben ook een methode ontwikkeld voor de deeltje-deeltje en deeltje-wand interactie op korte afstand, het model voor lubricatie-interacties verbeterd, en een simpel maar realistisch model voor deeltje-deeltje/-wand botsingen onder een hoek geïncorporeerd. Drie typen interacties tussen deeltjes worden daarbij meegenomen: (1) lange-

en (2) korteafstandsinteracties van hydrodynamische aard, en (3) direct contact tussen vaste deeltjes. Het botsingsmodel is geverifieerd ten opzichte van een aantal referentie-experimenten.

We hebben simulaties gedaan van turbulent transport van hoogbeladen suspensies. Onze resultaten hebben ons in staat gesteld om bekende schalingswetten voor de gemiddelde snelheid en de algehele weerstand als functie van stromingsgerelateerde parameters, afgeleid door von Kármán en Prandtl in de jaren 1920 voor éénfasige turbulente stroming, uit te breiden naar de casus van een suspensie met deeltjes van eindige grootte. Dit is gedaan door de suspensiestroming in twee gebieden op te delen: de kern, waar de stroming zich gedraagt als een vloeistof met een effectieve viscositeit hoger dan die van de suspensievloeistof, en een dunne deeltjes-wandlaag langs elke wand. In de deeltjes-wandlaag hebben deeltjes een grote invloed op de verdeling van de afschuifspanningen op de wand. Dit wordt gekarakteriseerd door extreme gebeurtenissen (zowel veel hoger als veel lager dan het gemiddelde). Op basis van deze observaties stellen we een schaling op voor de gemiddelde slipsnelheid tussen de deeltjes en de vloeistof als functie van de geldende stromingsparameters. Met betrekking tot de dispersie van deeltjes is de eenpuntdispersie gedomineerd door deeltjes-turbulentie (en niet deeltje-deeltje) interacties, terwijl verschillen in de tweepunts-dispersie en botsingsdynamica consistent zijn met het beeld van afschuiving-gedreven interacties.

INTRODUCTION

1.1 BACKGROUND

PARTICLE-LADEN TURBULENT FLOWS

Panta rhei. This expression, attributed to the Greek philosopher Heraclitus (535-475 BC), translates in English to *everything flows*, and intends to convey the idea that oneself and the rest of the world is in continuous change:

We both step and do not step in the same rivers. We are and are not.¹

We borrow this expression in a less philosophical sense and shape it to the purpose of this introduction: *anything can flow*, provided that there is a driving force capable of making the *thing* – matter – flow.

In the present work we consider particle-laden fluid flows. Particles – portions of matter much smaller than the overall physical system of interest – travel in a carrier fluid, also in motion. The system at stake is in a turbulent state, exhibiting both chaotic and multiscale dynamics.

These flows are ubiquitous in nature. After all, turbulent is the natural state of most of the flows present in nature². Few of many popular examples are sediment transport in rivers, sandstorms, pyroclastic flows, slurry transport in land reclamation processes, and the flocculation and sedimentation processes in the treatment of drinking water, see figure 1.1. These examples and many others share two characteristics that are explored here. First, the flow can be dense, meaning that the volume fraction of particles is sufficiently high that particle-particle interactions are dynamically significant; and second, the particles can have a *finite size*, about the same size or larger than the smallest relevant length scale of the fluid flow (e.g., the Kolmogorov microscale [82]).

In this case turbulence – as an unsolved problem of classical physics – is tightly coupled to the particle dynamics, modifying and being modified by it. This results in a complex problem, with an unbalance between the limited fundamental knowledge of its physics, and its ubiquitous character.

It is imperative that we continuously improve our fundamental knowledge on particle-laden flows. In industry, engineers strive to develop more efficient and sustainable processes. Moreover, we would like to be able to anticipate potential natural disasters, and once they cannot be avoided, to minimize the potential natural hazard. Think, for instance, about our capacity for predicting where human waste tends to accumulate in the ocean, or of how the ashes from a volcanic eruption will disperse in space and time, and where they can be hazardous to airline flights. Such predictions are inherently difficult to make, requiring a significant amount of data, computing time, and a great deal of modeling. These are impossible to make without some level of fundamental understanding of particle-laden flows.

¹ DK B49a (Diels-Kranz collection of Presocratic sources)

² At least at scales that the human eye can see.

There is a kaleidoscope of possible effects of particles on turbulence, and reciprocally of turbulence to particle dynamics. Particles may vary in shape, size and physical/chemical properties; the fluid can be non-Newtonian and the flow/particle dynamics influenced by external fields (e.g. gravitational or magnetic). One can think of many more parameters inspired by real applications that make the flow even more complex. Taking all these into account at once in a specific problem makes it difficult to disentangle the fundamental role that each parameter takes in the flow physics. In the framework of this thesis we will consider particles that are of finite size, non-Brownian³, spherical, rigid, homogeneous, and isotropic. As we will see, even in this “simplified” case there is a wide range of regimes that are still subject of active research, and with practical applications⁴.

Here we focus on *dense turbulent suspensions*. The attributes *dense* and *turbulent* impose respectively lower and upper bounds in the volume fractions that are considered. Dense implies that the concentration of particles is sufficiently high such that particle-fluid and particle-particle interactions are dynamically significant; turbulent obviously implies that the flow is in a turbulent state. Consequently, the solid volume fraction cannot be too high. Otherwise, turbulent coherent structures are completely destroyed by particle collisions and the rigidity constraint of the zero rate-of-strain that the particle boundaries impose on the flow dynamics. We therefore do not consider the more extreme values of solid volume fraction typical of a granular flow. More qualitatively, apart from relatively high flow Reynolds number, we require that the Bagnold number $Ba = 4Re_p\sqrt{\lambda}$ – a ratio between inter-particle inertial to viscous forces – is small enough. $\lambda = 1/(\Phi_{max}/\Phi)^{1/3} - 1$ is the linear concentration, $\Phi_{max} = 0.74$ and Re_p a particle Reynolds number defined from the particle radius, local shear rate and fluid viscosity. The range of Bagnold numbers that we consider are typically in the range $40 < Ba < 450$ [5, 85].

TURBULENCE MODULATION BY THE PRESENCE OF PARTICLES

Noticeable changes in the turbulence dynamics require a dynamically significant number of particles. Three main coupling regimes are often considered, depending on the volume fraction ($\Phi = V_s/(V_f + V_s)$) and mass fraction ($\Psi = M_s/(M_f + M_s)$) of solid particles in the flow, with V and M denoting total mass and volume, respectively, and the

³ Typically with diameter $D_p \gtrsim 1\mu\text{m}$.

⁴ Here is an example. Consider sediment transport for land reclamation in the dredging industry (figure 1.1 (d)), a very important activity in The Netherlands. Here, characteristic velocities are of the order of 5m/s, flowing through a suction pipe with a diameter of about 1m. Considering the kinematic viscosity of water at the range of temperatures at stake (about 10°C) equal to $\nu = 10^{-6}\text{m}^2/\text{s}$, and a solid volume fraction of 40%, we get a Reynolds number based on the pipe diameter and effective suspension viscosity [133] of $Re_D \approx 10^5$. Estimating the Kolmogorov length scale in the bulk from the viscous wall unit $\eta \sim DRe_D^{-7/8}$ (assuming a friction factor $f \sim Re_D^{-1/4}$) we get a value of $\eta \approx 0.04\text{mm}$, much smaller than the characteristic size of the sediments that are being transported $D_p \sim 0.1\text{mm}$ [60].



Figure 1.1: Practical examples of sediment transport: (a) pyroclastic flow from the Mayon Volcano, Philippines, 1984 (source: volcanoes.usgs.gov); (b) aeolian flow in a crest in the Kelso Dunes in the Mojave Desert, California (source: wikipedia.org); (c) channeling due to the erosion in a river flow in the Toklat River, Alaska (source: flickr.com); (d) sediment discharge in land reclamation (d) (source: dragadoinfra.com).

subscripts s and f denoting 'solid' and 'fluid', respectively. In this context, low Φ and Ψ correspond to a regime where the global particle inertia is so small that the turbulence dynamics is hardly modified by their presence, and the volume fraction of particles so small that particle-fluid and particle-particle interactions are negligible. This is the so-called *1-way coupling* regime, where particle dynamics is influenced by the turbulence dynamics but the reciprocal influence is negligible. Increasing Ψ for fixed Φ (e.g., by considering the same amount of particles in a lighter fluid) will eventually result in a regime where the overall particle inertia becomes dynamically significant in turbulence modulation, while particle-particle interactions are still unlikely. In this regime particle dynamics modulate the turbulence, and vice-versa (hence called *2-way coupling*). Finally, increasing Φ will eventually result in a regime where all the previous interactions are important, plus particle-particle interactions: the so-called *4-way coupling* regime. Of course, choosing the modeling strategy to study these flows requires considering the type of coupling regime. These regimes and the associated nomenclature were introduced in [41], where a schematic like figure 1.2 is made. We note that the ratio of particle-to-turbulence response times τ_p/τ_η presented along the vertical axis can be expressed in terms of the particle mass fraction, and particle-to-fluid density ratio, large scale turbulent Reynolds number Re_L , and particle-to-turbulence size ratio D/L .

In figure 1.2 particle size and density influence the coupling regime similarly. But when it comes to developing a modeling strategy, large particles, which interact directly with flow scales, are more challenging.

MODELING STRATEGIES FOR TURBULENT DISPERSED MULTIPHASE FLOWS

The modeling approach depends, first of all, on the level of detail that is required, i.e., on which scales to resolve. Fully-resolved simulations compute the flow up to the smallest scale – the *microscale*. By definition, this approach requires no closure models for unresolved terms, often at the price of a large computational demand⁵.

At present, interface-resolved simulations of particulate turbulent flows are limited to $O(10^5 - 10^6)$ particles and relatively low Reynolds numbers, albeit many realistic applications deal with much higher figures. Predicting such large systems requires methods for resolving scales down to a certain threshold, while modeling the spectrum of unresolved scales. In this spirit, if information beyond the largest scales is required, while resolving all the scales is unfeasible, one can resort to *macroscopic* models. In these models, a volume-averaging procedure is typically applied to the governing equations, thereby deriving a system of equations for conservation of mass and momentum of the mixture. Two types of unclosed terms emerge from such averaging procedure. First, as in single-phase flows, a subgrid-scale stress term. Second, terms related to exchange of momentum between

⁵ Hence denoted by some researchers in the field of kinetic models for multi-phase flows (private communication with the author) as the *brute-force* approach.

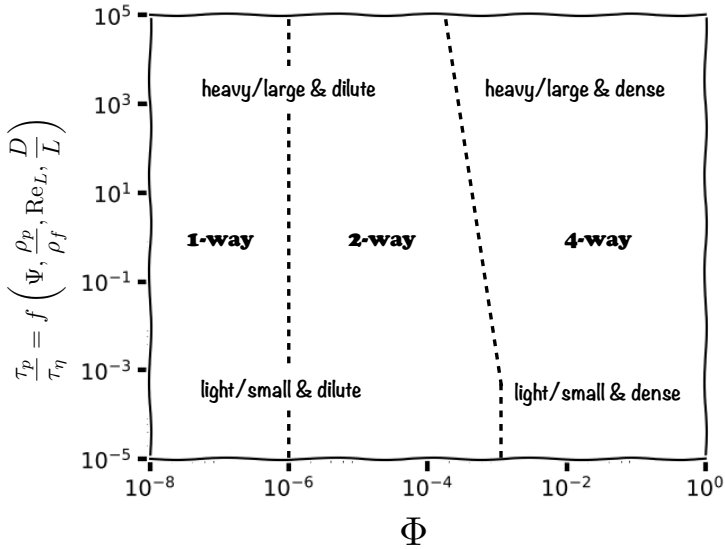


Figure 1.2: Coupling regimes as described in [41]. τ_p/τ_η increases monotonically with any of the following parameters: Ψ , ρ_p/ρ_f , D_p/L or Re_L , with L being the turbulence integral scale, and Re_L the Reynolds number based on the large turbulence scales. For a very dilute system, particles hardly influence the flow dynamics; only the flow dynamics influence the particles. Increasing the volume fraction for fixed τ_p/τ_f results in a stronger coupling: first 2-way and ultimately 4-way. The heavier or larger the particles are, the lower the volume fractions for which 2- and 4-way coupling effects are important.

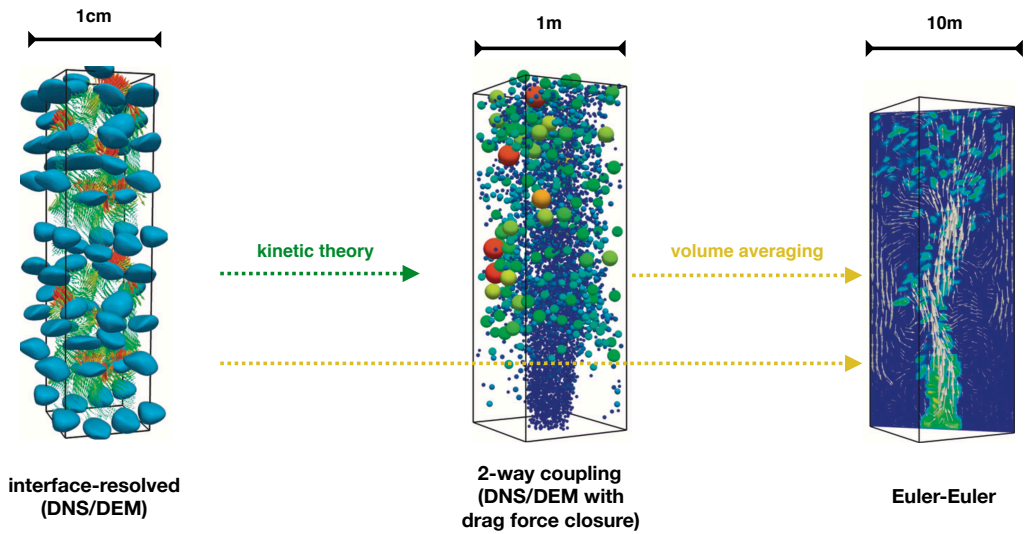


Figure 1.3: Schematic of a multi-scale modeling approach applied to a turbulent bubble column (figures adapted from [122]). Moving from left to right requires more modeling and less computing time (for fixed problem size). The finest level of detail is achieved through interface-resolved DNS approach (left). Treating the bubbles as spherical particles with closures for inter-phase momentum transfer can result in savings in computing time and allows for simulating bigger systems. Volume-averaging of the flow governing equations results in an even less expensive (two-fluid) Euler-Euler approach, which often can handle problems at the scale of industrial applications. With additional assumption on the Reynolds-averaged and volume-averaged flow, the two-fluid model can often be further simplified (e.g. from 3D to 1D).

phases (e.g. drag and particle stresses). This results in a so-called *Euler-Euler* description of the system, as both phases are treated as continua (see e.g. [42]). Insights on closure problems can be obtained from microscale simulations. This approach requires much less computational time, being important in many industrial applications that require prompt results for large systems.

An increasingly popular approach consists on *mesoscopic* (or kinetic) models, which can be seen as bridge between the micro and macroscopic approaches. Here, insights from microscale simulations are used to formulate kinetic equations for mesoscale variables, such as an equation for transport of particle number density; see e.g. [50, 101] for reviews. In this case, it is still possible to model distributions of the dispersed phase in a Lagrangian framework (see e.g. [22, 50]). A well-posed mesoscopic model should converge to the macroscopic model when a proper averaging procedure is applied to its equations.

Approaches at different scales can be used in a strategy for upscaling a given problem up to the engineering scale. Figure 1.3 presents an example of a multi-scale modeling strategy [63, 122], which can be used to scale problems to sizes of a realistic application. At each stage, some information is fed into the model to make the problem computationally less expensive and easier to upscale for a larger system. See the figure caption for a detailed explanation.

FULLY-RESOLVED SIMULATIONS – FROM POINT-PARTICLE TO INTERFACE-RESOLVED

The term *fully-resolved* always depends on the smallest relevant flow scale for the application at stake. In DNS of heavy particles much smaller than the relevant flow length scale, in a dilute regime, one can state that simulations with point-particle methods⁶ provide a similar level of detail when it comes to the turbulence modulation as an interface-resolved simulation, where the fluid-phase would be over-resolved. In the point-particle limit, the particle dynamics is governed by the well-known Maxey-Riley-Gatignol equation [51, 100] for a spherical particle with radius R :

$$\frac{d\mathbf{u}_p}{dt} = \underbrace{\frac{1}{\tau_p} \left(\mathbf{u} - \mathbf{u}_p + \frac{R^2}{6} \nabla^2 \mathbf{u} \right)}_{\alpha_d} + \underbrace{\frac{\rho_f}{\rho_p} \frac{D\mathbf{u}}{Dt}}_{\alpha_{pg}} + \underbrace{\frac{1}{2} \frac{\rho_f}{\rho_p} \left(\frac{D\mathbf{u}}{Dt} - \frac{D\mathbf{u}_p}{Dt} + \frac{R^2}{10} \nabla^2 \mathbf{u} \right)}_{\alpha_{am}} + \underbrace{\sqrt{\frac{9}{2\pi} \frac{\rho_f}{\rho_p} \frac{1}{\tau_p}} \int_{-\infty}^t \frac{1}{\sqrt{t-\tau}} \frac{d}{d\tau} \left(\mathbf{u} - \mathbf{u}_p + \frac{R^2}{6} \nabla^2 \mathbf{u} \right) d\tau}_{\alpha_h} \quad (1.1)$$

⁶ This nomenclature can be misleading, as in fact the size of the particle is considered in the governing equations of the particle motion. Point-particle approximation requires that the effect of particles in the flow is modeled by point forces.

with \mathbf{u}_p being the particle velocity and \mathbf{u} the velocity of the carrier fluid undisturbed by the presence of the particles, evaluated at the particle location; τ_p the particle response time in the Stokes limit: $(2/9)\rho_p R^2/\mu$. Term α_d on the right-hand-side corresponds to the Stokes drag, α_{pg} results from the local fluid acceleration, α_{am} to the *added mass* force required to displace carrier fluid as the particle moves, and α_h is the Basset history force term due to an unsteady diffusion of vorticity in the boundary layer around the particle [9]. Corrections for a non-uniform undisturbed flow field ($\propto \nabla^2 \mathbf{u}$) are known as Faxén corrections for finite size effects.

Several studies have been uncovering the dynamics of small particles in many canonical turbulent flows. Even so, eq. (1.1), also incorporating the Faxén corrections for finite size effects, still relies on a strict number of assumptions that loose the validity in 2- or 4-way coupling regimes, finite particle inertia, or particle size $D_p \gg \eta$, with η being the Kolmogorov microscale. First, the necessity of vanishing particle Reynolds number. Second, relying on a 1-way coupling framework where an undisturbed flow field modifies the particle dynamics but is not modified by it. Despite their limitations, 1-way coupling simulations have been providing insights on several canonical turbulent flows laden with solid particles, such as homogeneous isotropic turbulence e.g. [21, 124, 138]), wall-bounded flows [38, 125, 132], flows and jets [113].

The idea of the point-particle approximation for 2-way coupling is to model the effects of the dispersed particles in the flow through a localized source/sink of momentum in the discretized Navier-Stokes equations. Even without the need of accounting for 4-way coupling effects, this approach poses problems. When implemented in the most straightforward manner (particle-in-cell method [30]), it cannot reproduce consistently the simple benchmark of a particle settling in a quiescent fluid at low Reynolds number, while a 1-way coupling model – presumably incorporating fewer physics – can. In the case of a 2-way coupling simulation, the flow forcing acts such that the local drag force on the particle is reduced, thereby imposing an artificial acceleration on the particle, as illustrated in [57], who developed a more sophisticated 2-way coupling algorithm that overcomes these issues. Obviously, in a 4-way coupling regime one needs to resort to approaches that can account for short-range particle-particle interactions, which are very difficult to tackle without interface-resolved simulations.

MODELING 4-WAY COUPLING AND FINITE SIZE EFFECTS

Particles with a diameter D that is about the same or larger than the smallest flow relevant scale η (e.g. the Kolmogorov microscale, in turbulence) will be our definition of *finite size* particles. Finite-size effects are therefore responsible for deviations in the flow dynamics from the situation of particle size $D/\eta \ll 1$.

Limitations of the point-particle approximation justify the need for interface-resolved simulations. The exponential growth in computing power throughout the last decades⁷, in addition to the development of efficient numerical methods, allow for massively-parallel interface-resolved simulations of particle-laden flows. The current methods could be grouped in three categories, depending on the strategy for applying boundary conditions at the particle-fluid interface: body-fitted, fictitious domain, and meshless methods. We will briefly address the features of these methods (see also [99] for a recent review), restricting ourselves to approaches that couple a Navier-Stokes solver⁸ to a certain number of solid particles with finite size, through boundary conditions at the particle-fluid interface.

Body-fitted methods are those in which the computational grid conforms to the surfaces of all the particles (panel (a) of figure 1.4). They therefore employ an accurate description of the boundary conditions in the particle-fluid interfaces. Downsides of this approach are computational overhead associated with (1) solving the Navier-Stokes equations on the resulting complex geometry, and (2) re-gridding every time step. This approach has been applied in the first reported interface-resolved simulations coupling the motion of spherical particles to the Navier-Stokes equations [64, 72], in a finite-element framework. At present, the most used method is by Hu, Patankar, and Zhu [65], where the fluid flow is solved implicitly in a finite-element framework and the particle positions updated implicitly. Recent developments of efficient grid-overset methods [20] give exciting prospects for future interface-resolved body-fitted simulations, see [146]. These methods use two grids. Each particle is discretized in a body-fitted structured orthogonal grid, *overset* on a background grid, and on grids pertaining to other particles. Interpolation schemes are used to match numerical solutions of the two overlapping grids. From a computational point of view, the ideal problem for these methods are dilute systems, where the cost of re-gridding and slower Navier-Stokes solver is compensated by the flexibility in using an irregular mesh with a much smaller number of grid points, as recently demonstrated in [147].

Fictitious domain methods encompass most of the state-of-the-art methods that have been able to simulate mobile particle-laden flows with resolved particle-fluid interface. Several approaches have been developed and applied to particle-laden turbulent flows throughout the last two decades. These methods solve the equations governing the carrier fluid dynamics over the entire flow domain, including the one occupied by the dispersed particles. Then, special treatment on the grid cells near the particle surface allow for imposing boundary condition with satisfactory accuracy (see panel (b) of figure 1.4). This therefore allows for exploiting relatively efficient Navier-Stokes solvers, in structured Cartesian grids. The downside is a loss of accuracy in the imposition of boundary conditions at the particle surface, often with a non-sharp particle-fluid interface boundary

⁷ Following Moore's law [104].

⁸ At finite Reynolds number; therefore excluding several efficient methods based on the Stokes equations, such as boundary integral methods [117], or Stokesian dynamics (when one is solely interested in the particle dynamics) [14].

condition. In the following we highlight some popular methods and explain in words their concept.

- *Distributed Lagrangian Multiplier (DLM)* is an immersed-body method where the flow inside the particles is forced to comply to their rigid-body motion [52, 110]. This is achieved by introducing a distributed Lagrange multiplier; physically the additional force distribution required to impose these constraints.
- *Viscosity Penalization* methods (VPM) follow a conceptually simple approach: treating the flow inside the particles as a Newtonian fluid with viscosity $\nu_s \gg \nu$ [121, 144]. This poses some problems with respect to the Navier-Stokes solver that is being used. It should cope with large viscosity variations over few grid cells. If the solver cannot handle variations in viscosity, and the difference in viscosity must be decreased, then it can happen that the flow problem being solved becomes a different one than the one of the flow conforming rigid particles.
- *Direct Forcing Immersed-Boundary* method (IBM) is probably the most used approach at present⁹. The idea is relatively simple. A body force is added in the discretized momentum equations, computed such that no-slip and no-penetration boundary conditions are fulfilled, see e.g. [43, 102, 142]. This method will be discussed in detail in chapter 3. Contrarily to some previous methods, the flow field in the region inside the particles is not forced, and thus is not physically relevant for the application that is being studied. These methods are relatively simple to implement and allow for the use of very efficient Navier-Stokes solvers with direct solution for the pressure Poisson equation. Typically, this comes at the price of a small error in slip/penetration velocity when continuity is imposed following the fluid forcing, or an error in mass conservation, if non-divergent-free forcing is applied after imposing mass conservation.
- *Physalis* method [119, 134, 154] uses the fact that, very close to the particle surface, the fluid flow field relative to it satisfies the Stokes equations. Canonical solutions for the Stokes flow around a sphere are well-known in the literature (see e.g. [81]). These use a multipole (Lamb) series expansion and can accommodate any exterior flow condition. Typically, few low-order terms suffice for the relatively small particle Reynolds numbers (< 150). The Stokes solution is used as boundary conditions of a Navier-Stokes solver, and a few iterations between the Lamb solution and Navier-Stokes solver are performed. Advantages of this method are that it keeps the sharpness of the particle-fluid interface, and that the terms of the multipole expansion, needed for the calculation, have a clear physical meaning (e.g. drag, stresslet, rotlet); they do not need to be computed a posteriori for post-processing.

⁹ This claim is based on the number of citations of the pioneering papers on the methodology used for particle-laden flows in 2016, [142] for IBM, [52] for DLM, and others.

The main disadvantage comes from the computational effort required for matching the Stokes solution near the particle surface to the solution of the Navier-Stokes solver. Moreover, since pressure points inside the domain are forced, the pressure Poisson equation cannot be efficiently solved with direct methods. The most recent developments regarding this method can be seen in [128].

- *Lattice-Boltzmann* methods formulate the governing equations at a mesoscopic scale, in between the continuum (Navier-Stokes) and microscopic (molecular) descriptions [23]. It solves the evolution of a particle distribution function on a lattice, through a *streaming step* in between lattice points, and a *collision step* where the local distribution relaxes a certain time scale towards an equilibrium. It can be formally shown that this method solves the Navier-Stokes equations in a weakly-compressible form. Being a *particle-based* method, it performs well in several complex multi-physics problems, and allows for easy massively-parallel implementations: calculations are performed (almost) independently per particle, with little inter-process communication. For particle-laden flows, these methods are often implemented with a *bounce-back* boundary condition at the particle surface (typically inaccurate [23]), or combined with an Immersed-Boundary method [155].

Finally, a third modeling approach that is denoted Lagrangian or **meshless**. In this case both phases are described in a Lagrangian framework, as sketched in panel (c) of figure 1.4. This class of methods is advantageous when it comes to versatility: as it is meshless, difficult boundary conditions such as free surfaces, or immersed obstacles are straightforward to implement. Its major downside is its current inability of simulating canonical single-phase turbulent flows as accurately as Eulerian methods do. A popular method of this class is smoothed particle hydrodynamics [103]. In these methods, the computational domain is discretized in terms of Lagrangian particles, in which the governing equations and physical properties are obtained from a weighted average of surrounding particles with the aid of a smoothing kernel. The form of each weight-averaged terms is derived from the continuum equations for the fluid.

In the present work we adopted a fictitious domain method, suited for the type of problems that we will tackle: a large number of particles in relatively simple Eulerian domains and standard no-slip and no-penetration boundary conditions for inter-phase coupling. We will make use of the Immersed boundary method developed in [18]. Its suitability for the type of problems that we will address becomes clear during the description of our methodology in chapter 2.

1.2 OBJECTIVES AND STRATEGY

Ultimately, we apply a state-of-the-art algorithm to study particle-laden turbulent flows. Our objectives are therefore two-fold: (1) developing a numerical tool capable of simulat-

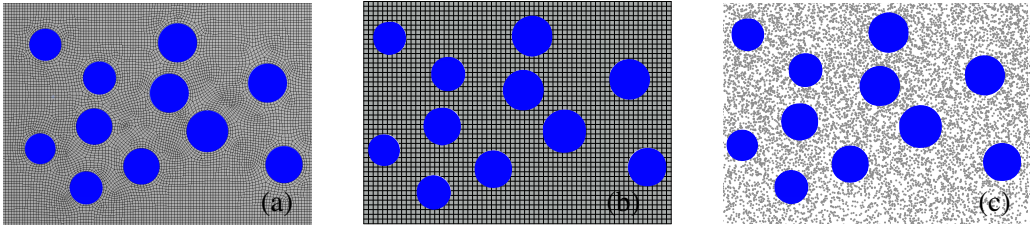


Figure 1.4: Illustration of the discretization strategy in a 2d domain for body-fitted (a), fictitious domain (b) and meshless (particle-based) (c) methods. Volumes/particles in gray discretize the carrier phase and large blue particles correspond to the dispersed phase.

ing relatively large systems with respect to the current state-of-the-art interface-resolved DNS; and (2) using it to study *turbulent transport of dense finite size particle suspensions*, one of a wide range of interesting problems that can be tackled with it, see e.g. [58].

For the first objective we need:

- an algorithm with both phases parallelized such that up to $O(10^6)$ finite size particles can be simulated, with efficient data-handling and post-processing (chapter 2);
- a physical model for short-range particle-particle/particle-wall interactions with little effect on the computational performance of the code (chapter 3).

For the second objective we aim in particular at:

- using simulations that allow for insights at the microscopic level to explain several macroscopic observables – *upscaling*;
- use this information to develop simple macroscopic descriptions of the mean turbulent suspension flow (chapter 4);
- and to understand in detail finite size effects: what causes differences in flow dynamics with respect to the case where the particles can be treated as point-particles (chapter 5).

As a starting point of this study, we used the code developed in [17, 18] for interface-resolved simulations of particle-laden flows, which was employed in e.g. [84, 85, 112, 114]. The inherent numerical algorithm uses an immersed-boundary method with second-order spatial accuracy, coupled to a standard second-order finite-volume numerical scheme to solve the Navier-Stokes equations. This scheme was coupled to a soft-sphere collision model used to model short-range particle-particle and particle-wall interactions, with analytical corrections for lubrication interactions in the Stokes regime. Despite the successes of the model, requirements of development in terms of the parallelization strategy and modeling of short-range particle-particle/-wall interactions have been detected and inspired chapters 2 and 3 of this thesis.

Subsequently we will apply the numerical algorithm to turbulent channel transport of neutrally-buoyant, finite size particle suspensions; a case that only recently started to be explored with accurate three-dimensional and time-resolved data. This inspired chapters 4 and 5, and is the core of the thesis.

1.3 OUTLINE

Following this introduction, in chapter 2 we introduce the governing equations and methodology used in the present study, followed by some benchmark assessments. Chapter 3 describes in detail the collision model developed in the framework of this thesis. Chapter 4 presents scaling laws for the mean flow obtained from interface-resolved simulations of turbulent suspension flows. Related to this, chapter 5 investigates finite size effects in turbulent suspension flows. Finally, in chapter 6 we present concluding remarks and future perspectives.

2

METHODS

Parts of this chapter will be included in J. Brändle de Motta et al. “Assessment of methods for fully resolved simulations of particle-laden turbulent flows.” In: *(in preparation)* (2017).

2.1 GOVERNING EQUATIONS

We aim at solving the Navier-Stokes equations for an incompressible, Newtonian fluid with density ρ and kinematic viscosity ν ,

$$\nabla \cdot \mathbf{u} = 0, \quad (2.1)$$

$$\frac{d\mathbf{u}}{dt} + \nabla \cdot (\mathbf{u}\mathbf{u}) = -\frac{1}{\rho} \nabla(p + p_e) + \nu \nabla^2 \mathbf{u}, \quad (2.2)$$

where \mathbf{u} is the fluid velocity vector, $p + p_e$ the fluid pressure with respect to an arbitrary constant reference value; ∇p_e corresponds to a constant pressure gradient that may serve as driving force for the flow. This set of equations is solved together with the Newton-Euler equations governing the motion of a rigid spherical particle with mass m_p and moment of inertia I_p ,

$$m_p \frac{d\mathbf{U}}{dt} = \oint_{\partial V} \boldsymbol{\sigma} \cdot \mathbf{n} dA + \mathbf{F}_c, \quad (2.3)$$

$$I_p \frac{d\boldsymbol{\Omega}}{dt} = \oint_{\partial V} \mathbf{r} \times (\boldsymbol{\sigma} \cdot \mathbf{n}) dA + \mathbf{T}_c, \quad (2.4)$$

where \mathbf{U} and $\boldsymbol{\Omega}$ denote respectively the particle linear and angular velocity vectors, $\boldsymbol{\sigma} \equiv -(p + p_e)\mathbf{I} + \mu(\nabla\mathbf{u} + \nabla\mathbf{u}^T)$ is the fluid stress tensor, \mathbf{r} a position vector with respect to the particle centroid, \mathbf{n} the outward-pointing unit vector normal to the particle surface, ∂V a parametrization of the surface area of the particle A , and \mathbf{F}_c and \mathbf{T}_c correspond to external forces and torques associated with short-range inter-particle or particle-wall interactions (such as solid-solid contact).

Eqs. (2.1) – (2.2) and (2.3) – (2.4) are coupled through no-slip and no-penetration boundary conditions at the particle surface:

$$\mathbf{U} + \boldsymbol{\Omega} \times \mathbf{r} = \mathbf{u} \quad \forall \mathbf{r} \in \partial V. \quad (2.5)$$

The challenge is to couple the two sets of equations in an efficient and yet reasonably accurate way, to allow for simulating relatively dense particle suspensions. In what follows we will present our methodology, starting with the treatment of the fluid phase.

2.2 NAVIER-STOKES SOLVER

The Navier-Stokes equations are solved with a pressure-correction method [1]. Considering for simplicity an explicit first-order time stepping with size Δt , it reads ($P \equiv p/\rho$)

$$\mathbf{u}^* = \mathbf{u}^n + \Delta t (\mathbf{A}^n + \mathbf{D}^n - \nabla P^n - \nabla P_e) \quad (2.6)$$

$$\nabla^2 \tilde{p} = \frac{1}{\Delta t} \nabla \cdot \mathbf{u}^* \quad (2.7)$$

$$\mathbf{u}^{n+1} = \mathbf{u}^* - \Delta t \nabla \tilde{p} \quad (2.8)$$

$$p^{n+1} = p^n + \tilde{p} \quad (2.9)$$

where the subscript n and $n + 1$ denote two subsequent time levels, and \mathbf{u}^* is the so-called prediction velocity. $\mathbf{A} = -\nabla \cdot (\mathbf{u}\mathbf{u})$ and $\mathbf{D} = \nu \nabla^2 \mathbf{u}$ denote respectively the advective and diffusive terms. The equations are discretized in space with a second-order finite-difference method (with advective term in divergence form), in a regular, staggered grid arrangement.

Typically the solution of the Poisson equation for the correction pressure \tilde{p} is most computation-intensive part of fluid-flow solvers. Since further on we will elaborate on the parallelization of this step of the numerical algorithm, we will briefly describe here the method for solving the Poisson equation. The discretized Laplace operator in this standard method, for grid cell (i, j, k) and uniform grid spacing $\Delta x/y/z$ reads (dropping the tilde from \tilde{p} for simplicity),

$$\begin{aligned} \nabla^2 P_{i,j,k} = & (P_{i-1,j,k} - 2P_{i,j,k} + P_{i+1,j,k})/\Delta x^2 + \\ & (P_{i,j-1,k} - 2P_{i,j,k} + P_{i,j+1,k})/\Delta y^2 + \\ & (P_{i,j,k-1} - 2P_{i,j,k} + P_{i,j,k+1})/\Delta z^2. \end{aligned} \quad (2.10)$$

This results in a system described by a matrix with 7 non-zero diagonals. We take advantage of the simplicity of our geometry and boundary conditions (e.g. periodic in at least two directions), and the fact that we use at least in two directions a regular, Cartesian grid. This allow us to solve the Poisson equation with a fast (FFT-based) direct method (see e.g. [126]). The underlying idea is to reduce the number of diagonals of the resulting system of equations by applying eigenfunction expansions to the regular domain directions, thereby reducing the system of equations into a tri-diagonal system, easily solvable with Gauss elimination¹. For periodic boundary conditions, two consecutive discrete Fourier transforms can be applied in the periodic directions of the domain. Using the shift theorem, it

¹ The system could also be solved by applying eigenfunction expansions in the other domain direction. However, this is more expensive than solving a tri-diagonal system with Gauss elimination

can be shown that the finite-difference equation with directions i and j in Fourier space reduces to

$$\nabla^2 \hat{P}_{\hat{i},\hat{j},k} = (\lambda_{\hat{i}}/\Delta x^2 + \lambda_{\hat{j}}/\Delta y^2) \hat{P}_{\hat{i},\hat{j},k} + (\hat{P}_{\hat{i},\hat{j},k-1} - 2\hat{P}_{\hat{i},\hat{j},k} + \hat{P}_{\hat{i},\hat{j},k+1})/\Delta z^2 \quad (2.11)$$

with $\hat{i}/\hat{j} = 0, 1, \dots, N_{i/j}/2$ for $N_{i/j}$ even; $N_{i/j}$ correspond to the number of grid points in the i/j direction. The eigenvalues are given by $\lambda_{\hat{i}} = -2(1 - \cos(2\hat{i}\pi/N_i))$ (ditto for \hat{j}). The solution procedure involves therefore 3 steps. First, applying a 2D Fourier transform operator to the right-hand-side of the Poisson equation. Second, solving the resulting tri-diagonal system with Gauss elimination, and a solution for \hat{P} is obtained. Third, applying the respective inverse Fourier transform to \hat{P} , yielding the final solution of eq. (2.7). This procedure can also be applied to solve efficiently other combinations of homogeneous boundary conditions, namely Neumann-Neumann, Dirichlet-Dirichlet or Neumann-Dirichlet. We refer to [126] for the eigenfunction expansions pertaining to other boundary conditions. We should note that this approach cannot be used for non-uniform grid spacing or more complex boundary conditions (e.g. Robin). When that is the case, iterative solvers (such as preconditioned conjugate gradient methods [53]) are typically the most efficient choice.

2.3 IMMERSSED-BOUNDARY METHOD

We use the direct forcing IBM developed in [18], briefly explained below. The IBM uses a quasi-2D Lagrangian grid to discretize the particle surface (see figure 2.1), while the fluid is discretized on a regular² Eulerian mesh. The fluid prediction velocity is *interpolated* from the Eulerian to a Lagrangian grid. There the force required for satisfying no-slip and no-penetration is computed. Subsequently, the force is *spread* back to the Eulerian grid. A regularized Dirac delta function δ_d with support of 3 grid cells is used to perform interpolation and spreading operations [123, 142]. The regularization of the particle-fluid interface can result in a loss of spatial accuracy to first-order. Breugem [18] showed that a slight inward retraction of the Lagrangian grid by a factor $\approx \Delta x/3$ (while the particle governing equations are still solved considering its actual radius R) circumvents this issue and allows for second-order spatial accuracy (figure 2.1(b)). The support of the interpolation kernel is such that the same Eulerian grid point can be forced due to neighboring Lagrangian grid points – reducing the accuracy of the imposition of BC. Errors in penetration velocity arising from this are mitigated via a multi-direct forcing scheme [95] (figure 2.1 (c)), which improves the calculation of the force distribution by iterating the

² As implemented, the conservation of total force/torque of the interpolation kernel holds for a regular grid, our direct fluid solver could accommodate one irregular direction and, at the cost of a more expensive calculation, use the methodology in [115] or [70] for interpolation/spreading operations that conserve total force/torque on irregular meshes.

forcing scheme. We refer to [18] for more details on this IBM and Navier-Stokes solver. To facilitate readability, we write below the numerical algorithm described therein. The solution advances from time step n to $n + 1$ with the following pressure-correction scheme and a third-order Runge-Kutta (RK3) temporal integration:

for q in $1, 2, 3$ **do**

$$\mathbf{u}^* = \mathbf{u}^{q-1} + \frac{\Delta t}{\rho} \left(-(\alpha_q + \beta_q) \nabla P^{q-3/2} + \alpha_q \mathbf{AD}^{q-1} + \beta_q \mathbf{AD}^{q-2} \right)$$

$$\mathbf{u}_{ijk}^{**,s-1} = \mathbf{u}^*$$

for s in $0, 1, \dots, N_s$ **do**

$$\mathbf{U}_l^{**,s-1} = \sum_{ijk} \mathbf{u}_{ijk}^{**,s-1} \delta_d \left(\mathbf{x}_{ijk} - \mathbf{X}_l^{q-1} \right) \Delta x \Delta y \Delta z$$

$$\mathbf{F}_l^{q-1/2,s} = \mathbf{F}_l^{q-1/2,s-1} + \left(\mathbf{U}_p \left(\mathbf{X}_l^{q-1} \right) - \mathbf{U}_l^{**,s-1} \right) / \Delta t$$

$$\mathbf{f}_{ijk}^{q-1/2,s} = \sum_l \mathbf{F}_l^{q-1/2,s} \delta_d \left(\mathbf{x}_{ijk} - \mathbf{X}_l^{q-1} \right) \Delta V_l$$

$$\mathbf{u}^{**,s} = \mathbf{u}^* + \Delta t \mathbf{f}^{q-1/2,s}$$

end for

$$\nabla^2 \tilde{p} = \frac{\rho}{(\alpha_q + \beta_q) \Delta t} \nabla \cdot \mathbf{u}^{**,N_s}$$

$$\mathbf{u}^q = \mathbf{u}^{**,N_s} - \frac{(\alpha_q + \beta_q) \Delta t}{\rho} \nabla \tilde{p}$$

$$p^{q-1/2} = p^{q-3/2} + \tilde{p}$$

integrate Newton-Euler equations

end for

where the Runge-Kutta step q corresponds to time step n for $q = 0$ and $n + 1$ for $q = 3$. \mathbf{AD} denote the advective and diffusive terms. Variables with capital case \mathbf{U} and \mathbf{F} correspond respectively to velocities and forces in a Lagrangian grid point l , while the respective lower case letters pertain to the same quantities in the Eulerian grid. ΔV_l corresponds to the volume of the Lagrangian grid cell, set to be as close as possible to the volume of an Eulerian grid cell $\Delta x \Delta y \Delta z$. $\mathbf{u}^{**,s}$ is the second prediction velocity at iteration step s of the multi-direct forcing scheme, with N_s steps. The Runge-Kutta coefficients can be found in e.g. Wesseling [150]: $\alpha_1 = 32/60$, $\beta_1 = 0$, $\alpha_2 = 25/60$, $\beta_2 = -17/60$, $\alpha_3 = 45/60$, $\beta_3 = -25/60$. Sufficient condition for a stable temporal integration is given by the following criterion:

$$\Delta t \leq \min \left(\frac{1.65}{12} \frac{\Delta x^2}{\nu}, \frac{\sqrt{3} \Delta x}{\max_{ijk} (|u| + |v| + |w|)} \right) \quad (2.12)$$

where the restriction due a viscous CFL-like criterion could be removed with an implicit (e.g. Crank-Nicolson) discretization of the diffusion term, which in practice involves the solution of a 3D Helmholtz equation for each domain direction [150]. We did not use such approach, as this restriction was typically not the bottleneck for the cases simulated in this work.

A straightforward integration of the Newton-Euler equation can become unstable for low density ratios. First, due to a singularity in their integration when rigid-body motion

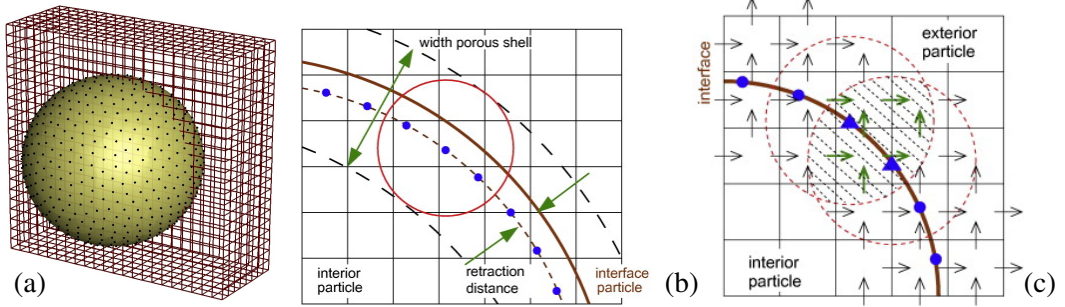


Figure 2.1: Sketch of the quasi-2D Lagrangian and 3D Eulerian grids, discretizing respectively the carrier phase and the particle surface (a). Inward-retraction of the Lagrangian grid (b) and illustration of a source of error in the imposition of boundary conditions due to spreading operations to the Eulerian grid from different Lagrangian grid points (c); figures from [18].

of the fluid inside the particle is indirectly taken into account, for $\rho_p = \rho_f$ (index p and f correspond respectively to particle and fluid). When no special treatment for this singularity is made, the solution becomes unstable at density ratios $\rho_p/\rho_f \approx 1.2$. This restriction has been circumvented by directly accounting for the fluid inertia inside the particle [18, 77], integrating it through the Eulerian grid points inside the sphere with a second-order level-set approach. Still, the temporal integration of the particle motion becomes unstable for $\rho_p/\rho_f \approx 0.3$, which and has been attributed to an increasing importance of added mass effects. Tschisgale, Kempe, and Fröhlich [139] proposed a scheme that introduces an added-mass-like term that allows for stable integration of the Newton-Euler equation for relatively small particle densities. Circumventing this instability was not required for the set of parameters that has been addressed in this work.

The temporal integration of the Newton-Euler equations mentioned in the RK3 loop presented above yields,

$$\begin{aligned} \mathbf{u}_c^q &= \mathbf{u}_c^{q-1} - \frac{\Delta t}{V_p} \frac{\rho_f}{\rho_p} \sum_l \mathbf{F}_l^{q-1/2, N_s} \Delta V_l \\ &+ \frac{1}{V_p} \frac{\rho_f}{\rho_p} \left(\left\{ \int_{V_p} \mathbf{u} dV \right\}^q - \left\{ \int_{V_p} \mathbf{u} dV \right\}^{q-1} \right) \\ &+ (\alpha_q + \beta_q) \Delta t \left(1 - \frac{\rho_f}{\rho_p} \right) \mathbf{g} + \left(\frac{\alpha_q + \beta_q}{2} \right) \Delta t \frac{(\mathbf{F}_c^q + \mathbf{F}_c^{q-1})}{(\rho_p V_p)}, \end{aligned} \quad (2.13)$$

$$\begin{aligned} \boldsymbol{\omega}_c^q &= \boldsymbol{\omega}_c^{q-1} - \Delta t \frac{\rho_f}{I_p} \sum_l \mathbf{r}_l^{q-1} \times \mathbf{F}_l^{q-1/2, N_s} \Delta V_l \\ &+ \frac{\rho_f}{I_p} \left(\left\{ \int_{V_p} \mathbf{r} \times \mathbf{u} dV \right\}^q - \left\{ \int_{V_p} \mathbf{r} \times \mathbf{u} dV \right\}^{q-1} \right) \\ &+ \left(\frac{\alpha_q + \beta_q}{2} \right) \Delta t \frac{(\mathbf{T}_c^q + \mathbf{T}_c^{q-1})}{I_p}, \end{aligned} \quad (2.14)$$

where the last 4 terms in eq. (2.13) are obtained from Newton's law at the discrete level (and ditto in eq. (2.14) for conservation of angular momentum) and correspond respectively to (1) the sum of the IBM force contribution (of the fluid on the particle) at the particle surface, (2) the inertia of the fluid inside the particle, computed directly [77] and not analytically from a requirement of rigid body motion [142], (3) buoyancy and (4) short-range particle-particle/-wall interactions such as solid-solid contact or lubrication.

2.4 SHORT-RANGE PARTICLE-PARTICLE AND PARTICLE-WALL INTERACTIONS

Short-range hydrodynamic particle-particle and particle-wall interactions are also partly reproduced by the IBM. However, since the method uses a fixed grid, a lubrication model is needed for an inter-particle gap width smaller than the grid spacing. Our lubrication model is based on asymptotic expansions of analytical solutions for canonical lubrication interactions between spheres in the Stokes regime. Roughness effects are incorporated by making the lubrication correction independent of the gap width for gap widths smaller than $\sim 1\%$ of the particle radius. This correction is applied until the particles reach solid-solid contact. Then, the corresponding contact force is modeled by a soft-sphere collision model. This approach for short-range particle-particle and particle-wall interactions, developed in the present study, is described in chapter 3.

2.5 COMPUTATIONAL IMPLEMENTATION AND PARALLELIZATION

Achieving massively parallel simulations of relatively large systems, larger than e.g. the 10^4 interface-resolved turbulent suspension in [112] required significant changes in the original algorithm of Breugem [18].

The numerical algorithm has been implemented in a FORTRAN90 code using a Message-Passing Interface (MPI) standard for distributed memory parallelization, together with a shared memory (OpenMP) parallelization. Next we will explain some general, less obvious features of the implementation of the resulting code, named *InterPartS*³.

2.5.1 FLUID FLOW SOLVER

The three-dimensional regular Eulerian grid is divided into several computational subdomains. In most steps of the numerical algorithm, these share the total length of the domain in one direction (the wall-normal, z), being of equal or smaller size than the domain length in the other directions. This configuration is commonly denoted as two-dimensional *pencil*-like decomposition. The finite-difference algorithm requires communication due to the 2-cell width of the computational stencil. We use halo cells that store a copy of data pertaining to the boundary of an adjacent subdomain, common practice in this kind of numerical codes. This requires a simple pair-wise exchange of data (e.g. `SEND_RECV`) of a *derived type* (`VECTOR`) describing data layout of the halo region, see figure 2.2. We refer the reader unfamiliar with the nomenclature of the MPI standard to [49].

Poisson solver

The numerical algorithm takes advantage of a direct, FFT-based solver for the pressure Poisson equation (eq. (2.7)), as described before. Its implementation steps are summarized below.

³ Short for *INTER*face-Resolved *PART*icle Simulations.

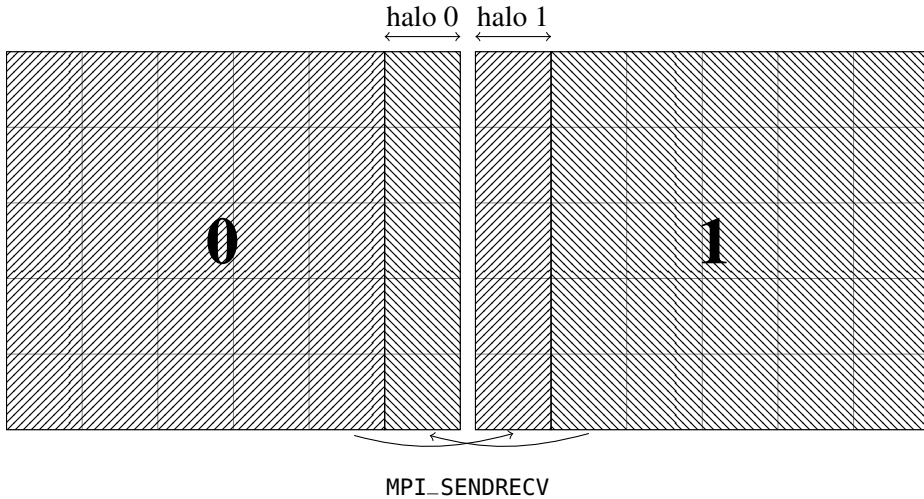


Figure 2.2: Schematic of the exchange of information in the vertical direction (the same operation is performed in the horizontal direction) for a 2D distributed memory parallelization. Information pertaining to the boundary of task 0 is sent to the y -halo of task 1 and vice-versa. Exchange of information can be achieved through a `SEND_RECV` call.

Algorithm 1 Steps taken to solve the Poisson eq. (2.7), together with the number of operations. Total number of operations $\mathcal{O}(N_x N_y N_z (\log N_x N_y))$. For more details see e.g. [126].

- 1: compute the right-hand-side (RHS) of the pressure Poisson equation ($\mathcal{O}(N_x N_y N_z)$ operations);
 - 2: compute N_z 2D discrete Fourier transform (DFT) of the RHS over two periodic directions ($\mathcal{O}(N_z (N_y N_x \log N_x + N_x N_y \log N_y))$ operations);
 - 3: solve the resulting $N_x N_y$ tri-diagonal systems for the pressure with Gauss elimination ($\mathcal{O}(N_x N_y N_z)$ operations);
 - 4: compute N_z 2D inverse DFT of the resulting pressure field ($\mathcal{O}(N_z (N_y N_x \log N_x + N_x N_y \log N_y))$ operations).
-

These computation steps must be implemented in a parallel framework. The RHS of the Poisson equation is computed in the 2D pencil configuration. Subsequent communication steps for computing the Fourier transforms are required. The 2D DFT are computed through two successive 1D DFT in each of the directions. Each DFT requires all the grid cells for the direction at stake, making further communication operations unavoidable.

Two approaches were considered. The first one takes the following steps: (i) change the data distribution from a 2D to a 1D *slab-like* configuration (see panel (a) of figure 2.3), (ii) perform the 1D DFTs in both directions, (iii) change the distribution back to 2D to (iv) solve the resulting tri-diagonal system with Gauss elimination and (v) perform the

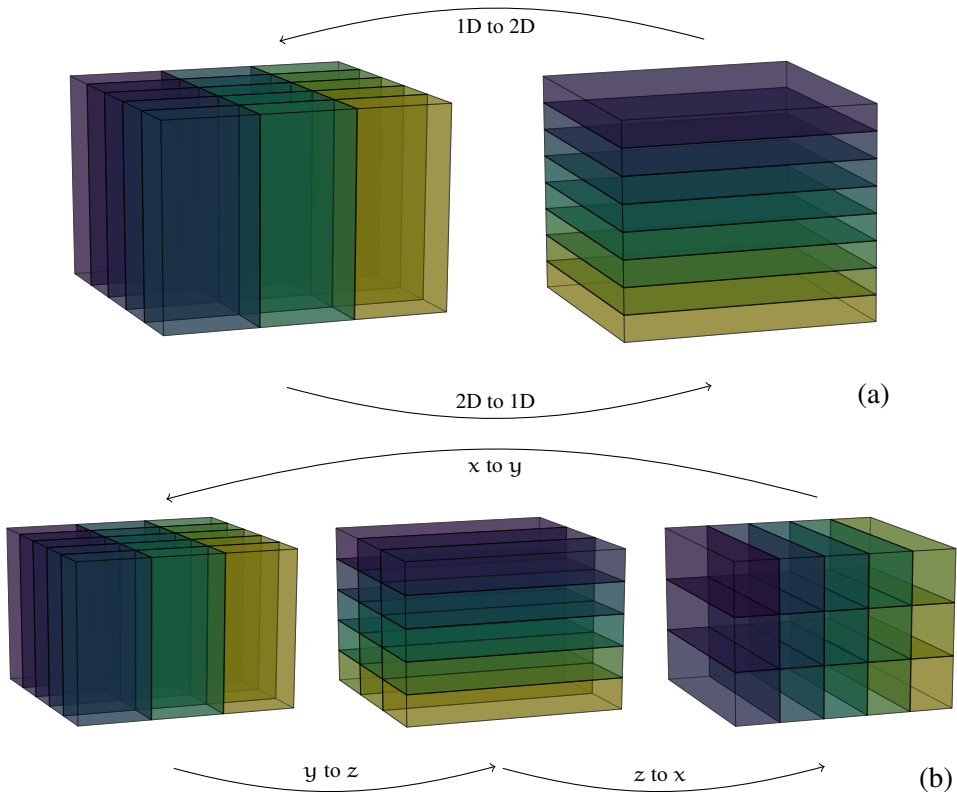


Figure 2.3: Illustration of data transposes in a 1D *slab-like* decomposition (a) and of a 2D *pencil-like* decomposition (b). Each arrow involves in an *all-to-all* operation. Colors illustrate different process IDs.

reciprocal operations on the obtained solution (now using inverse DFT) in order to obtain the pressure field in physical space. The required communication for changing the distribution from 1D/2D to 2D/1D can be achieved through a single (MPI) *all-to-all* operation⁴. The disadvantage of this approach is that it is restrictive in terms of the number of points in the direction perpendicular to the slabs: $N_z \leq N_1 N_2$, with $N_{1/2}$ the number of computational subdomains in direction 1/2.

Two workarounds for this restriction are as follows. First, one can combine the distributed memory with a shared memory parallelization (e.g. a hybrid MPI-OpenMP implementation). This way, the domain can be distributed in MPI tasks such that maximum number of tasks is satisfied, and distribute the load further via shared-memory parallelization⁵. This option can still be restrictive for relatively large systems, when more than $O(10^4)$ tasks are required. The second approach keeps the 2D parallelization, and transposes the

⁴ Meaning communication *from all, to all* tasks.

⁵ Typically in large-scale supercomputing facilities the number of cores sharing memory ranges from 16-32, see e.g. the top500.org list.

data distribution, such that it is shared in the direction of interest, see panel (b) of figure 2.3. This requires more communication, as each transpose performs an *all-to-all* operation. However, the number of MPI tasks can now be larger than N_z . There is a still restriction on the size of the computational subdomains, which should at most fit the computational grid (i.e. $N_x N_y \leq N_1 N_2$). Nevertheless, for the typical domain sizes and number of tasks considered in our simulations, this does not pose problems. We use the data transpose routines from the 2DECOMP&FFT libraries [90]. The algorithm for solving the Poisson equation is summarized below:

Algorithm 2 Implementation of the Poisson solver in a distributed memory parallelization (see also figure 2.3 (b)).

- 1: compute the RHS of the Poisson equation in the z -aligned pencil decomposition, and transpose result to y -aligned pencil decomposition;
 - 2: compute $N_x N_z$ 1D DFT in y , and transpose result to x -aligned pencil decomposition;
 - 3: compute $N_y N_z$ 1D DFT in x , and transpose result to z -aligned pencil decomposition;
 - 4: solve $N_x N_y$ linear tridiagonal systems with Gauss elimination; transpose result to x -aligned pencil decomposition;
 - 5: compute $N_y N_z$ inverse 1D DFT in x , and transpose result to y -aligned pencil decomposition;
 - 6: compute $N_x N_z$ inverse 1D DFT in y , and transpose result to z -aligned pencil decomposition.
-

Algorithm 2 involves 6 *all-to-all* operations due to the transposing routines, in contrast with the 1D slab decomposition, which involves 4. One should therefore resort to the 1D alternative whenever $N_z \bmod N_1 N_2 = 0$.

2.5.2 PARTICLE TREATMENT

The dispersed phase decomposition uses a master-slave technique, conceptually similar to the one in [141]. The load due to particle-related computations is spread to the computational subdomains containing the Eulerian data required for interpolation/spreading operations, which is – like the fluid velocity data – distributed in a 2D pencil configuration. The *master* process of a certain particle corresponds to the computational subdomain containing its centroid, and *slaves* to other subdomains crossing the particle-fluid interface (also accounting for the support of the IBM interpolation kernel). For ease of implementation, we require that no more than 4 different processes can handle the same particle, see figure 2.4. Consequently, each particle contains one master process, and at most three slave processes. This results in the following restriction to the number of subdomains in direction i :

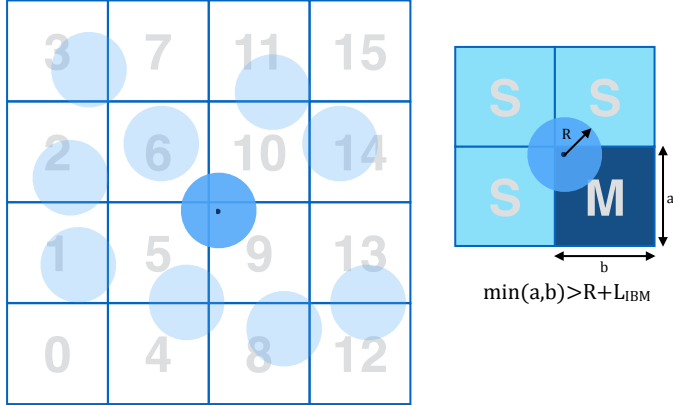


Figure 2.4: Schematic of master-slave parallelization for the dispersed phase in a 2D decomposition. The numbers denote the task IDs, M – master and S – slave. The size of the computational subdomains must be larger than the particle size. When further load distribution is required, a hybrid MPI-OpenMP parallelization is adopted. $L_{IBM} = \sqrt{3}\Delta x - d_{IBM}$, see eq. (2.15).

$$\left(\frac{L_i}{N_i}\right) > D_p - d_{IBM} + \sqrt{3}\Delta x, \quad i = 1, 2; \tag{2.15}$$

where $\sqrt{3}\Delta x$ accounts for the support of the regularized delta function used in the IBM, and d_{IBM} for the possibility of slight inward retraction of the Lagrangian grid [18]. To overcome this restriction without complicating the distributed-memory parallelization, we combine this master-slave technique with a shared-memory parallelization. Note that this restriction is relaxed when shifting to a 3D domain decomposition, as the subdomains can be bigger for the same number of tasks. The advantage of using 2D over 3D decomposition is the wider range of applications for which load balancing is not compromised: 2D allows for a direction with inhomogeneous particle distribution.

IBM forcing

Of all the operations required when including particles in the computation, the IBM forcing scheme is the most intensive. Implementing it in a distributed-memory parallelization requires some communication, as data required to perform interpolation/spreading operations can be distributed over different computational subdomains. We recall that the

following mathematical operations are to be performed, per Lagrangian grid point, per particle:

$$\mathbf{U}_l = \sum_{ijk} \mathbf{u}_{i,j,k} \delta_d(\mathbf{x}_{i,j,k} - \mathbf{X}_l) \Delta V_e, \quad (2.16)$$

$$\mathbf{F}_l = \frac{\mathbf{U}_l - \mathbf{U}_{p,l}}{\Delta t}, \quad (2.17)$$

$$\mathbf{f}_{i,j,k} = \sum_l \mathbf{F}_l \delta_d(\mathbf{x}_{i,j,k} - \mathbf{X}_l) \Delta V_l; \quad (2.18)$$

the notation used above has been introduced in section 5.2. Two approaches were considered.

The first one consists of communicating the data in a *Lagrangian* framework, i.e. the information pertaining to a certain particle is gathered and processed by the master process, which broadcasts the results to the slave processes, as explained below in algorithm 3:

Algorithm 3 Distributed memory implementation of IBM forcing with communications in a Lagrangian framework.

```

1: for p in 1 .. pmax do                                     ▷ loop through particles
2:   for l in 1 .. nl do                                       ▷ loop through Lagrangian grid points
3:     if grid point inside computational subdomain then
4:       compute partial sum of eq. (2.16) pertaining to this task for grid point l
5:     end if
6:   end for
7: end for
8: for p in 1 .. pmax do
9:   slaves communicate partial sums to masters (size of the communication package
   ∝ Nl)
10:  master collects partial sums from slaves and adds them, thereby computing  $\mathbf{U}_l$  in
   eq. (2.16)
11: end for
12: for p in 1 .. pmax do
13:  master broadcasts total force/torque sums per Lagrangian grid point to slaves
14: end for
15: for p in 1 .. pmax do
16:   for l in 1 .. nl do
17:     compute eq. (2.17) and spread IBM force (eq. (2.18)) to the Eulerian grid
18:   end for
19: end for

```

with pmax being the amount of particles for which task me is master/slave ($\leq N_p$). The advantage of this approach is that the associated load scales with the number of particles;

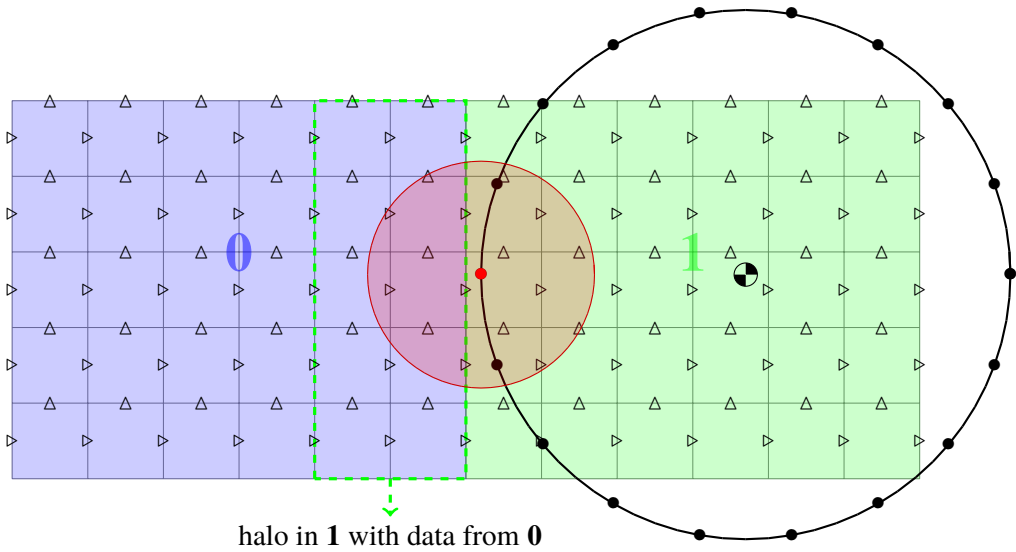


Figure 2.5: Schematic of the Eulerian-based communication strategy that substitutes master-slave communication during the IBM forcing scheme. In this 2D description, the large circle denotes a particle, discretized by the black bullets throughout its boundary. Triangles denote the velocity components in a regular mesh with staggered arrangement, and the translucent red circle shows the support of the IBM interpolation kernel for a certain Lagrangian grid point. The kernel support is covered through 2-cell-spanned halo regions containing a copy of the data from neighboring tasks.

if there are no particles, no data is communicated. The flip side is that it requires, at least in the most straightforward implementation, communication of $O(n\iota)$ reals ($n\iota$ being the total number of Lagrangian grid points), even though only a small fraction of the partial sums are performed by more than one task. The amount of communicated data only scales down with increasing number of subdomains when a task is no longer master/slave of a certain particle.

The second scenario is communicating the data in an *Eulerian* framework, through halo regions that cover the support of the IBM kernel, see figure 2.5. The disadvantage of this approach is evident: the amount of reals being communicated does not scale down with decreasing number of particles. The advantage, other than its simplicity, is that the amount of communicated data decreases with increasing number of tasks. Moreover, the associated communication load is known a priori, and evenly distributed throughout all the tasks. In this approach the task associated with the subdomain that contains a certain Lagrangian grid point ι will compute the total sum over the required Eulerian grid points, meaning that now both masters and slaves process partial sums of data that was originally distributed in different tasks. This allows for restricting the size of the loops through Lagrangian grid points to those that are actually contained in the subdomain. The algorithm reads,

Algorithm 4 Distributed memory implementation of IBM forcing with communications in an Eulerian framework.

```

1: copy data to IBM halos
2: for  $p$  in  $1 \dots p_{\max}$  do                                ▷ loop through particles
3:   for  $\iota$  in  $1 \dots n\iota(p)$  do  ▷ loop through Lagrangian grid points handled by that
   subdomain ( $n\iota(p) \leq n\iota$ )
4:     compute eq. (2.16) for grid point  $\iota$ 
5:     compute IBM force (eq. (2.17)) for grid point  $\iota$ 
6:     spread IBM force (eq. (2.18)) to the Eulerian grid, including the IBM halos
7:   end for
8: end for
9: communicate partial force/torque sums in IBM halos to the corresponding compu-
   tational subdomain where they belong, and compute the total sum in each Eulerian
   cell

```

We compared both Lagrangian and Eulerian approaches for communicating particle-related data. The latter approach proved to perform much better, specially for dense cases. As an example, for the turbulent suspension at 20% volume fraction presented in [112]⁶, a speedup in particle treatment of 60%, yielding an overall speedup of 40%.

⁶ A turbulent channel flow with neutrally-buoyant spherical particles, with the fluid phase discretized with ~ 0.1 billion grid points, and ~ 7.5 million Lagrangian grid points discretizing the dispersed phase.

Master/slave communication is still needed for computing sums over the entire Lagrangian grid, required for integrating the equations of motion of the particle (see eqs (2.3) – (2.4)). This is achieved using the following non-blocking communication steps (m_e denotes the ID of the task):

Algorithm 5 Distributed memory implementation of a sum over the entire Lagrangian grid. $neighbor$ is an array listing the IDs of the 8 neighboring tasks.

```

1: for  $p$  in 1 ..  $p_{max}$  do
2:   for  $nb$  in 1 .. 8 do                                ▷ loop through the neighboring tasks
3:     if  $m_e$  is master and  $neighbor(nb, p)$  is slave then
4:       non-blocking receive call
5:     end if
6:     if  $m_e$  is slave and  $neighbor(nb, p)$  is master then
7:       non-blocking send call
8:     end if
9:   end for
10:  synchronize                                          ▷ wait until messages have been received
11: end for

```

Only 6 scalars, namely the partial sums of force and torque acting on the Lagrangian grid points, are communicated. Since particle-related data is distributed (i.e. not global), the algorithm above requires that particle-related arrays are ordered by ID. Otherwise, deadlocks can occur at the *synchronize* statement.

Data handling

Like the fluid data, particle-related data are distributed over the computational subdomains. Each task m_e stores an array of a derived type *particle*. This choice is natural, as master/slave communication is typically performed in terms of properties of a single particle, and not a single property for many particles. Each element of this array contains the following information (circle bullets (●) represent data that is communicated between tasks, and square bullets (■) data that is not):

- \mathbf{x} , θ , \mathbf{u} , $\boldsymbol{\omega}$, $\int \mathbf{u} dV_e$, \mathbf{F}_c , \mathbf{T}_c , etc.

This results in $24 + 10N_q$ real numbers, stored contiguously in memory to facilitate master-slave communication, N_q is the maximum number of particles colliding with a single particle⁷;

- ID – an integer which absolute value $abs(ID)$ is the global ID of the particle. It is positive in case m_e is master of $abs(ID)$ and negative in case task is a slave;

⁷ The model for the tangential collision force has memory, requiring storage of tangential inter-particle displacements.

- data pertaining to Lagrangian grid points, and integrals over the grid ($12N_L + 6$ reals);
- other relevant parameters pertaining to the particles' physical/geometrical properties.

The order of the particle-arrays presented above is not arbitrary. It is such that data that must be communicated over different tasks is contiguously stored in memory, and therefore one only needs to specify the address of the first element and the number of elements to be communicated in order to have it communicated across tasks. For a memory-efficient implementation, the size of an array of derived type *particle* solely contains information of particles belonging to task *me*, having a size $np_{\max} \leq np$. These arrays are static and therefore np_{\max} is an educated guess of the maximum number of particles that will be contained on that computational subdomain.

Initialization of particle-related data

Following the temporal integration of the Newton-Euler equations (eq. (2.3) – (2.4)), several steps should be taken before proceeding with the numerical algorithm, starting by determining the new master/slave processes of each particle. The procedure can be summarized in the following steps:

1. Determine if particle has a new master.
If so, a neighboring process was its master in the previous time step⁸. These two processes exchange information.
2. To perform communications such as the ones in algorithm 5, the array of derived type *particle* is ordered by increasing value of ID. Particles for which a task just became slave at the current time level, and for which a task was already master/slave, must be ordered. A binary search algorithm is used to find the position p ($< p_{\max}$) in the array corresponding to particle $\text{abs}(ID)$ in the previous time level.
3. Initialize fields of the derived types for the masters and slaves. Some of these (e.g. centroid position and velocity) are conveniently stored in both master and slave processes.
4. Determine which Lagrangian grid points are within which process, and store their ID in an array $nla(1:nl(p))$, where $nl(p)$ denotes the number of Lagrangian grid points for particle p that task *me* is in charge of.

⁸ We assume the temporal resolution to be such that a particle cannot travel through more than 1 computational subdomain in 1 timestep.

Short-range particle-particle interactions

Each particle p mastered by task m_e requires a search for short-range particle-particle interactions⁹. This search is only performed – first of all – only in particles contained in m_e and the 8 neighboring tasks. There is still significant room for improvement at this point: as we consider particles distributed over 2D pencils, there may be several inquiries for collision that can be disregarded a priori for particles very far apart along the length of the pencils. To narrow the search we define for each particle a list of neighboring particles, that are inside a $2D_p$ square box centered at the particle centroid. This list is recurrently updated.

2.5.3 APPLICABILITY OF OUR METHOD

At this point we have all the information needed to comment on our method's applicability and preferred type of problems: dense, inertia-dominated¹⁰ flows laden with finite-size, rigid, spherical particles. In particular,

- large particles, otherwise it is computationally difficult to use $O(10)$ Eulerian grid points conform to the particle diameter;
- inertia-dominated due to the explicit temporal integration of the diffusion term, and the weak coupling between the equations of fluid and particle phases (i.e. there is no iteration through fluid and particle solutions within one time step);
- mono-disperse, spherical particles (although the extension to poly-disperse and non-spherical cases is straightforward and has been achieved in [3] and [86]);
- when moderately dense, there should be no more than 1 statistically inhomogeneous direction, due to the 2D domain decomposition of the numerical algorithm.

2.5.4 VALIDATIONS AND SCALING PERFORMANCE

Our numerical algorithm has been extensively validated against several configurations, including:

- Flow through a regular array of spheres at solid volume fraction of 6.5% for which 2nd order accuracy has been shown [18].
- Lubrication force between 2 spheres, and a sphere and a wall: accurate predictions up to a gap width of 2.5% of the sphere radius at resolution $D/dx = 32$ [17, 18].

⁹ With regard to short-range solid-solid interactions, a wall is treated in the code as a particle with different geometrical properties.

¹⁰ The particle Reynolds number should still be sufficiently small ($\lesssim 100$), as we cannot otherwise resolve the thin boundary layer along the particle surface.

- Head-on/oblique particle-wall collisions in a viscous fluid (coefficients of restitution/bouncing motion, etc) [27] (*in chapter 3 of this thesis*).
- Effective viscosity of a suspension of non-Brownian spheres [112, 114].
- Particle settling velocity versus time [135] in [85].
- Trajectory of a particle pair released in a simple shear flow, against data from other numerical implementations, in [85].
- Jeffrey's orbits and settling of non-spherical particles in quiescent environments [3].

Scaling performance for particle-laden turbulent channel flow

We investigated the performance of our numerical algorithm in a case where the fluid and particle-related load are of the same order of magnitude, and where the fluid-related load is such that *all-to-all* communications can compromise scaling. Table 2.1 summarizes the most demanding communication steps in the numerical algorithm.

Table 2.1: Summary of the most demanding communication steps taken in the numerical algorithm. Note that the IBM forcing scheme requires updates in the halo cells for each velocity component, for interpolation and spreading operations, times the number of iterations of the IBM forcing scheme N_{IBM} . HCE stands for halo-cell exchange.

type	mpi directive	required by	calls/RK step	comments
1-point HCE	<code>mpi_sendrecv</code>	finite-differences	4	(u, v, w and p)
2-point HCE	<code>mpi_sendrecv</code>	IBM forcing scheme	$3 \times 2 \times N_{\text{IBM}}$	(u^*, v^*, w^*)
transpose	<code>mpi_all_to_all</code>	Poisson solver	6	see algorithm 2

Figure 2.6 quantifies the scaling efficiency of our numerical algorithm for a case with the computational parameters in table 2.2. The simulations are performed in a three-dimensional domain discretized in a regular grid; periodic boundary conditions are imposed in the streamwise and spanwise directions, together with no-slip/no-penetration conditions in both walls. Both panels are normalized such that values above 0 mean a deterioration with respect to ideal scaling, and below 0 an improvement. A strong scaling test keeps the same mesh and number of particles, while varying the number of computational subdomains; weak scaling varies the number of computational subdomains and changes the mesh and number of particles such that the number of Eulerian and Lagrangian grid points per subdomain is fixed. Timings were computed with the function `mpi_wtime()`, averaged for 50 timesteps of the numerical algorithm. Computations were performed in the thin (*Ivy Bridge*) nodes of the Dutch national supercomputer Cartesius, in Amsterdam.

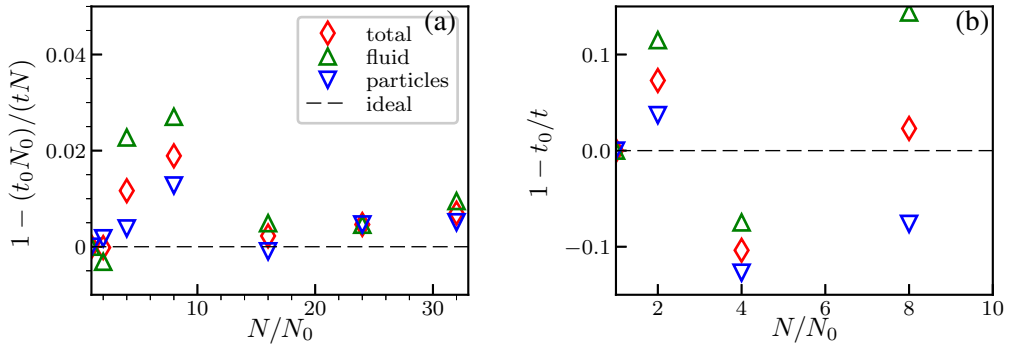


Figure 2.6: Strong (a) and weak (b) scaling deterioration of the numerical algorithm for the case in table 2.2. t and N denote the elapsed wall-clock time and corresponding number of tasks. $N_0 = 24$ and t_0 correspond to the minimum number of tasks, and respective elapsed wall-clock time. Values above the dashed line correspond to sublinear and below to superlinear scaling.

We achieved, with a distributed-memory parallelization, satisfactory timings for the typical problem sizes that was interesting to tackle in this research. We therefore decided not to analyze here the scaling performance of the hybrid MPI-OpenMP implementation.

Table 2.2: Computational parameters used for the scaling study. Weak scaling was performed by changing N_x , N_y and N_p , such that $N_x \times N_y \times N_z / (N_1 \times N_2)$ and $N_p / (N_1 \times N_2)$ is constant. The resolution was set such $D_p / \Delta x = 16$, corresponding to 746 Lagrangian grid points. We recall that N_1 and N_2 correspond to the number of computational subdomains in x and y , respectively.

scaling test	$N_x \times N_y \times N_z$	N_p	$(N_x/N_1) \times (N_y/N_2)$	$N_p / (N_1 \times N_2)$
strong	$768 \times 768 \times 384$	22 000	varied	varied
weak	(varied) \times (varied) \times 384	varied	768×768	22 000

Overall the scaling performance of the code proves to be good, showing at most 3% deterioration, and what seems to be a *cache effect* at around $N/N_0 = 16$, corresponding to a number of tasks $N = 384$. Both fluid- and particle-related computations eventually show some performance deterioration with increasing number of CPUs. Performance deterioration in particle treatment is caused by the `mpi_sendrecv` calls for updating the 2-cell halo regions, required by the IBM. Note that the multi-direct forcing scheme multiplies the required number of calls by $6N_s$ halo exchanges per time step. This becomes clear in the weak scaling tests – here the size of the computational subdomains remains fixed, and the scaling of the particle treatment is close to ideal (even exceeding ideal performance, likely due to cache effects). The same cannot be stated for the treatment of the fluid phase. Here halo-cell exchange is not as demanding as in the IBM algorithm, as the regions only

span 1 cell, and the associated directives are only called 4 times per RK3 step. The deterioration in performance comes from the *all-to-all* operations in the Poisson solver, clearly the most communication-intensive part of the numerical algorithm. The solver low computational demand, together with the communication load are such that its efficiency must drop when the computational load per CPU is not sufficiently high.

Despite the loss in efficiency associated with the fast Poisson solver, the numerical algorithm still shows close to ideal scaling for relatively large problems, and as will be shown below, performs well compared to other state-of-the-art implementations.

2.5.5 BENCHMARK – NUMERICAL SIMULATION OF PARTICLE-LADEN DECAYING HOMOGENEOUS ISOTROPIC TURBULENCE

We simulated particle-laden decaying homogeneous isotropic turbulence (HIT) laden with finite-size particles. Our simulations are compared to the ones of different groups, which simulated the same flow with different numerical approaches¹¹. We use this as an assessment of the computational performance of our numerical algorithm, as it is compared with other state-of-the-art methods: a lattice-Boltzmann method (LBM) used e.g. in [36, 37] and a viscous penalization method (VoF-Lag) used e.g. in [107, 144]. We must note that the version of the code used here is different from the one for which the scaling tests were performed. At the time of this workshop, communication of particle-related data through Eulerian halo regions was not implemented yet, and therefore particle treatment was slowed down, and its scaling deteriorated.

The initial condition is a single-phase turbulent flow field computed from a pseudo-spectral DNS code (with Taylor-based Reynolds number $Re_\lambda = 87$), linearly-interpolated to our staggered mesh, and a pseudo-random distribution of particle positions. Particle initial linear velocities were obtained from a trilinear interpolation from the fluid velocity grid cells closest to its centroid, while angular velocity was set to zero. Other physical and computational parameters are shown in table 2.3 and its caption.

Two cases were considered, with particle sizes varying by a factor of two, number of grid points over the particle diameter fixed to $D_p/\Delta x = 12$, while keeping the volume fraction fixed to $\Phi = 0.03$ and mass density ratio $\rho_p/\rho_f = 4$, clearly a 4-way coupling regime. We should note that the fluid-phase is over-resolved, thereby focusing differences in observables to different approaches to particle-fluid/particle-particle coupling. This case is particularly well-suited for our method as the grid can be regular without over-/under-resolving the flow in a particular direction, and it is an inertia-dominated flow.

¹¹ The simulations were performed in the framework of the workshop *High Performance Computations for Fluid Dynamics Interface treatment and finite size particles – Interface treatment and finite size particles* held in November 2014 in Toulouse. The workshop was organized by the Institut de Mécanique des Fluides de Toulouse (IMFT) and the center CALcul en MIDI Pyrénées (CALMIP). Groups with different approaches for simulating interface-resolved particle-laden turbulent flows simulated the same benchmark case.

Hereafter we show some basic statistics, followed by some notes on the physical and computational performance of the methods.

Table 2.3: Computational setup for DNS of decaying HIT laden with finite-size particles. Common features of the laden cases are: a fixed volume fraction $\Phi = 0.03$, lubrication closures switched off, frictionless particles, mass density ratio $\rho_p/\rho_f = 4$, and a dry normal coefficient of restitution $e_{dry} = 0.97$.

case	N^3	N_p	D_p/η	$\eta/\Delta x$
SPH-0512	512^3	–	–	0.81
SPH-1024	512^3	–	–	1.64
MPH-0512	1024^3	4 450	19.7	0.81
MPH-1024	1024^3	36 502	9.8	1.64

Figure 2.7 presents a visualization of the flow-field, where the particles are also rendered. Isosurfaces of Q -criterion (Q being the second invariant of the fluid velocity gradient tensor) and low pressure regions [66] to depict respectively small and large-scale coherent structures (see the figure caption for details). The multiscale character of the flow is evident, and the size of turbulence scales compares to the one of the particle size, justifying the interface-resolved simulation.

The decay of particle linear ($\langle u_i^2 \rangle / 2$) and angular kinetic ($\langle \omega_i^2 \rangle / 2$) energy, normalized by their maximum values are depicted in figure 2.8. Particles adapt relatively fast to the initial vorticity field, reaching on average a maximum of angular TKE in about one eddy turnover time. Larger particles reach this peak at later times due to their larger moment of inertia. Notice the cross-over between the particle linear TKE for the two cases (see the inset in the figure, where the difference between the two is computed). First, for sufficiently high turbulence intensity, smaller particles loose energy faster than larger particles, hinting on the effect that smaller particle inertia dominates over the smaller surface area. At $t \approx 2T_e$ this tendency reverts: energy decays faster for the largest particles. Since here viscous effects are dominant, larger surface area is the dominant factor determining the rate of decay. Decreasing importance of viscous effects can be appreciated in the conditionally-averaged flow conforming a single-particle, computed from the following procedure presented in algorithm 6, similar to [25, 107]. The contours of slip velocity show a smaller magnitude (even scaled with the global particle velocity rms), and a wake with a much less elongated shape. Clearly, at late times the particle Reynolds number is sufficiently small that viscous effects are ought to be the main mechanism driving the decay of TKE.

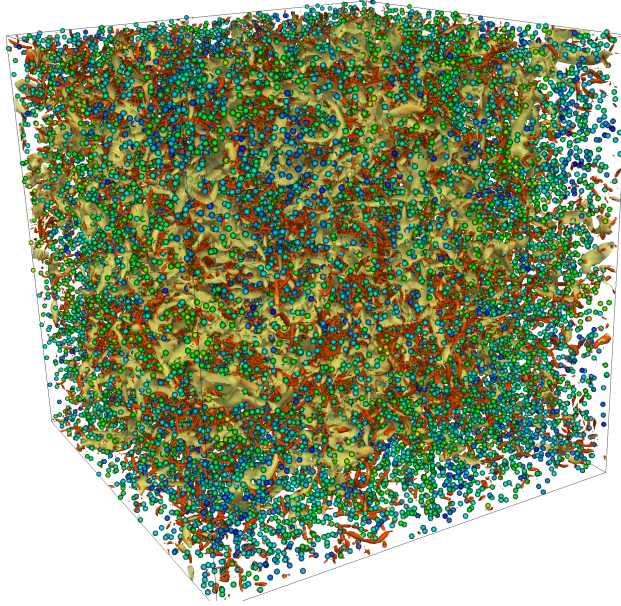


Figure 2.7: Visualization of particle-laden decaying HIT. Particles are colored by their linear velocity (green-high and blue-low). Red denotes iso-surfaces of constant Q , while translucent yellow iso-surfaces of low pressure regions.

Algorithm 6 Procedure for computing the average flow around a particle.

- 1: mask fluid flow inside particles with a phase-indicator function ϕ ;
 - 2: interpolate $\phi \mathbf{u}$ and ϕ to a Lagrangian grid in a spherical shell with radius $R_{\text{av}} = 4R$;
 - 3: compute phase-averaged fluid flow velocity to the Lagrangian grid $\mathbf{U}_f = \sum_l \Phi \mathbf{U} / \sum_l \Phi$;
 - 4: compute particle-to-fluid apparent slip velocity $\mathbf{U}_s = \mathbf{U}_f - \mathbf{U}_p$ with \mathbf{U}_p the particle velocity;
 - 5: define a spherical averaging volume, with origin aligned with \mathbf{U}_s ;
 - 6: compute phase-averaged fluid velocity in this volume for all the particles, and ensemble-average;
 - 7: average result along the (statistically homogeneous) azimuthal direction.
-

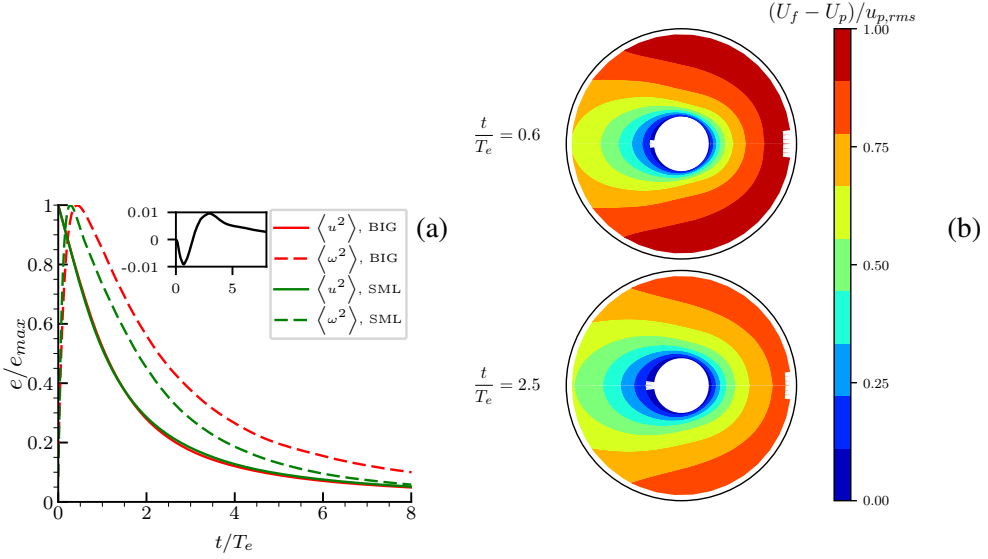


Figure 2.8: Temporal decay of particle linear and angular kinetic energy, both normalized by its maximum value. The inset shows the difference between the decay of linear TKE of the large and small particles (a). Conditionally-averaged profile of fluid velocity conforming a particle (b) for $t = 0.6T_e$ (top), and $t = 2.5T_e$ (bottom). In a reference frame moving with the particle, the flow is from right to left; blue–low and red–high.

Figure 2.9 presents the longitudinal 1D energy spectra for both laden and unladen cases defined as:

$$E_{ii}(k) = \frac{1}{N_i} \sum_{n=0}^{N_i/2} \rho_{ii}(\Delta x) e^{-2\pi i k \Delta x / L_i}, \quad k = [0, 1, \dots, N_i/2] \quad (2.19)$$

with ρ_{ii} being the longitudinal autocorrelation over direction i , and N_i being the number of grid points over the i direction. The spectra were averaged in space and over the three domain components. Since the flow is relatively dilute, we computed the auto-correlation function over the entire Eulerian field, even within the domain inside the particles. The results show the same trend as observed in [93], that particles decrease the energy content at large scales, observation attributed to increasing dissipation, and increase it at small scales, due their energy-producing wakes. Notice that this change in trend occurs at wave numbers $\kappa \sim D_p^{-1}$.

Let us now compare some results for the different numerical approaches. First we investigate the decay of fluid TKE for single-phase flow. Curves pertaining to the IBM algorithm show good agreement with the spectral simulations over the entire range of time scales, despite an under-prediction at time scales smaller than one eddy turnover time. Since the results seem to be already grid-independent, we attribute this difference to the trilinear interpolation used to initialize the flow-field (provided in a collocated grid) in

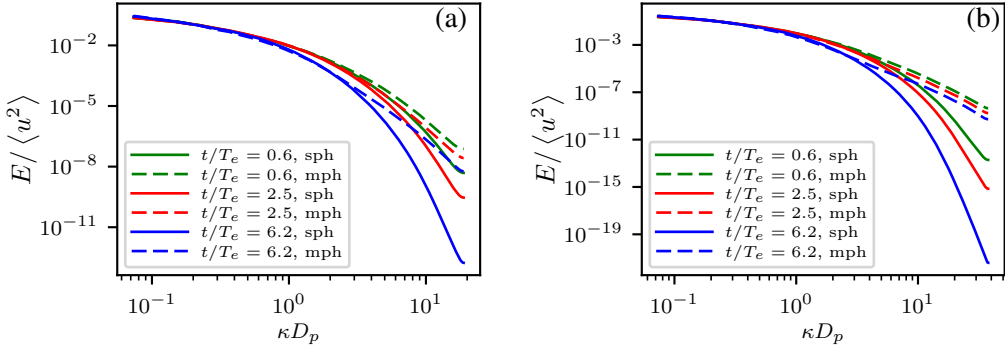


Figure 2.9: Longitudinal 1D energy spectra for cases MPH-0512 (a) and MPH-1024 (b), normalized by the velocity variance. The wave number in the horizontal axis is made non-dimensional by the particle size D_p . sph – single phase cases, mph – multiphase cases.

a staggered MAC arrangement. The same under-prediction is more evident in the VoF-Lag approach, which still captures well the final period of decay where viscous effects dominate, well-fitted by $\langle E \rangle \sim (t/T_e)^{-10/7}$ [12]. Since both methods are second-order accurate in space, differences can be attributed to the different temporal discretization or a less converged solution of the pressure Poisson equation for the latter approach (note that the IBM approach uses a direct, and the VoF-Lag an iterative solver, with a tolerance for residual of velocity divergence equal to 10^{-3} of its r.m.s.). The results pertaining to the LBM show the opposite trend: a good agreement at small time scales which degrades at higher turnover times. Notice that the LBM approach uses a collocated grid, and therefore does not require any sort of interpolation of the initial velocity field. For this method, differences to the spectral solver during the viscous region is largest, perhaps an effect of formally solving a weakly-compressible formulation of the Navier-Stokes equations. Despite this, for the region where the turbulence intensity remains high, the LBM approach also compares well to the spectral solution. As it can be seen in panel (b) of the same figure, the decay for the particle-laden simulations is biased by these discrepancies. Therefore, finer comparison between approaches, using e.g. conditional statistics like in figure 2.8(b) should be performed in a future study.

Figure 2.11 compares the computational performance of the different approaches. For the current configuration, the IBM approach performed best in terms of computing time. Both the IBM and LBM do not achieve perfect scalability, even though the LBM code seems to improve the computational performance at ~ 2000 CPU, resembling a cache memory effect. In the IBM and LBM approaches the difference between the load due to a single-phase and multi-phase simulation are of the same order of magnitude. The VoF-Lag approach shows almost an order of magnitude difference between the laden and unladen cases. The high computational cost for this method could be explained by two factors. First, the semi-implicit iterative solver used to solve the mass and momentum equations is more expensive than the time splitting used in classical Navier-Stokes solvers.

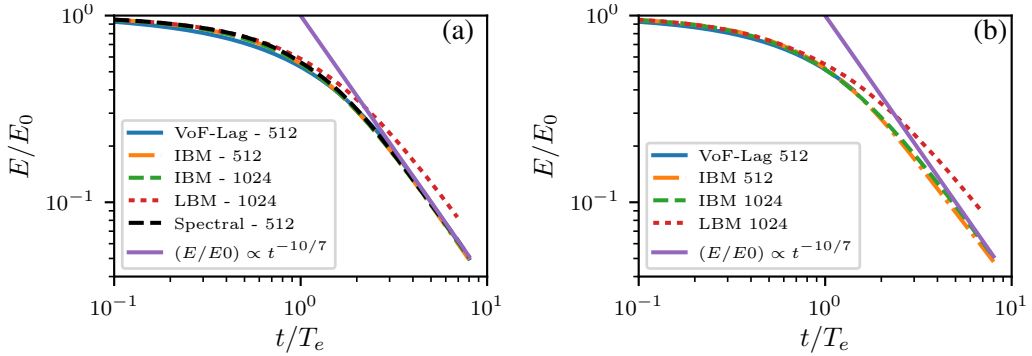


Figure 2.10: Comparison of the total decay of TKE for the single-phase cases sph (a) and multi-phase cases mph (b).

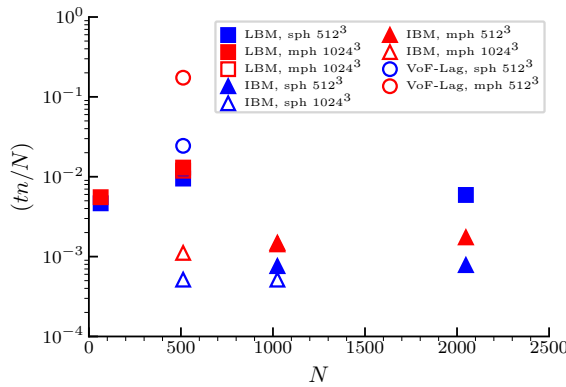


Figure 2.11: Wall-clock time in seconds normalized by the number of cores N ; Ideal scaling should follow a horizontal line.

The advantage of this solver is that it can handle larger time steps, not being limited by the viscous CFL number in very viscous flows. However, in this inertia-dominated flow, the time-step is dictated by the advective stability restriction. Second, when the particle laden case is considered, the CPU time becomes about one order of magnitude higher. This increase is explained by two factors. First of all, for stability reasons the time step is divided by a factor of two. Second, the update of the physical characteristics takes 67% of the simulation. That includes the transport of the particles, update of the color function, and the of the viscosity and density, equations.

To summarize, this is an example of a problem that is particularly well-suited for our method. All the methods were able to simulate this complex flow successfully; achieving such state-of-the-art simulations with $O(10^4)$ particles is a computational achievement that only few groups can reach.

ACKNOWLEDGMENTS

We acknowledge Jorge Brändle for inviting us to participate in the workshop that led to these results and the fruitful discussions. Jos Derksen is also acknowledged for the fruitful discussions during this collaboration. Nicolas Renon from CALMIP is kindly acknowledged for assisting us with porting the code to the supercomputer EOS.

3

COLLISION MODELING

This chapter is adapted from P. Costa et al. “Collision model for fully resolved simulations of flows laden with finite-size particles.” In: *Phys. Rev. E* 92 (5 Nov. 2015), p. 053012.

3.1 INTRODUCTION

Studying flows laden with finite-size particles using interface-resolved direct numerical simulations (DNS) has recently become possible with the development of efficient numerical methods, such as immersed boundary methods [7], together with the continuous increase in computing power. Such simulations provide detailed insight in the flow dynamics at the particle scale and beyond. The governing equations for the fluid phase and the particles are directly coupled with each other through the no-slip/no-penetration condition at the particle surface (i.e., 2-way coupling), without the need of parameterizing the drag force between the phases. Also, long-range hydrodynamic interactions between particles (i.e., 4-way coupling) are naturally reproduced by these methods. However, when the particle volume fraction is high, additional models are required to account for short-range hydrodynamic solid-solid interactions (lubrication forces) and solid-solid contacts. Otherwise, the realism of the simulation may be compromised by a poor description of these interactions. For instance, by under-predicting lubrication-enhanced clustering of inertial particles, as observed for homogeneous isotropic turbulent flows [136]. The challenge is to find a model able to reproduce short-range particle-particle and particle-wall interactions with the required realism and with little effect on the computational efficiency of the overall numerical algorithm.

We consider non-Brownian spherical particles, which are sufficiently large such that inter-surface forces as the Van der Waals force and the electrostatic double-layer force can be neglected [55]. Also, cohesive forces, which are relevant for wet granular media [56], are disregarded. We restrict the applicability of the model to cases where 4-way coupling is required, but where the solid volume fraction is not extremely high such that good description of the macroscopic outcome of the collision (i.e., relative velocity prior to and after contact) is sufficient to model the suspension dynamics.

Much work has been done in modeling of inter-particle (or particle-wall) collisions. Discrete element methods (DEM) have been successfully used to account for inter-particle collisions in simulations of gas-solid flows where hydrodynamic interactions between particles are negligible (e.g., [31], [140] and [63]). These collisions are often referred to as *dry* collisions. More recently, some studies used these same collision models for reproducing particle-particle and particle-wall interactions in viscous liquids, commonly referred to as *wet* collisions. In this case, fluid effects such as added mass, viscous dissipation and history forces become important [54].

Typically, lubrication interactions in interface-resolved simulations cannot be resolved by the overall numerical method (not without resorting to excessive grid refinement). This lack of spatial resolution can be circumvented by a closure model for lubrication interactions based on analytical solutions of these interactions in the Stokes regime (e.g., [135], [17], [77] and [106]).

Many studies used variants of the soft-sphere collision model of Cundall and Strack [31] to compute the contact forces, because of its computational advantages for simulating

dense suspensions when compared to hard-sphere models [35]. In the soft-sphere model, the normal force acting on the particle during a collision is computed from an equivalent linear spring-dashpot system in which the spring stiffness and dashpot coefficients are parameterized as function of the particle elastic properties. A limitation of this approach when applied to particle-laden flows is that the collision must be resolved with a time step that can be several orders of magnitude smaller than the time step of the Navier-Stokes solver for the fluid flow. This happens because the characteristic time scale of solid-solid contact is in general orders of magnitude smaller than the smallest time scale present in the flow [61, 87]. However, it is possible to artificially stretch the collision time to a multiple of the time step with which the particle motion is integrated. In some studies this was done by decreasing the value of the spring stiffness and checking resulting the collision time in a trial and error procedure [44]. This approach was avoided by others, who prescribed the desired collision time and computed the corresponding collision parameters by solving the equations of the spring-dashpot system (e.g., [17, 77, 106]).

Experimental studies have shown that fluid effects in the normal collision of a sphere onto a plane wall can be quantified by an *effective* normal coefficient of restitution, e_n , defined as the ratio of the magnitudes of rebound and impact velocities. In particular, when experimental data of $e_n/e_{n,d}$ (where $e_{n,d}$ is defined in an analogous way as e_n but for a collision in a dry system) are plotted against the particle impact Stokes number, $St \equiv (1/9)\rho_p U_p D_p / \mu$ (where ρ_p , U_p , D_p and μ are respectively the particle mass density, impact velocity, diameter and the fluid dynamic viscosity), the datasets for different fluids and particle types collapse in the same curve [87]. This suggests that e_n , $e_{n,d}$ and St are key parameters to describe a head-on wet collision. Hence, reproducing this scaling is an important test for which any numerical method for resolving the flow conforming a particle combined with a collision model should pass.

Several authors have been able to reproduce it with different methodologies for resolving the particle-fluid interface, such as tensorial penalty methods [106], Lagrange multiplier-based methods [2] or IBM [17, 68, 79, 91]. However, this benchmark relies on a definition of impact and rebound velocities, which vary significantly in these references [68]. Hence, if one solely resorts to this simple validation benchmark without careful comparison with experimental data, it can happen that the definitions of the impact and rebound velocities determined from the numerical simulation are not consistent with the measured quantities.

The complexity of the problem increases when the collision is oblique. In this case, the relative motion between the contact surfaces has a tangential component. Two different kinds of motion can occur between the surfaces in contact: rolling and sliding. Rolling occurs when a point of contact has zero relative velocity with respect to the contact surface, otherwise sliding occurs. Moreover, when a particle flowing through a viscous liquid approaches a planar surface obliquely, it experiences not only lubrication forces due to the squeezing motion of the fluid through the gap, but also forces and torques due to relative translational and rotational shearing (see e.g. [32] for a review). Finally, the frictional re-

sistance of the contact surface in the presence of a viscous liquid can change abruptly due to piezoviscous effects when smooth particles collide obliquely [73].

To the best of our knowledge, Kempe and Fröhlich [77] report the only collision model validated against experimental data of oblique particle-wall collisions in viscous liquids and against bouncing trajectories of particles colliding onto a planar surface in a viscous liquid. The latter benchmark validation is particularly interesting to reproduce, because it does not rely on definitions of impact and rebound velocities. It therefore gives a finer indication of the success of the model to reproduce the canonical case of a particle-wall collision than reproducing data of $e_n/e_{n,d}$ vs St. Kempe and Fröhlich [77] computed the normal collision force from a non-linear spring-dashpot system. This was done so that the force-displacement relation agrees with Hertzian contact theory. The collision time was stretched by using a numerical procedure to solve the resulting equations of the non-linear oscillator. For the tangential component, they developed a model based on the assumption that, throughout solid contact, a particle either rolls or slides, depending on the particles' incidence angle. Although the approach of considering pure rolling for small incidence angles does not reproduce collisions with recoil of the contact point, their methodology can be easily adapted to account for it. Even though their model is able to reproduce normal and oblique collisions in viscous liquids with satisfactory realism, the fact that it needs an extra iterative procedure to deal with the non-linear spring when computing the normal force may deteriorate its computational performance for denser concentrations. Furthermore, the force law for the tangential component of the collision force depends on the particles' incidence angle, which is difficult to interpret, e.g., for cases in which geometrical constraints force sustained contact.

We present a model for wet particle-particle and particle-wall collisions in fully-resolved simulations of particle-laden flows. We show that a simple variant of a linear spring-dashpot model capable of stretching the collision time [17, 63] suffices for computing contact forces. This contact model can be seen as a linearized version of Hertz contact theory, and its choice is motivated by a separation between time scales of solid-solid contact and the typical particle response time. The advantage of using this model is that its parameters can be analytically determined from well-documented material properties and a desired collision time, which is computationally attractive. Moreover, it accounts for stick-slip effects at the contact point without requiring explicit definition of impact and rebound angles. Oblique collisions with recoil are explicitly accounted for by using a tangential coefficient of restitution e_t as input parameter. This contact force model is implemented in an efficient and second-order accurate IBM for particle laden flows developed in [18] and combined with a physical model for lubrication interactions and roughness effects. We found the experimental data used by Kempe and Fröhlich [77] to validate their approach to be a good set of tests for which a physically realistic collision model should pass. We therefore validated our collision model against those distinct experimental cases which include the trajectory of a sphere colliding onto a planar surface in a viscous liquid [54], head-on particle-particle collisions [151] and data on oblique particle-wall collisions [73].

This chapter is organized as follows. Section 3.2 presents a brief overview of the physics of dry collisions of elastic spheres (subsection 3.2.1) followed by the description of the methodology for computing contact force/torques (subsection 3.2.2). Subsection 3.3 addresses the effects of the interstitial fluid in a wet collision and our modeling strategy for lubrication interactions. The numerical implementation is addressed in section 3.4. Section 5.3 explores the consequences of excessive and insufficient stretching of the collision time and presents the validation of the model against several benchmark experiments. Finally, in section 3.6 the conclusions and outlook are given.

3.2 DRY COLLISIONS

3.2.1 PHYSICS

When head-on inter-particle collisions take place in the absence of a viscous fluid, only the contact mechanics dissipate kinetic energy. This energy loss can be described by a *dry* coefficient of restitution, $e_{n,d}$, defined as the ratio of the relative rebound to relative impact velocities. The collision is referred to as oblique when the particles approach each other with an incidence angle just prior to contact ϕ_{in} and bounce with a rebound angle ϕ_{out} , as illustrated in figure 3.1. From these, it is convenient to define *effective* angles of

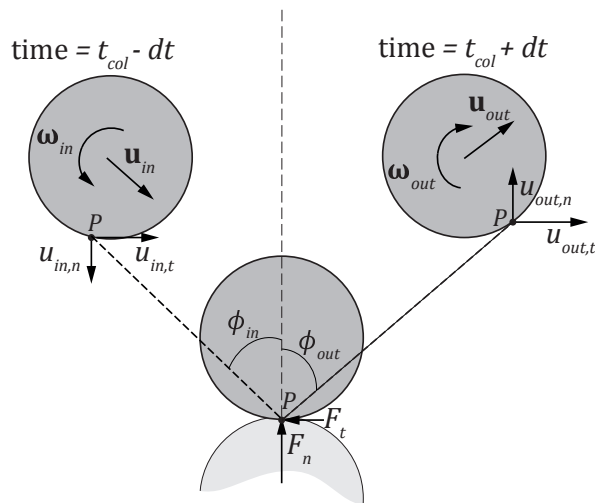


Figure 3.1: Schematic representation of an oblique inter-particle collision. For the sake of clarity we considered in this figure a reference frame moving with the light grey particle, which implies that the velocities sketched are relative velocities. F_n and F_t denote the normal and tangential component of the collision force.

incidence and rebound, respectively as,

$$\Psi_{\text{in}} = \frac{u_{\text{in},t}}{u_{\text{in},n}} = \tan(\phi_{\text{in}}), \text{ and} \quad (3.1)$$

$$\Psi_{\text{out}} = \frac{u_{\text{out},t}}{u_{\text{in},n}} = e_{n,d} \tan(\phi_{\text{out}}), \quad (3.2)$$

with the normal dry coefficient of restitution $e_{n,d}$ given by

$$e_{n,d} = \frac{u_{\text{out},n}}{u_{\text{in},n}}. \quad (3.3)$$

Maw, Barber, and Fawcett [98] explored this problem in detail. They used Hertzian contact theory to obtain the normal component of the collision force and velocity. Moreover, they assumed particles of the same material for which the contact area consists of stick and slip regions, and that slip could be modeled by a constant coefficient of sliding friction, μ_c . Their results show that three different types of impacts can occur, depending on the value of the following normalized incidence angle,

$$\psi_{\text{in}} = \frac{2}{\mu_c} \frac{1-\nu}{2-\nu} \Psi_{\text{in}}, \quad (3.4)$$

and the material- and geometry-dependent parameter,

$$\chi = \left(1 + \frac{1}{K^2}\right) \frac{1-\nu}{2-\nu}, \quad (3.5)$$

where ν is the Poisson's ratio and K the normalized particle radius of gyration ($K^2 = 2/5$ for a homogeneous solid sphere). Figure 3.2 shows ψ_{out} as a function of ψ_{in} as computed in their model, where ψ_{out} is the normalized rebound angle, defined analogously to ψ_{in} as,

$$\psi_{\text{out}} = \frac{2}{\mu_c} \frac{1-\nu}{2-\nu} \Psi_{\text{out}}. \quad (3.6)$$

The numerical solution of this model yields three distinct regions denoted in figure 3.2 by I, II and III. First, for small incidence angles, $\psi_{\text{in}} \leq 1$, the sphere sticks during contact because the normal component of the load is much larger than the tangential component. When the contact surface starts to shrink, small regions of micro-slip may occur due to tangential elastic recovery, which can spread throughout the entire contact area, leading to gross slip. Second, for an intermediate range of incidence angles, $1 < \psi_{\text{in}} \leq 4\chi - 1$, the collision starts with gross slip, but the frictional stresses retard the tangential velocity, which rapidly drops to zero in the entire contact area (full stick). Finally, for higher incidence angles, $\psi_{\text{in}} > 4\chi - 1$, the tangential component of the load is even higher and gross slip occurs throughout the contact time.

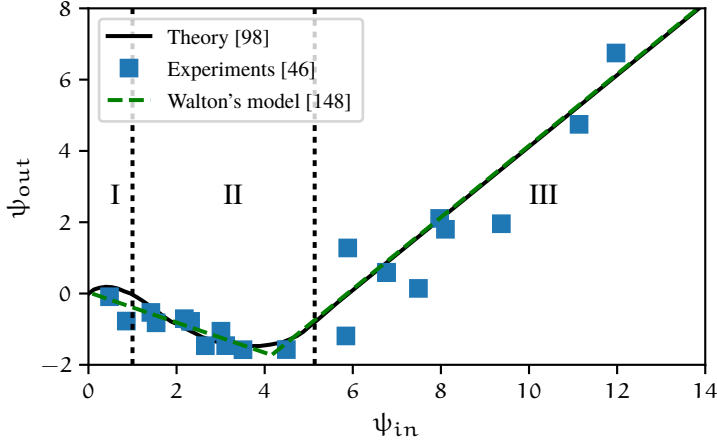


Figure 3.2: Numerical solution of the model of Maw, Barber, and Fawcett [98] for collisions between glass spheres, compared with experimental data of Foerster et al. [46] and the model of Walton [148]. The curve and experimental data were extracted from a curve Ψ_{out} vs Ψ_{in} of [46] and rescaled to ψ_{out} vs ψ_{in} with the parameters of their homogeneous 3mm glass spheres, $\nu = 0.22$ and $\mu_c = 0.092$. The two vertical dotted lines delimit the three different types of impact and are given by $\psi_{in} = 1$ and $\psi_{in} = 4\chi - 1 \approx 4.2$.

Walton [148] proposed a simplified hard-sphere model with three parameters: (1) a normal coefficient of restitution, $e_{n,d}$; (2) a tangential coefficient of restitution for non-sliding contact, $e_{t,d}$, defined as,

$$e_{t,d} \equiv -\frac{u_{out,t}}{u_{in,t}} = -\frac{\Psi_{out}}{\Psi_{in}}; \quad (3.7)$$

and (3) a coefficient of sliding friction, μ_c , to model the tangential component of the load acting on the particle when it is sliding:

$$F_t = -\mu_c |F_n|, \quad (3.8)$$

where F_n is the normal component of the contact force. This model assumes that the collision force acts at a single point and can be decomposed into a normal and tangential component. Moreover, it assumes that throughout the collision time the regime is either full stick or gross slip. From these three parameters, one can define the two lines which dictate the collision regime:

$$\Psi_{out} = \begin{cases} -e_{t,d} \Psi_{in}, & \Psi_{in} \leq \Psi_{in}^* \quad (\text{stick}), & (3.9a) \\ \Psi_{in} - \mu_c (1 + 1/K^2) (1 + e_{n,d}), & \Psi_{in} > \Psi_{in}^* \quad (\text{slip}), & (3.9b) \end{cases}$$

where eq. (3.9a) is obtained directly from the definition of $e_{t,d}$, and eq. (3.9b) by applying the definition of coefficient of sliding friction to relate the normal and tangential momen-

tum impulses. Ψ_{in}^* is the incidence angle above which the collision regime changes from full stick into gross slip:

$$\Psi_{\text{out}}(\Psi_{\text{in}}^{*+}) = \Psi_{\text{out}}(\Psi_{\text{in}}^{*-}) \Leftrightarrow \Psi_{\text{in}}^* = \mu_c \left(1 + \frac{1}{K^2} \right) \frac{1 + e_{n,d}}{1 + e_{t,d}}. \quad (3.10)$$

The two models differ most significantly in the intermediate region of incidence angles, for which there may be periods of full stick and gross slip throughout the contact. Despite these differences, the simplified approach is able to reproduce experimental data reasonably well, as shown, e.g., in [148], [46] (figure 3.2) and [73]. The minimalistic nature Walton's model makes it an attractive choice for problems where a detailed description of the contact mechanics is not required, which is in general the case for particle-laden flows.

3.2.2 MODELING

Collisions of spherical particles in a viscous liquid were shown to have a contact time larger but of the same order than the contact time in a dry system, predicted by Hertzian contact theory, see Legendre et al. [87]. The authors also showed that this contact time is four to five orders of magnitude smaller than the viscous relaxation time of the particle, depending on the impact Stokes number. This means that the particle experiences a collision as a *discontinuity* in its motion. Even when the characteristic time scale of the particle motion is not dictated by the viscous relaxation time, (e.g., due to geometrical constraints in a flow with high volume fraction of particles) this clear separation of time scales typically remains valid. Hence, we require that the collision dynamics are realistically reproduced from a *macroscale* perspective, i.e., realistic approach and rebound velocities and timescale small enough such that this separation of time scales is satisfied. Hence, it is convenient to use a model capable of stretching the collision time, so that the overall numerical algorithm is not significantly penalized by the overhead introduced by the integration of the particle equations of motion. Furthermore, it is convenient to use a model with parameters that can be easily measured experimentally, such as the parameters of Walton's model. Joseph and Hunt [73] successfully used this model to describe experimental data from wet oblique collisions of spherical particles onto planar surfaces, further supporting its validity to describe collisions in a viscous liquid.

We found the variant of the soft-sphere contact model of Tsuji, Kawaguchi, and Tanaka [140], described in [63] to be suitable for our problem. This approach has computational advantages for dense suspensions when compared to other alternatives such as hard-sphere models, and allows the collision time to be stretched. The model consists on a linear spring-dashpot system in the normal and tangential directions, with a Coulomb friction slider in the latter, as sketched in figure 3.3 (a). In the following we describe the model, with differences in the definition of the tangential unit vector and in the value to which the

tangential displacement is saturated. Figure 3.3 (b) illustrates the notation and reference frame adopted.

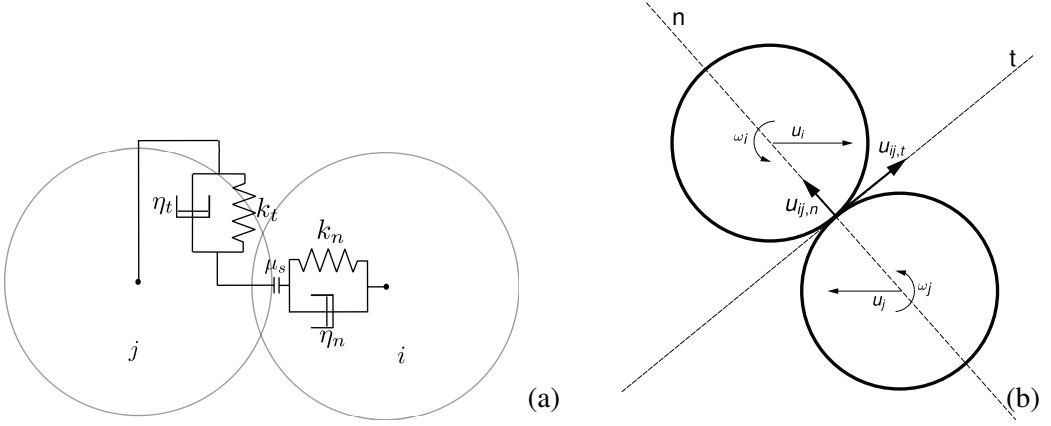


Figure 3.3: Linear spring-dashpot model (a). Notation and reference frame adopted for an inter-particle collision (b).

The normal force acting on particle i due to a contact with particle j , with a relative velocity at the contact point given by

$$\mathbf{u}_{ij} = (\mathbf{u}_i + \mathbf{R}_i \boldsymbol{\omega}_i \times \mathbf{n}_{ij}) - (\mathbf{u}_j + \mathbf{R}_j \boldsymbol{\omega}_j \times \mathbf{n}_{ij}), \quad (3.11)$$

is the component of the collision force that acts along the direction of the line-of-centers (figure 3.3 (b)),

$$\mathbf{n}_{ij} = \frac{\mathbf{x}_j - \mathbf{x}_i}{\|\mathbf{x}_j - \mathbf{x}_i\|}. \quad (3.12)$$

This collision force depends on the overlap distance between the two particles,

$$\delta_{ij,n} = (\mathbf{R}_i + \mathbf{R}_j - \|\mathbf{x}_j - \mathbf{x}_i\|) \mathbf{n}_{ij}, \quad (3.13)$$

and the normal relative velocity of the contact point,

$$\mathbf{u}_{ij,n} = (\mathbf{u}_{ij} \cdot \mathbf{n}_{ij}) \mathbf{n}_{ij}, \quad (3.14)$$

and is obtained from the equivalent linear spring-dashpot system:

$$\mathbf{F}_{ij,n} = -k_n \delta_{ij,n} - \eta_n \mathbf{u}_{ij,n}, \quad (3.15)$$

where k_n and η_n are the normal spring and dashpot coefficients, respectively. These are computed by solving for the motion of a linear harmonic oscillator [63], and requiring that there is no overlap at the end of the collision, $t = N\Delta t$,

$$(\delta_{ij,n} \cdot \mathbf{n}_{ij})|_{t=N\Delta t} = 0, \quad (3.16)$$

and that the velocity at the end of the collision is given by the definition of $e_{n,d}$,

$$(\mathbf{u}_{ij,n} \cdot \mathbf{n}_{ij})|_{t=N\Delta t} = -e_{n,d} (\mathbf{u}_{ij,n} \cdot \mathbf{n}_{ij})|_{t=0}. \quad (3.17)$$

Note that we define the collision time, T_n , as a multiple N of the time step of the overall numerical algorithm, Δt . This is convenient because – as our results will show – the outcome of a numerical simulation of a wet collision is more realistic if the fluid is allowed to adapt itself to the sudden changes in particle velocity. In practice, because T_n should be fixed during a collision, and Δt may vary in agreement with the stability criterion of the fluid solver, one should define the collision time as a multiple of the estimated time step of the numerical algorithm.

The coefficients read,

$$k_n = \frac{m_e (\pi^2 + \ln^2 e_{n,d})}{(N\Delta t)^2}, \quad \eta_n = -\frac{2m_e \ln e_{n,d}}{(N\Delta t)}, \quad (3.18)$$

where

$$m_e = (m_i^{-1} + m_j^{-1})^{-1} \quad (3.19)$$

is the reduced mass of the particles.

This approach can be seen as a linearized version of Hertzian contact theory. Since we model the collision as a discontinuity in the particle motion, it is sufficient to guarantee that the conditions specified in eq. (3.16) and eq. (3.17) are fulfilled and $N\Delta t$ is small enough that separation of time scales is satisfied. One advantage of using a linear system is that the spring and dash-pot constants can be determined analytically and a priori, which is computationally attractive. Notice that increasing the value of T_n reduces the spring stiffness, which makes the contact *softer*. This implies that excessive stretching of the collision time results in a large overlap between solid surfaces and consequently in an unrealistic delay of the particle rebound. On the other hand, the collision time should be sufficiently stretched so that the collision force is accurately resolved in time. We require that the maximum particle overlap, which is reached when the particles have zero relative velocity, $\delta_{ij,n}^{max} = \delta_{ij,n}|_{\mathbf{u}_{ij,n}=0}$, is much smaller than D_p :

$$T_n \ll T_n^* = \alpha \frac{D_p}{(\mathbf{u}_{ij} \cdot \mathbf{n}_{ij})|_{t=0}} e^{-(\arcsin(\pi/\alpha)/\pi)} \quad (3.20)$$

where $\alpha = \sqrt{\pi^2 + \ln^2(e_{n,d})}$ [63]. Alternatively, if applicable, one can require that the maximum overlap due to the particle's submerged weight ($\delta_{ij,n}^{max,g} = |1 - \rho_f/\rho_p|g/k_n$) is much smaller than D_p :

$$T_n \ll T_n^{*,g} = \sqrt{\frac{D_p}{g} \frac{\alpha^2}{|1 - \rho_f/\rho_p|}}. \quad (3.21)$$

The tangential force is obtained analogously to $\mathbf{F}_{ij,n}$, but now with a Coulomb friction model to account for sliding motion:

$$\mathbf{F}_{ij,t} = \min \left(\| -k_t \delta_{ij,t} - \eta_t \mathbf{u}_{ij,t} \|, \| -\mu_c \mathbf{F}_{ij,n} \| \right) \mathbf{t}_{ij} \quad (3.22)$$

where $\delta_{ij,t}$ is the tangential displacement and \mathbf{t}_{ij} the unit vector with the direction of the test force:

$$\mathbf{t}_{ij} = -\frac{k_t \delta_{ij,t} + \eta_t \mathbf{u}_{ij,t}}{\|k_t \delta_{ij,t} + \eta_t \mathbf{u}_{ij,t}\|}. \quad (3.23)$$

The coefficients k_t and η_t are obtained analogously by solving a harmonic oscillator for the tangential direction, and requiring that the definition of the tangential coefficient of restitution is fulfilled,

$$(\mathbf{u}_{ij,t} \cdot \mathbf{t}_{ij})|_{t=N\Delta t} = -e_{t,d} (\mathbf{u}_{ij,t} \cdot \mathbf{t}_{ij})|_{t=0}, \quad (3.24)$$

and matching the collision times in both directions ($T_t = T_n$). The values of the coefficients read,

$$k_t = \frac{m_{e,t} (\pi^2 + \ln^2 e_{t,d})}{(N\Delta t)^2}, \quad \eta_t = -\frac{2m_{e,t} \ln e_{t,d}}{(N\Delta t)}, \quad (3.25)$$

where the reduced mass of the system is given by:

$$m_{e,t} = (1 + 1/K^2)^{-1} m_e. \quad (3.26)$$

The tangential displacement of the contact point must be integrated in time from the imminence of contact. Integrating the relative tangential velocity at the point of contact yields,

$$\delta_{ij,t}^{*n+1} = \underline{\mathbf{R}} \cdot \delta_{ij,t}^n + \int_{t^n}^{t^{n+1}} \mathbf{u}_{ij,t} dt, \quad (3.27)$$

where $\underline{\mathbf{R}}$ is a rotation tensor which rotates $\delta_{ij,t}^n$ to the new local coordinate system at time level $n + 1$.

The tangential force becomes independent of the tangential displacement of the spring when the particle starts sliding (eq. (3.22)). If the tangential displacement is further incremented when the particle starts to slide, unrealistic results can be obtained if the collision regime changes subsequently to sticking [15]. Hence, the tangential displacement must be saturated in order to comply to Coulomb's condition whenever the collision is in the sliding regime [94]:

$$\delta_{ij,t}^{n+1} = \begin{cases} \delta_{ij,t}^{*n+1}, & \|\mathbf{F}_{ij,t}\| \leq \mu_c \|\mathbf{F}_{ij,n}\|, \\ (1/k_t) (-\mu_c \|\mathbf{F}_{ij,n}\| \mathbf{t}_{ij} - \eta_t \mathbf{u}_{ij,t}), & \|\mathbf{F}_{ij,t}\| > \mu_c \|\mathbf{F}_{ij,n}\|. \end{cases} \quad (3.28a)$$

$$(3.28b)$$

After computing the contact forces acting at the point of contact, we determine the equivalent force-couple system acting in the particle centroid:

$$\mathbf{F}_{ij}^c = \mathbf{F}_{ij,t} + \mathbf{F}_{ij,n}, \quad (3.29)$$

$$\mathbf{T}_{ij}^c = R_p (\mathbf{n}_{ij} \times \mathbf{F}_{ij,t}). \quad (3.30)$$

The total collision force and torque are the sum of contributions of all the particles in direct contact with the particle i :

$$\mathbf{F}_i^c = \sum_j \mathbf{F}_{ij}^c, \quad (3.31a)$$

$$\mathbf{T}_i^c = \sum_j \mathbf{T}_{ij}^c. \quad (3.31b)$$

Finally, a wall is treated as a semi-infinite spherical particle, which makes a particle-wall collision the limit case of a spherical particle with finite-radius, R_i , colliding onto a sphere with radius $R_j \rightarrow \infty$. The parameters for particle-wall collisions are therefore computed in an analogous way, but taking this limit. The reduced mass is now given by $m_e = m_i$ and the normal overlap by $\delta_{iw,n} = (R_i - \|\mathbf{x}_i - \mathbf{x}_w\|) \mathbf{n}_{iw}$ where \mathbf{n}_{iw} is the unit-vector perpendicular to the wall and \mathbf{x}_w the coordinate of the point of contact on the planar surface.

3.3 EFFECTS OF THE INTERSTITIAL FLUID

3.3.1 LUBRICATION EFFECTS

A particle immersed in a viscous liquid experiences lubrication effects when moving close to and with finite relative velocity to another particle or wall. Assuming a drainage of the intervening liquid film in the Stokes regime, the force acting on the particle has an analytical solution that diverges when the non-dimensional gap-width, $\varepsilon \equiv \delta_{ij,n}/R_p$, tends to zero [16]. Our IBM is able to reproduce this and other analytical solutions until a certain (small) value of ε . For smaller gap-widths ($\lesssim \Delta x$) the IBM under-predicts this force due to a lack of spatial grid resolution. An approach that has been adopted for these cases is to keep the grid fixed and use lubrication models based on asymptotic expansions of analytical solutions for the lubrication force in the Stokes regime to compensate this lack of spatial grid resolution (e.g. [17, 77, 106, 135]). Taking these effects into account has been proved to be important for computing realistic bouncing velocities in simulations of head-on particle-wall collisions in viscous fluids [77].

Lubrication theory shows that ideally smooth particles would not reach actual solid-solid contact. Even if one accounts for the particles' surface deformation due to the abrupt

increase of the pressure in the gap, the particles would not reach direct contact but a finite *closest distance of approach*, h_m [33]. However, particles may interact through their asperities, with typical size σ , before reaching a gap distance of h_m . Joseph et al. [74] observed larger scatter of their experimental data for wet head-on collisions of a spherical particle onto a planar surface when $\sigma > h_m$. They argued that the contact occurs through the asperities (which are irregularly oriented) before elastohydrodynamic lubrication effects become important. This reasoning justifies the approach used by several authors of setting the lubrication correction to zero for small gap-widths (e.g. [135], [77]) or making it independent of the gap-width [17].

The most relevant component of the lubrication forces acting on the particle is the squeezing force acting along the line-of-centers, because its dominant term is $\propto 1/\varepsilon$ in contrast to translational and rotational shearing, which diverge slower ($\propto \ln \varepsilon$) and even for a value of ε close to surface roughness have a milder effect in the particle dynamics. Test simulations showed that the latter mentioned lubrication corrections had little effect on the results for immersed oblique, particle-wall collisions and therefore we decided to neglect them in the present study.

We use a two-parameter model to account for normal lubrication interactions and roughness effects, as illustrated in figure 3.4. When a spherical particle approaches a planar surface/another particle, for a certain gap-width, $\varepsilon_{\Delta x}$, the IBM cannot resolve the lubrication force acting on the particle. Hence, for gap-widths smaller than $\varepsilon_{\Delta x}$, we correct the lubrication force acting on the particle by adding to the Newton-Euler equations $\Delta F_{\text{lub}} = -6\pi\mu R_p u_{ij,n} (\lambda(\varepsilon) - \lambda(\varepsilon_{\Delta x}))$, where the Stokes amplification factor λ is given by [71]:

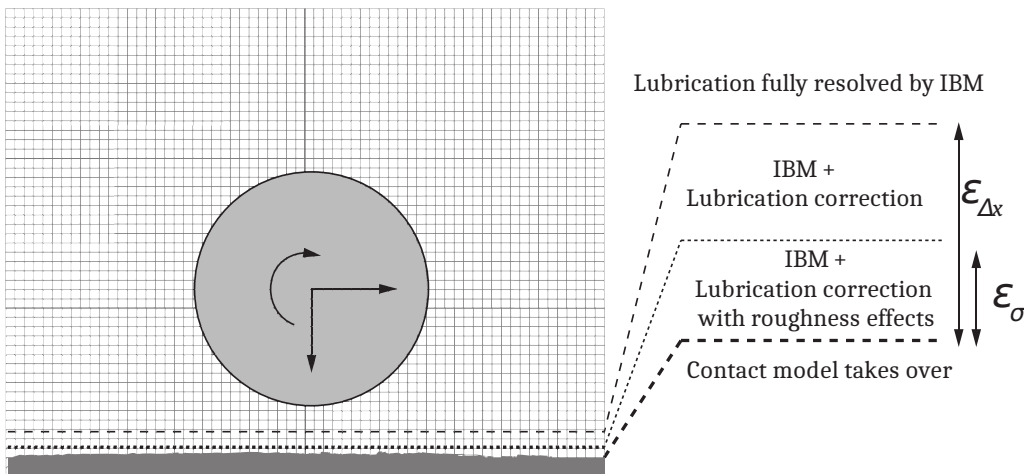


Figure 3.4: Schematic representation of the lubrication model. We illustrate the case of particle-wall interactions for the sake of simplicity. The model is analogous for particle-particle interactions.

$$\lambda_{pp}(\epsilon) = \frac{1}{2\epsilon} - \frac{9}{20} \ln \epsilon - \frac{3}{56} \epsilon \ln \epsilon + \mathcal{O}(1), \tag{3.32}$$

$$\lambda_{pw}(\epsilon) = \frac{1}{\epsilon} - \frac{1}{5} \ln \epsilon - \frac{1}{21} \epsilon \ln \epsilon + \mathcal{O}(1), \tag{3.33}$$

for lubrication interactions between two equal spheres, and between a sphere and a planar surface, respectively.

The value of $\epsilon_{\Delta x}$ can be determined by simulating the slow approach of a sphere towards a planar surface [16] or between two spheres [26] and determining up to which point the IBM is able to reproduce the lubrication interaction [17]. We illustrate this in figure 3.5 by comparing the analytical solution with the simulations without lubrication correction and with lubrication correction. The corresponding values of $\epsilon_{\Delta x}$ for two different spatial resolutions are given in table 3.1. To account for surface roughness, we saturate the Stokes

Table 3.1: Parameters for the lubrication model.

$D_p/\Delta x$	Interaction	$\epsilon_{\Delta x}$
16	particle-wall	0.075
16	particle-particle	0.025
32	particle-wall	0.05
32	particle-particle	0.025

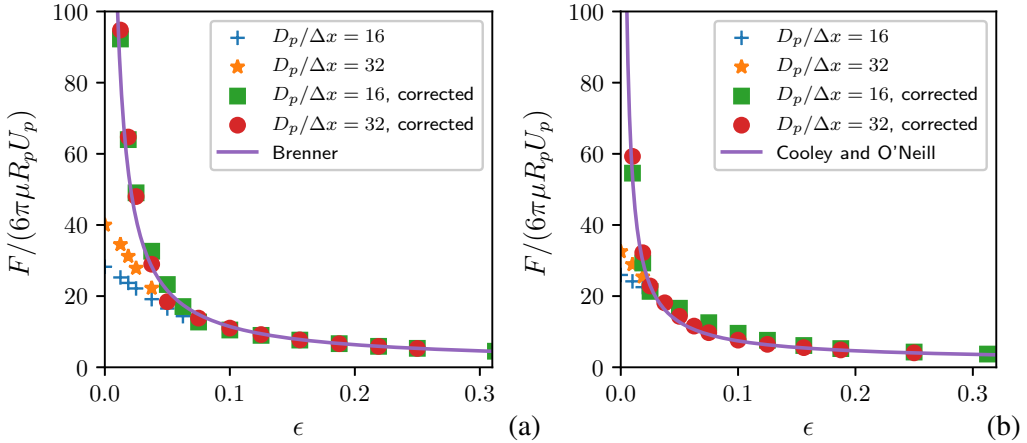


Figure 3.5: Lubrication corrections for the cases of normal particle-wall (a) and particle-particle (b) interactions, respectively compared against the analytical solution of Brenner [16] and Cooley and O’Neill [26]. Results shown for two different resolutions, $D_p/\Delta x = 16$ and 32.

amplification factor for gap-widths below a threshold ϵ_σ so that $\lambda(\epsilon < \epsilon_\sigma) = \lambda(\epsilon_\sigma)$. This

threshold value is related to the typical size of the asperities and was fixed to $\varepsilon_\sigma = 0.001$ for particle-wall interactions. We keep the Stokes amplification factor saturated until the surfaces overlap; then the collision force takes over. Hence, the force acting on the particle is corrected by ΔF_{lub} , given by:

$$\frac{\Delta F_{lub}}{-6\pi\mu R_p u_{ij,n}} = \begin{cases} \lambda(\varepsilon) - \lambda(\varepsilon_{\Delta x}), & \varepsilon_\sigma \leq \varepsilon < \varepsilon_{\Delta x} \\ \lambda(\varepsilon_\sigma) - \lambda(\varepsilon_{\Delta x}), & 0 \leq \varepsilon < \varepsilon_\sigma \\ 0, & \text{otherwise.} \end{cases} \quad (3.34)$$

For particle-wall collisions, the normal fluid-induced forces are set to zero for overlaps larger than the overlap due to the particle's submerged weight, $\delta_{ij,n}^g = |\rho_p - \rho_f|gV_p/k_n$, in order to avoid artificial dissipation due to the stretching of the collision time of the contact model. This procedure is not extended to particle-particle interactions, as it can cause significant artificial increase in the particles' acceleration for colliding particle pairs due to a sudden decrease in drag force.

3.3.2 PIEZOVISCOUS EFFECTS

Joseph and Hunt [73] performed experiments on wet, oblique collisions of spheres onto planar surfaces. They showed that the coefficient of sliding friction decreased by one order of magnitude when their smooth steel spheres collide, whereas it remained of the same order of magnitude ($\sim 15\%$ higher) for the case of rough glass spheres. They suggested that this abrupt decrease of the friction coefficient for smooth spheres was due to the fact that a characteristic piezoviscous length scale [8], h_{pv} , was larger than the average size of the asperities and therefore 'contact' occurs through the fluid, which is behaving like an elastic solid. Also, the slight increase in the coefficient of sliding friction for rough spheres was explained by the fact that the fluid introduces an extra resistance when the asperities have relative motion in the tangential direction. Figure 3.6 illustrates this effect. They developed a model capable of predicting the coefficient of sliding friction of smooth spheres colliding onto planar surfaces in a viscous liquid from elastohydrodynamic lubrication theory.

Hence, for the case in which piezoviscous effects are important, it does not suffice to use input parameters from dry collisions and lubrication corrections for obtaining a physically realistic result: the coefficient of sliding friction measured in a wet collision experiment, or predicted by the model developed in [73], $\mu_{c,wet}$, should be used.

3.4 NUMERICAL IMPLEMENTATION

The governing equations for the solid particles are advanced in time with the same Runge-Kutta scheme as used for the fluid phase, except for collision forces/torques and tangential displacement; these terms are integrated with a second-order Crank-Nicolson CN2

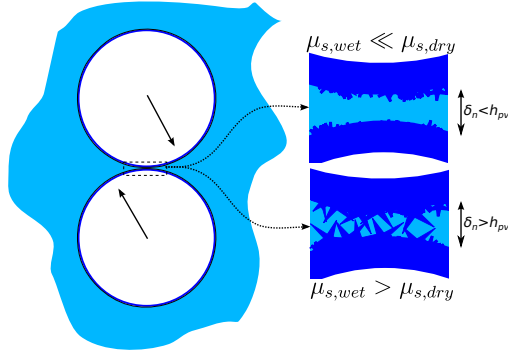


Figure 3.6: Illustration of piezoviscous effects during an oblique contact between two spheres. When the size of the asperities is smaller than the typical piezoviscous lengthscale, $\sigma < \delta_{pv}$, the effective coefficient of sliding friction $\mu_{c,wet}$ decreases. Otherwise, the $\mu_{c,wet}$ remains of the same order, or even slightly larger, due to the increased frictional resistance induced by the viscous fluid draining through the asperities.

scheme that has proven to return a stable and accurate integration. This scheme requires the contact force at the next time level, q , which depends on the values of the particle position and velocity at the same level (eq. (3.15) and eq. (3.22)). We therefore compute the contact force iteratively as a function of the particle position and velocity at q until the new particle position converges. The particles' position and velocity are initialized ($k = 0$) with the values of the previous time level $q - 1$. The advancement follows directly the integration of the Navier-Stokes equations, within the RK3 time advancement loop with a time step Δt_p which is allowed to be smaller than the time step of the Navier-Stokes solver Δt to ensure that the contact forces and lubrication force corrections are accurately integrated. The forces induced by the IBM are fixed in time while the sub-integrations are performed. For sub-stepping ratios $r_{\Delta t} = \Delta t / \Delta t_p$ ranging from 1 to $\mathcal{O}(100)$, the extra overhead introduced by the sub-stepping is negligible. The scheme is illustrated below.

$k = 0$

do

for all particles j in contact with particle i **do**

compute $\delta_{ij,n}^{q,k}$ and $\delta_{ij,t}^{q,k} = \underline{\mathbf{R}} \cdot \delta_{ij,t}^{q-1} + \frac{\Delta t_p^q}{2} (\mathbf{u}_{ij,t}^{q,k} + \underline{\mathbf{R}} \cdot \mathbf{u}_{ij,t}^{q-1})$

compute $\mathbf{F}_{ij,n}^{q,k}$ and $\mathbf{F}_{ij,t}^{q,k}$

update $\mathbf{F}_c^{q,k}$ and $\mathbf{T}_c^{q,k}$

end for

$$\mathbf{u}_c^{q,k} = \mathbf{u}_c^{q-1} + (\text{particle-fluid coupling terms [18]}) + \frac{\Delta t_p^q}{2} \frac{\mathbf{F}_c^{q,k} + \mathbf{F}_c^{q-1}}{\rho_p V_p} \quad (3.35)$$

$$\mathbf{x}_c^{q,k} = \mathbf{x}_c^{q-1} + \frac{\Delta t_p^q}{2} (\mathbf{u}_c^{q,k} + \mathbf{u}_c^{q-1}) \quad (3.36)$$

$$\boldsymbol{\omega}_c^{q,k} = \boldsymbol{\omega}_c^{q-1} + (\text{particle-fluid coupling terms [18]}) + \frac{\Delta t_p^q}{2} \frac{\mathbf{T}_c^{q,k} + \mathbf{T}_c^{q-1}}{\rho_p I_p} \quad (3.37)$$

$$\text{err}_{iter}^k = \|\mathbf{x}_c^{q,k} - \mathbf{x}_c^{q,k-1}\| \quad (3.38)$$

$$k = k + 1$$

while $\text{err}_{\text{iter}}^k < \text{err}_{\text{iter,max}}$

$\Delta t_p^q = (\alpha_r + \beta_r)\Delta t_p$ varies according to the duration of the Runge-Kutta sub steps and the coefficients can be found in Wesseling [150]: $\alpha_1 = 32/60$, $\beta_1 = 0$, $\alpha_2 = 25/60$, $\beta_2 = -17/60$, $\alpha_3 = 45/60$, $\beta_3 = -25/60$. The lubrication corrections are integrated with the same scheme as the collision force. From this CN2 scheme, we expect second-order accuracy for the linear momentum of the particle and consequently, third-order accuracy for the integration of the particle velocity. We verified the accuracy of the method by reproducing, in simulations of dry collisions, the coefficients of restitution ($e_{n,d}$ and $e_{t,d}$) that are used as an input in the collision model (not shown). For the simulations of the present work 1 iteration sufficed for obtaining a small iterative error: $\text{err}_{\text{iter}}^1 > 10^{-8}\Delta x$.

Unless otherwise stated, the particles are resolved with $D_p/\Delta x = 16$ and a sub-stepping ratio of $r_{\Delta t} = 50$; the collision time set to $T_n = 8\Delta t$ and the time step set a CFL value of $C = 0.5$.

3.5 RESULTS FROM COLLISION SIMULATIONS

3.5.1 BOUNCING MOTION OF A SOLID SPHERE COLLIDING ONTO A PLANAR SURFACE IN A VISCOUS LIQUID

We simulated the bouncing motion of a solid sphere immersed in a viscous liquid and colliding under gravity onto a planar surface. The trajectory of the point of the particle closest to the surface and time evolution of its velocity are compared to the experimental data of Gondret, Lance, and Petit [54]. This experiment is a useful benchmark for confirming that the lubrication corrections and collision model return a realistic bouncing velocity, and that the collision is represented in good approximation as an instantaneous event in the particle motion. Furthermore, there is no need for specifying impact and rebound velocities, which definitions vary significantly in literature [68]. Note that small differences in rebound velocity are amplified after its temporal integration, and therefore more noticeable in the particle trajectory.

The simulations were carried out in a domain corresponding to a closed container with dimensions $L_x/D_p \times L_y/D_p \times L_z/D_p = 12 \times 30 \times 12$. The particle is initially placed at $y/D_p = L_y - 1.5R_p$, centered in $L_x/2$ and $L_z/2$. The motion is driven by a downward-pointing gravitational acceleration of $g = 9.81\text{m/s}^2$. The time step was fixed to the maximum allowed by the stability criterion at the maximum particle velocity (i.e., at impact), multiplied by C to ensure a stable and accurate temporal integration. The physical and computational parameters are listed in table 3.2.

Figure 3.7 presents the results for the trajectory and time evolution of velocity of a steel sphere colliding onto a glass wall immersed in silicon oil RV10, corresponding to Case $St_n = 152$ of table 3.2 with, and without lubrication correction. The model is able

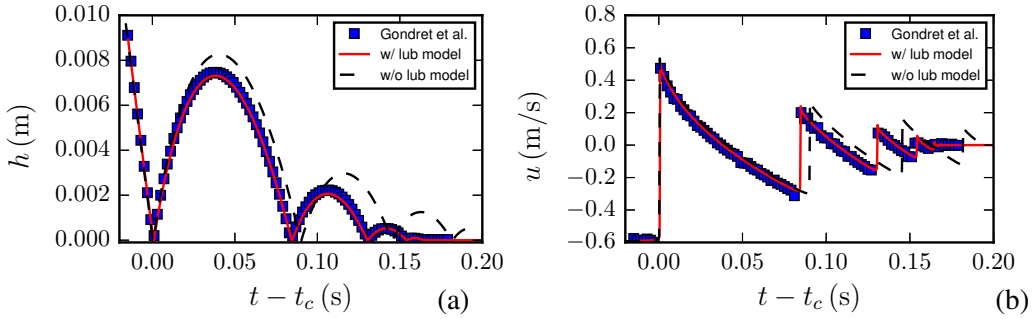


Figure 3.7: Trajectory (a) and time evolution of the particle velocity (b) in the bouncing motion of a steel sphere colliding onto a planar surface in silicon oil RV10.

to accurately reproduce this case. Also, the large discrepancy for the numerical solution in the absence of lubrication model illustrates the importance of including it. Note that at each impact the particle has a lower Stokes number: $St_{n,1st b} = 152$, $St_{n,2nd b} = 81$, $St_{n,3rd b} = 23$ and $St_{n,4th b} = 10$.

Figure 3.8 (a) compares our simulations to the experimental data of Gondret, Lance, and Petit [54] of the first bounce of steel spheres colliding onto planar surfaces in silicon oil at different impact Stokes numbers. In the cases for which L_y was not sufficiently large for the particle to reach its terminal velocity before colliding with the wall, we imposed an initial velocity to the particle to ease the convergence of the velocity to its terminal value. For extreme cases of a highly inertial $St_n = 742$ and highly viscous $St_n = 29$ flow the resolution was increased to $D_p/\Delta x = 32$.

Table 3.2: Properties of the fluids and solid spheres used in the experiment of Gondret, Lance, and Petit [54] and computational parameters of the numerical simulations.

Case	D_p [mm]	ρ_p [kg/m ³]	$e_{n,d}$	μ [cP]	ρ_f [kg/m ³]	$D_p/\Delta x$	C	$r_{\Delta t}$	N
$St_n = 742$	5	7800	0.97	5	920	32	0.5	50	8
$St_n = 152$	3	7800	0.97	10	935	16	0.2	50	8
$St_n = 100$	4	7800	0.97	20	953	16	0.2	50	8
$St_n = 29$	6	7800	0.97	100	965	32	0.5	50	8

As expected and shown in figure 3.8 (b), the deviation from the experimental data for the simulations without lubrication closure is more significant for smaller Stokes numbers due to the increasing importance of viscous effects. Again, the simulations show good agreement with the experimental data for this wide range of Stokes numbers.

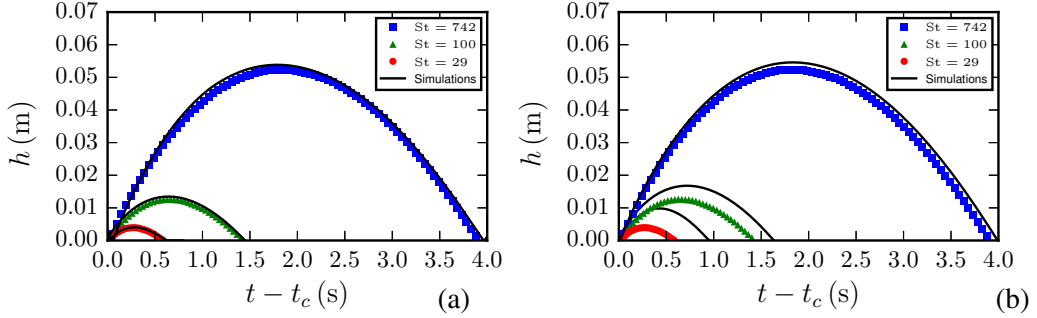


Figure 3.8: Trajectories obtained from simulations of particles colliding onto a planar surface in silicon oil, for different impact Stokes numbers with (a) and without (b) closure for lubrication interactions. Experimental data from Gondret, Lance, and Petit [54].

Sensitivity of the results to the collision time and, time step and sub-stepping

We explore the sensitivity of the model to the computational parameters that govern the collision time and temporal integration of the fluid and particle motion. These parameters are prescribed collision time, T_n , amount of sub-stepping, $r_{\Delta t}$, and time step of the overall numerical algorithm Δt . Let us consider the trajectory of figure 3.7 as the reference case for this sensitivity analysis, with focus on the first bounce (the subsequent will be influenced by how realistically the first is reproduced). We performed a set of simulations with parameters shown in table 3.3. Figure 3.9 (a) presents the outcome of this set

Table 3.3: Computational parameters used for the sensitivity study.

Case	C	$r_{\Delta t}$	N	$\delta_{ij,n}^{max}/\Delta x$ (%)	Notes
REF	0.2	50	8	33.6	Reference case
SA1	0.6	50	5	63.0	Larger Δt , smaller N
SA2	0.2	1	8	33.6	No sub-stepping
SA3	0.2	50	1	4.16	Small N
SA4	0.025	50	8	4.16	Smallest Δt , same T_n as SA3
SA5	0.1	50	16	33.6	Δt between REF and SA5, same T_n as REF
SA6	0.025	50	64	33.6	Same Δt as SA4, same T_n as REF

of simulations. The trajectory corresponding to case SA1 compares well with the one of REF, which shows that a collision which takes 5 Navier-Stokes can still be realistically reproduced.

The trajectories of cases SA2 and REF cannot be distinguished; this shows that sub-stepping is not required to better resolve the collision and lubrication force corrections in this case because the time step of the Navier-Stokes solver is sufficiently small.

In case SA3 the collision time takes exactly one time step of the Navier-Stokes solver, which has the same value that the one of REF. Although the collision force and lubrication corrections are resolved due to the sub-stepping, the trajectory obtained from this simulation differs significantly from the reference case. This is mostly a consequence of an over-estimation of the drag force from the IBM when the surrounding fluid does not adapt itself gradually to the abrupt change in particle velocity due to a collision, as illustrated hereafter.

Decreasing the time step of SA3 while keeping the stiffness fixed (SA4) allows the fluid to adapt itself to the changes in particle velocity. However, the simulation also over-estimates the drag force acting on the particle. We further show with cases SA5 and SA6 that the over-estimation of the drag force is not consequence of an inconsistency problem, because the simulations, for the same particle stiffness, converge monotonically to SA6 with decreasing time step.

The discrepancy of the solution for the stiff particle of case SA4 is caused by a loss of conservation properties of the interpolation kernel used by the IBM when its stencil, for a certain Lagrangian forcing point, overlaps with the one of another particle or with a solid wall [76]. This issue becomes significant for considerably high particle stiffnesses, where more problematic forcing points continue to perform interpolation/spreading operations in an inconsistent manner throughout the entire collision time. Figure 3.9 (b) shows simulations for cases SA3* and SA4* with the same parameters as the ones of SA3 and SA4, but excluding from the forcing scheme Lagrangian forcing points with a distance to the wall smaller than Δx (procedure similar to what is suggested in [76]). Indeed, simulation SA3* still yields an over-estimated drag force, whereas SA4* yields the realistic bouncing trajectory with a difference in the peak of the trajectory of 2.5% from REF.

This illustrates that the realistic bouncing trajectory can only be obtained if the surrounding fluid is allowed to adapt itself to the changes in particle velocity. Hence, we decided to ensure that the fluid phase adapts itself to the changes in particle velocity by avoiding excessively high values of particle stiffness. Note that for the reference case the maximum overlap is already significantly small, about one third of a grid cell.

3.5.2 WET HEAD-ON COLLISIONS

The previous validation gives a fine validation of the approach used to simulate a wet head-on collision. On contrary, the experimental curves of $e_n/e_{n,d} = f(St)$ – benchmark often used to validate these models – depend on the definition of impact and rebound velocities that are used to compute e_n . If, for instance, we define $u_{i,n}$ as the terminal velocity, and $u_{o,u,t,n}$ as the maximum velocity after impact, for the case $St_n = 152$ of table 3.2 we

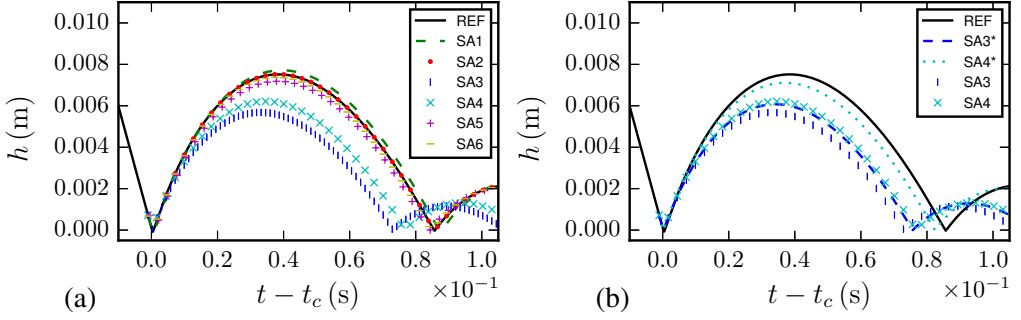


Figure 3.9: Sensitivity analysis to the time step, sub-stepping and stretching of the collision time (a) and outcome of cases SA3 and SA4 when problematic Lagrangian forcing points are excluded from the IBM forcing scheme (b). Computational parameters in table 3.3.

obtain $e_n = 0.85$; considerably different from the experimentally measured value of 0.78. To circumvent this problem one can define impact and rebound velocities which agree with the frame rates used in the measurements [2]. We therefore use the impact velocity and rebound velocities at the instants $t - t_c = \mp f^{-1}$, respectively; where f is a frequency related to the temporal resolution of the experiment.

Particle-wall collisions

We simulated particle-wall collisions in a viscous liquid for several values of St_n and compared the resulting normal coefficients of restitution e_n to the experimental data of Joseph et al. [74].

The computational domain has dimensions of $L_x/D_p \times L_y/D_p \times L_z/D_p = 12 \times 24 \times 12$. Similarly to the previous cases, the particles are placed at a distance $y/D_p = L_y - 1.5R_p$ and their motion driven by gravity. We simulated steel spheres colliding onto a planar surface in silicon oil RV20 (physical parameters are listed in table 3.2). The Stokes number was varied by varying the particle diameters from 1.5 mm to 10 mm. We used a value of $f = 500$ Hz, which complies to the frequency of image acquisition of the experiment. Figure 3.10 shows the results. The numerical simulations agree with the experiments for the entire range of impact Stokes numbers.

Particle-particle collisions

For inter-particle collisions we reproduced the pendulum experiment of Yang and Hunt [151] by colliding a moving projectile particle with a steady target particle. Spheres of the same size and material were centered in a computational box with dimensions $L_x/D_p \times L_y/D_p \times L_z/D_p = 6 \times 12 \times 6$ and separated in the y -direction by a distance of $4 D_p$. Similarly to Simeonov and Calantoni [130], we force an acceleration g to the projectile particle to mimic the release mechanism of the experiment.

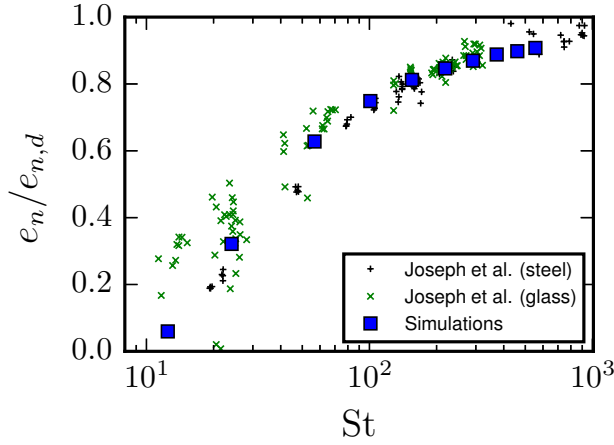


Figure 3.10: Normal, wet coefficients of restitution for particle-wall collisions. The experimental data were normalized with the value $e_{n,d} = 0.97$ measured in the reference.

The physical parameters are comparable to the experiments of head-on collisions of steel spheres in aqueous solutions of glycerol: $e_{n,d} = 0.97$, $\rho_p = 7780 \text{ kg/m}^3$, $D_p = 12.7 \text{ mm}$, $\mu = 45 \text{ cP}$, $\rho_f = 1125 \text{ kg/m}^3$. Yang and Hunt [151] defined the rebound and impact velocities at instants corresponding to a value of $f = 100 \text{ Hz}$.

The *binary* impact Stokes number, defined as $St_{ij,n} \equiv (1/9)\rho_p u_{ij,n} D_p / \mu$ for two equal spheres of the same material, was changed by varying the projectile particle's acceleration from $g/9.81 = 0.02$ to 10 m/s^2 . We used a value of $\varepsilon_\sigma = 10^{-5}$ to resolve the lubrication interaction in the thin gap-width between these smooth particles. This value agrees with the order magnitude of the size of the asperities ($\mathcal{O}(0.1) - \mathcal{O}(0.01) \mu\text{m}$ [151]). These small values together with the fact that the target particle is freely mobile (numerical solution more sensitive to errors when compared to a collision with a wall or a fixed particle) make this benchmark a valuable test for the overall methodology. Resolving the lubrication layer of the interacting particles at such a small scale required a time step dictated by $C = 0.1$ for a resolution of $D_p/\Delta x = 16$, and a sub-stepping ratio of $r_{\Delta t} = 1000$. For values of St_n higher than $\mathcal{O}(100)$, the resolution required to describe the dynamics of the intervening film is higher. Hence, $D_p/\Delta x$ was increased to 32, with a time step dictated by $C = 0.5$.

Figure 3.11 (a) presents the trajectories of the particles' contact points (results of the numerical simulations shifted vertically for clarity). For very small impact Stokes numbers, the momentum transferred to the target particle is not sufficiently high for it to overtake viscous dissipation and travel with increasing relative displacement. Yang and Hunt [151] observed that this is the case for $St_{ij,n} \lesssim 10$, where the particles tend to move as a pair with constant separation distance. This is shown in figure 3.11 (a) for cases $St = 11.8$ (measured experimentally) and $St = 12.7$ obtained from a numerical simulation. The good agreement between the numerical simulation and the experiment gives a finer as-

assessment of the lubrication closure. Furthermore, the simulations with values of binary impact Stokes number considerably larger than 10, $St = 21.5$ and $St = 34.3$ do not show this trend, consistently with the experimental observations.

Finally, figure 3.11 (b) compares the computed effective binary coefficient of restitution from the numerical simulations to the experiments. The necessity of increasing the spatial resolution of the simulation for a binary impact Stokes number of $St = 135$ is also illustrated by showing the outcome of this case with both resolutions. Increasing the resolution becomes more important in this case than in particle-wall interactions due to the requirement of an accurate description of the interacting dynamics of the two particles through short-range hydrodynamic interactions. The agreement with the experimental data is clear.

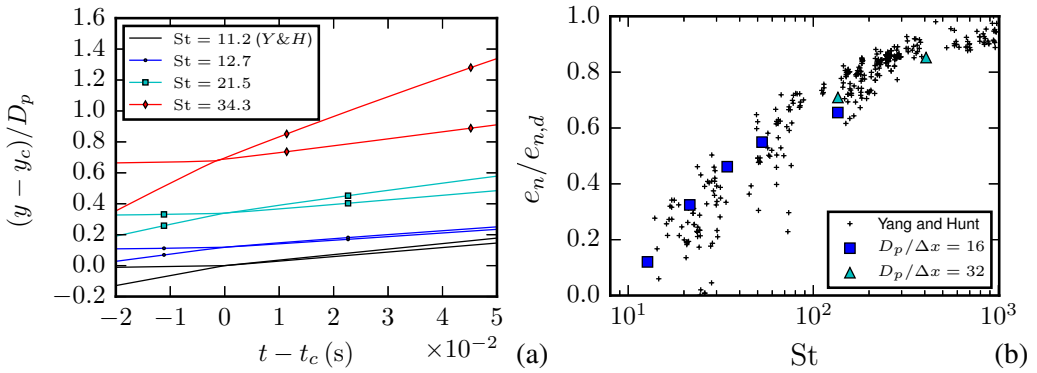


Figure 3.11: Trajectories of the particles' contact points (results of the numerical simulations were shifted vertically for clarity). The solid line was extracted from [151] (a). Wet coefficients of restitution for particle-particle collisions (b). The experimental data were normalized with the value $e_{n,d} = 0.97$ measured in the reference.

We should note that extra computational overhead ($C = 0.1$ for $D_p / \Delta x = 16$) was required for reproducing these results, when compared to particle-wall collisions.

3.5.3 OBLIQUE COLLISIONS

Finally, we validated our model for oblique particle-wall collisions in a dry system and in viscous liquids. We use the experimental data of Joseph and Hunt [73] of oblique particle-wall collisions in air and aqueous solutions of glycerol. The collisional properties parameters of the particles agree with their experiments and are described together with the other physical parameters of the simulations in table 3.4. The computational domain and particle's initial position is the same of the previous simulations of particle-wall collisions. The particle motion is driven by an imposed acceleration with direction $\mathbf{e}_g = -\sin(\phi_{in})\mathbf{e}_y - \cos(\phi_{in})\mathbf{e}_z$, to yield the desired incidence angle. The magnitude of the particle acceleration was set to $g = 10 \times 9.81 \text{ m/s}^2$ to ensure that the glass spheres collide with an impact Stokes number of $\mathcal{O}(1000)$, comparable to the experimentally mea-

sured values. The results for immersed collisions of steel spheres show little sensitivity to the choice of the value of the acceleration due to the small value of the coefficient of sliding friction. For clarity, figure 3.12 presents a visualization of the collision event.

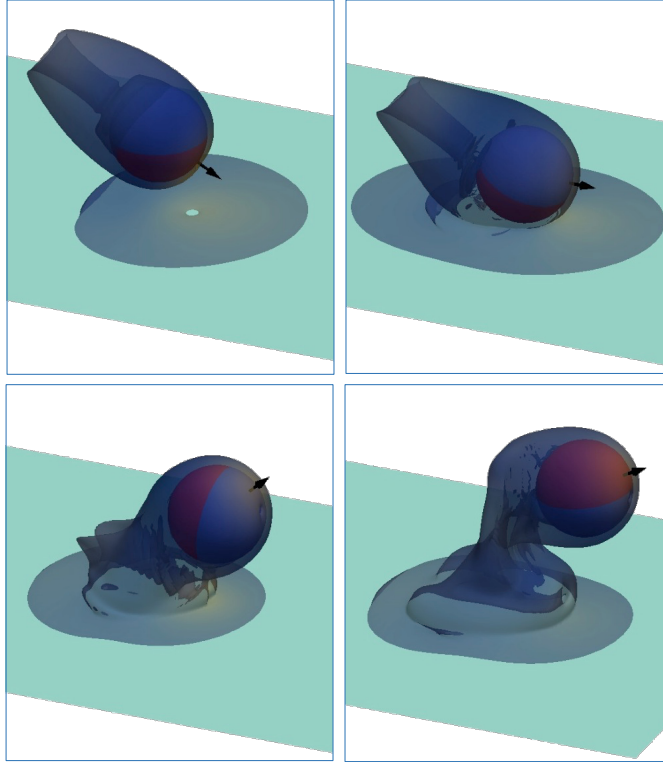


Figure 3.12: Visualization of the approach (top-left), collision (top-right) and rebound (bottom-left and -right) phases for a wet, oblique particle-wall collision. The sphere rotation can be visualized through the color-code. The translucent iso-surface are of constant vorticity magnitude, colored by the fluid pressure (yellow→high, blue→low), and the black arrow denotes the centroid velocity.

Table 3.4: Physical and computational parameters for the simulations of oblique particle-wall collisions.

Material	D_p	$e_{n,d}$	$e_{t,d}$	μ_c	$\mu_{c,wet}$	ρ_p	ρ_f	μ
steel	2.5 mm	0.97	0.34	0.11	0.02	7800 kg/m ³	998 kg/m ³	1 cP
glass	2.5 mm	0.97	0.39	0.10	0.15	2540 kg/m ³	998 kg/m ³	1 cP

Figure 3.13 shows a comparison between the normalized incidence and rebound angles obtained from oblique collisions between steel and glass spheres. The simulations agree well with the experimental data for the entire range of incidence angles. This is an ex-

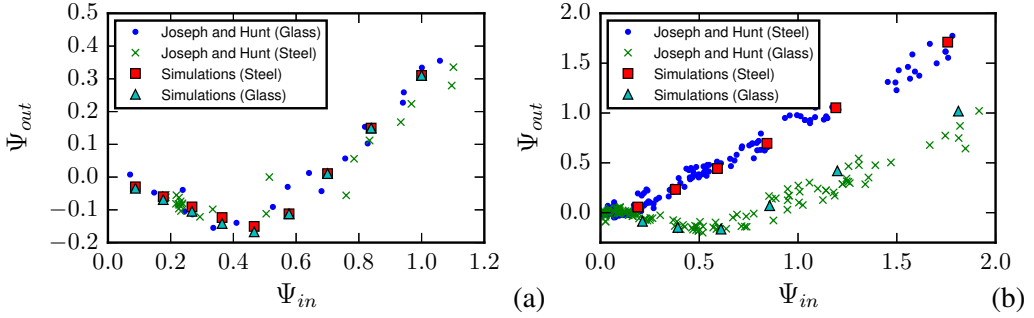


Figure 3.13: Results of for oblique collision simulations in a dry system (a), and in a viscous liquid (b). Experimental data of Joseph and Hunt [73].

pected consequence of the fact that the model uses the macroscopic properties of these collisions as input parameters.

3.6 CONCLUSIONS AND OUTLOOK

We presented and validated a collision model for fully-resolved 4-way coupled simulations of flows laden with finite-size solid particles. There are three types of particle-particle or particle-wall interactions that must be reproduced in such simulations: (1) long-range hydrodynamic interactions; (2) short-range hydrodynamic interactions; and (3) solid-solid contact.

The long-range hydrodynamic interactions are computed by a Navier-Stokes solver where we used an IBM for an efficient representation for the particles. Other approaches that require a closure for small inter-particle/particle-wall distances (e.g., Lagrangian-multiplier or Lattice-Boltzmann methods) could have also been used.

Short-range hydrodynamic interactions are also partly resolved by the IBM. However, the discrete nature of these numerical methods together with the necessity of a computationally efficient implementation typically require a closure model for lubrication interactions. For the cases addressed here, the only lubrication interaction that requires modeling is the squeezing of fluid through the thin gap between two approaching particles or a particle approaching a wall. To achieve this we used a two parameter model: for normalized gap-widths smaller than a value $\varepsilon_{\Delta x}$ we introduce a correction based on asymptotic expansions of analytical solutions of particle-particle/-wall interactions in the Stokes regime. This value is obtained by determining the gap-width below which our numerical method is unable to reproduce the interaction. The second parameter, ε_{σ} , accounts for roughness effects for even smaller gap-widths.

Finally, solid-solid contact is modeled through a linear soft-sphere collision model capable of stretching the collision time, to avoid computational overhead in the calculation of the collision force. The model constants are analytically related to the three input param-

ters of the model described by Walton [148], which are widely reported in the literature. It can be extended to accommodate more complex mechanics such as adhesion or plasticity for the normal force, or static and dynamic friction for the tangential force. However, these features are in general not required in 4-way coupled simulations of flows with finite-size particles at small/moderate solid volume fractions.

We validated our methodology against several benchmark experiments and the results show a good quantitative agreement. The simulations of the bouncing trajectory of a spherical particle colliding onto a planar surface [54] show that the lubrication force corrections, combined with the collision model are sufficient for reproducing a realistic bouncing velocity. Subsequently, we successfully reproduced experimental data for the normal coefficient of restitution as a function of the impact Stokes numbers for head-on particle-wall [74] and particle-particle collisions [151]. Finally, our simulations of oblique particle-wall collisions in dry and wet systems agree quantitatively with the experimental data of Joseph and Hunt [73] for the entire range of incidence angles.

The physical realism and computational efficiency of our method allows for massive fully-resolved simulations of particle-laden flows with 4-way coupling.

4

UNIVERSAL SCALING LAWS FOR DENSE PARTICLE SUSPENSIONS IN TURBULENT WALL-BOUNDED FLOWS

This chapter is adapted from P. Costa et al. “Universal Scaling Laws for Dense Particle Suspensions in Turbulent Wall-Bounded Flows.” In: *Physical Review Letters* 117 (13 Sept. 2016), p. 134501.

Turbulent, wall-bounded suspensions appear widely in environmental and industrial contexts. These suspensions are often dense, i.e. the volume fraction is sufficiently high that particle-particle and particle-fluid interactions strongly influence the macroscopic flow dynamics. In many cases, the suspended particles have a *finite size* – comparable to or larger than the smallest scales in the flow, and particle inertia plays an important role [6].

The flow of suspensions under laminar conditions has been thoroughly studied since Einstein [40] analytically derived an expression for the effective viscosity of a suspension of rigid spheres in the dilute and viscous limit: $\nu^e/\nu = 1 + (5/2)\Phi$, where ν is the kinematic viscosity of the suspending fluid, and Φ the bulk solid volume fraction. In dense cases, the rheology of laminar suspensions is usually characterized by semi-empirical formulas for the effective viscosity [58, 133].

When the Reynolds number (which quantifies the importance of fluid inertial to viscous effects) is sufficiently high, the flow becomes turbulent, exhibiting chaotic and multiscale dynamics. Wall-bounded turbulent flows are characterized by at least one inhomogeneous direction and by the constraint of vanishing velocity at the wall, which makes their analysis even more complicated. For simplicity, we consider the canonical case of a pressure-driven turbulent plane-channel flow laden with neutrally-buoyant particles, defined by the bulk Reynolds number $Re_b = U_b 2h/\nu$, where U_b is the bulk velocity (i.e. averaged over the entire domain) and h the half channel height. In the single-phase limit, the most well-known results from classical turbulence theory are the scaling laws for the mean velocity and the associated drag, or pressure loss. This is obtained by dividing the flow into two regions: the *inner layer*, close to the wall, $y \ll h$, with relevant velocity and length scales u_τ and δ_v , and the *outer layer*, away from the wall, $y \gg \delta_v$, governed by u_τ and h ; here $u_\tau = \sqrt{\tau_w/\rho}$ is the friction velocity, τ_w the wall shear stress, $\delta_v = \nu/u_\tau$ the viscous wall unit and ρ the fluid mass density.

At high-enough friction Reynolds number, $Re_\tau = h/\delta_v = u_\tau h/\nu \gtrsim 100$, corresponding to $Re_b \gtrsim 3000$ [116], an *overlap region* exists, $\delta_v \ll y \ll h$. Here a logarithmic law can be derived for the inner-scaled mean velocity profile, $u/u_\tau = (1/\kappa) \ln(y/\delta_v) + B$, and for the outer-scaled defect law $(U_c - u)/u_\tau = -(1/\kappa) \ln(y/h) + B_d$, with U_c the centerline velocity, $\kappa \approx 0.41$ the so-called von Kármán constant, $B \approx 5.2$ and $B_d \approx 0.2$. These simple scaling laws, derived in 1930 [75], have been confirmed by many numerical and experimental studies (see e.g. [131] for a review). Their importance is unquestionable to predict the overall drag [34] and as basis for many near-wall closure models currently used in computational fluid dynamics [111].

At the very high Reynolds numbers typically encountered in practice, the suspended particles are larger than the smallest turbulent scales ($\sim \delta_v$) and the single-phase approach fails to reproduce the behavior of turbulent channel flows of dense suspensions even when accounting for an effective suspension viscosity [97, 112, 118].

We propose scaling laws for turbulent wall-bounded suspension flows. These are characterized by three parameters: the bulk Reynolds number Re_b , the bulk solid volume frac-

Table 4.1: Physical and computational parameters of the DNS database (consisting of 20 simulations). N_p denotes the number of particles and $\delta_v^{sp h}$ ($\gtrsim \delta_v$) the viscous wall unit for the corresponding single-phase flow at the same Re_b .

Case	h/D_p	$D_p/\delta_v^{sp h}$	Φ (%)	Re_b	N_p
D10	36	9.7	20	12 000	640 000
D20	18	19.4	20	12 000	80 000
D10_2	36	9.7	5	12 000	160 000
FP [112]	9	19.9	0–20	5 600	0–10 000
IL [84]	5	20.7, 32.4	0–30	3 000, 5 000	0–2 580

tion Φ and the particle diameter D_p/h . These laws are capable of predicting the mean velocity and drag from dilute to dense cases, from large to relatively small particles and for a wide range of Reynolds numbers.

We use data from interface-resolved Direct Numerical Simulations (DNS). The DNS solve the Navier-Stokes equations for an incompressible Newtonian fluid in a plane channel with periodic boundary conditions in the streamwise (x) and spanwise (z) directions over lengths of $6h$ and $3h$ respectively, and no-slip and no-penetration at the bottom ($y = 0$) and top ($y = 2h$) walls. The flow solver is extended with an Immersed-Boundary-Method to force the fluid velocity to the local particle velocity at the particle surface [18]. Lubrication closures are used for short-range particle-particle and particle-wall interactions when inter-surface distances are smaller than a grid cell and a soft-sphere collision model for solid-solid contacts [27, 83]. The method has been tested and validated against several benchmark cases [27, 85, 114]. The flow is resolved on a uniform Cartesian grid with size $\Delta = D_p/16$. The computational parameters are presented in table 4.1 where we also report the cases from [84, 112] used here for comparison. The data are complemented with an unladen single-phase reference (SPR) case at the same $Re_b = 12000$ and a continuum limit reference (CLR), i.e. the single-phase flow of a fluid with the effective viscosity ν^e of a suspension with volume fraction $\Phi = 0.2$, corresponding to $Re_b^e = Re_b \nu/\nu^e \approx 6400$ in our case.

Unless otherwise stated, profiles of an observable o pertaining to a certain phase are obtained from the following intrinsic volume average of a 3d flow-field:

$$\langle o \rangle^{f/s}(\mathbf{y}) = \frac{\sum_{ijk} o_{ijk}(\mathbf{x}, \mathbf{y}, z) \phi_{ijk}^{f/s}(\mathbf{x}, \mathbf{y}, z)}{\sum_{ijk} \phi_{ijk}^{f/s}(\mathbf{x}, \mathbf{y}, z)} \quad (4.1)$$

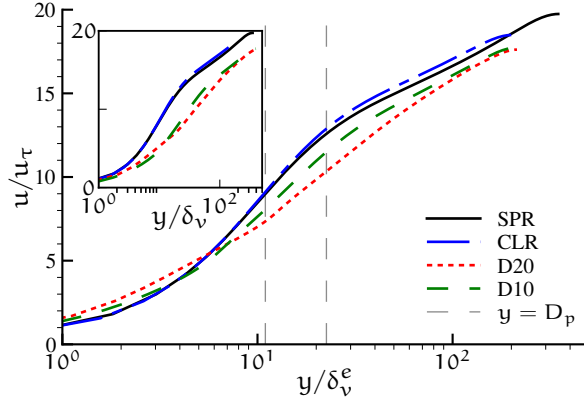


Figure 4.1: Mean streamwise flow velocity, u/u_τ , versus the wall-normal distance in inner scaling y/δ_v^e . Vertical dashed lines depict a wall-normal distance of 1 particle diameter ($y = D_p$) for cases D10 (closest to $y = 0$) and D20, see table 4.1. Maximum statistical error within 95% confidence interval is $\pm 0.9\%$. The inset shows the same velocity profile but with the wall-normal distance scaled with δ_v .

where $\phi(x, y, z)$ is a phase-indicator function ($\phi_{ijk}^f + \phi_{ijk}^s = 1$). For simplicity, we will drop in the profiles the $\langle \rangle$ brackets. Profiles pertaining to the combined phase are obtained in a similar fashion,

$$\langle o \rangle^c(y) = \frac{\sum_{ik} \left(o_{ijk}(x, y, z) \phi_{ijk}^f(x, y, z) + o_{ijk}(x, y, z) \phi_{ijk}^s(x, y, z) \right)}{\sum_{ik} \left(\phi_{ijk}^f(x, y, z) + \phi_{ijk}^s(x, y, z) \right)}. \quad (4.2)$$

Figure 4.1 shows the mean velocity profile for $D_p/\delta_v \approx 10$ (D10) and 20 (D20), compared to the continuum limit reference (CLR). The comparison between the single-phase and the two-phase flows requires a proper definition of the viscous wall unit in terms of ν^e , here $\delta_v^e = \nu^e/u_\tau$. Despite the improvement with respect to the use of the classical definition of $\delta_v = \nu/u_\tau$ (see the inset of figure 4.1), the figure reveals that the particle-laden flows show a clear deviation from the classical logarithmic law. The differences with the continuum limit are higher for larger particles, and so is the measured increase in drag. The abrupt change of the slope of the profile at a wall-normal distance of $y \sim D_p$ suggests that the deviation from the continuum limit is caused by a change in the near-wall dynamics. Studies of laminar wall-bounded flows laden with neutrally-buoyant spheres report a structured arrangement of particles near the wall [59, 114, 152]. This layering is attributed to the planar symmetry imposed by the wall and to stabilizing particle-particle and particle-wall interactions. Though more pronounced under laminar conditions, this phenomenon is also present in turbulent suspensions [84, 112]. Figure 4.2a presents the mean local number density n , normalized with the corresponding bulk value N , for cases D10 and D20 (see table 4.1). The particle layer is evident from the local minimum at a

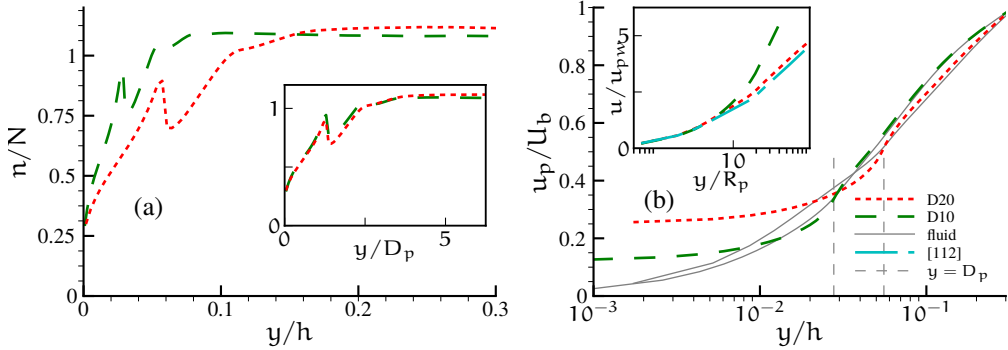


Figure 4.2: (a) Mean particle number density n divided by its bulk value N versus y/h in the main panel and y/D_p in the inset (Maximum statistical error within 95% confidence interval is $\pm 0.8\%$). (b) Mean streamwise particle and fluid velocity. The inset shows the fluid velocity, normalized with $u_{p,w}$ (definition in the text) versus y/R_p . The data from [112] pertain to the case of $\Phi = 20\%$. Vertical dashed lines depict a wall-normal distance of 1 particle diameter ($y = D_p$) for cases D10 (closest to $y = 0$) and D20, see table 4.1.

distance of one particle diameter from the wall, as shown in the inset where the horizontal axis is scaled with D_p .

The apparent mean particle-to-fluid slip velocity is highest close to the wall and becomes negligible at wall-normal distances $y \gtrsim D_p$, see figure 4.2b where we report the wall-normal profiles of the mean particle and fluid velocity for two of the cases considered. Away from the wall, the complex interaction between the turbulent fluid motion and the particles still result in approximately the same average value of streamwise velocity, as if the two phases behave as a continuum. The layer of particles near the wall shows an almost constant slip with respect to the fluid. This large slip indicates that continuum models based on an effective viscosity are bound to fail.

The inset of figure 4.2b reports the fluid velocity divided by the particle-to-fluid slip velocity at the wall, $u_{p,w}$, versus the wall-normal distance in units of particle radius R_p . For the same volume fraction of 20%, results from different numerical simulations with different Reynolds numbers and particle sizes collapse for wall-normal distances smaller than a particle radius. It appears that, in dense suspensions, a particle-wall layer exists that prevents a direct interaction between the turbulent suspension flow in the core and the solid wall underneath the particle-wall layer. This serves as starting point for the scaling arguments presented hereafter.

The former considerations motivate a modeling approach based on the separation between the dynamics of the particle-wall layer and of the turbulent flow region. We will denote the latter as the homogeneous suspension region (HSR), meaning a well mixed suspension. Let us therefore define the thickness of the particle-wall layer by the length scale $\delta_{p,w}$. The previous discussion showed that $\delta_{p,w}$ scales with D_p at fixed volume fraction.

In addition, δ_{pw} should vanish in the single-phase limit, i.e. when $\Phi \rightarrow 0$. We therefore assume δ_{pw} (i) to be proportional to the *solidity* of the bulk suspension, measured as the ratio between particle size and mean particle separation distance, and (ii) to scale with the particle size. These hypotheses give the result above $\delta_{pw} = C (\Phi/\Phi_{max})^{1/3} D_p$, where the constant is set to $C = 1.5$ ¹ for all the cases addressed here and $\Phi_{max} = 0.6$. Note that displacing the origin of the turbulent region has been successfully adopted in turbulent flows over rough walls [69], but was not applied before to the case of turbulent suspensions.

In the same spirit, we further assume that the total stress $\tau = \rho u_\tau^2 (1 - y/h)$ acting across the channel is due to two distinct mechanisms. In the HSR, the increment in stress due to the particles is assumed to be well modeled by an effective suspension viscosity; in the particle-wall layer, instead, the stress increases due to the large apparent slip velocity near the wall. This is the main finite-size effect present in the flow. The stress in the HSR ($y > \delta_{pw}$) corresponds therefore to that of a single-phase turbulent flow of a Newtonian fluid with viscosity ν^e , in a channel with a wall origin at $y = \delta_{pw}$ and half-height $h - \delta_{pw}$. The flow in this region experiences an apparent stress $\rho u_\tau^{*2} \leq \rho u_\tau^2$. In the particle-wall layer ($y < \delta_{pw}$) the stress increases linearly when approaching the wall from ρu_τ^{*2} to $\rho u_\tau^2 = \rho u_\tau^{*2} + \Delta\tau_{pw}$. Hence, the total stress, linearly varying across the channel [112], is split into two contributions:

$$\tau = (\rho u_\tau^{*2} + \Delta\tau_{pw}(1 - y/\delta_{pw})) \mathcal{H}(\delta_{pw} - y) + (\rho u_\tau^2(h - y)/(h - \delta_{pw})) \mathcal{H}(y - \delta_{pw}); \tag{4.3}$$

where \mathcal{H} is the Heaviside step function with the half-maximum convention. Evaluating eq. (4.3) at $y = \delta_{pw}$ yields the friction velocity in this region $u_\tau^* = u_\tau(1 - \delta_{pw}/h)^{1/2}$. Given u_τ^* , ν^e and δ_{pw} we obtain the following laws for the inner- ($u/u_\tau^* = F[(y - \delta_{pw})u_\tau^*/\nu^e]$) and outer-scaling ($(U_c - u)/u_\tau^* = G[(y - \delta_{pw})/(h - \delta_{pw})]$) of the mean velocity in the overlap region of the HSR:

$$\frac{u}{u_\tau^*} = \frac{1}{\kappa} \ln \left(\frac{y - \delta_{pw}}{\delta_v^{e*}} \right) + B, \tag{4.4}$$

$$\frac{U_c - u}{u_\tau^*} = -\frac{1}{\kappa} \ln \left(\frac{y - \delta_{pw}}{h - \delta_{pw}} \right) + B_d, \tag{4.5}$$

with $u_\tau^* = u_\tau(1 - \delta_{pw}/h)^{1/2}$, $\delta_v^{e*} = \nu^e/u_\tau^*$; κ , B and B_d retain the values of single-phase flow; here $\nu^e/\nu = (1 + (5/4)\Phi/(1 - \Phi/\Phi_{max}))^2$ [133]. Figure 4.3 reports the mean velocity profiles from the present simulations and the cases from [112]. The figure shows a collapse of the profiles in the logarithmic region, except for case FP [112] with $\Phi = 20\%$ (see table 4.1). This is expected from our model, because it is the only case for which the friction Reynolds number based on the scaling parameters of the HSR $Re_\tau^{hsr} =$

¹ Value obtained by fitting the agreement of the drag to the simulation results.

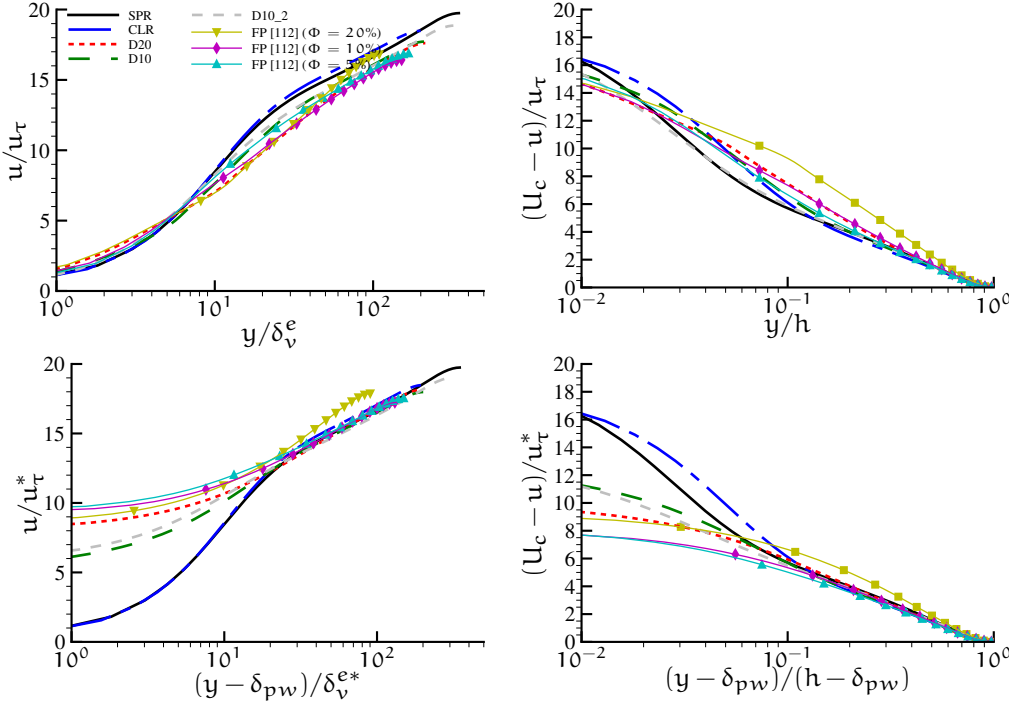


Figure 4.3: Profiles of mean streamwise fluid velocity u/u_τ^* versus the wall-normal coordinate $(y - \delta_{pw})/\delta_v^{e*}$, and defect law, $(U_c - u)/u_\tau^*$, versus the distance to the wall in outer units $(y - \delta_{pw})/(h - \delta_{pw})$ (definitions in the text). The top panels correspond to the unscaled profiles, accounting only for an effective suspension viscosity, i.e. $\delta_{pw} = 0$. Maximum statistical error is the same as in figure 4.1.

$(h - \delta_{pw})/\delta_v^{e*} < 100$. This implies that there is not a sufficient separation of the inner and outer scales for the overlap region to exist [116], which is a necessary condition for the logarithmic scaling of the velocity profile. The defect law is shown in outer scaling in the inset of figure 4.3, where scaling in the logarithmic region can be clearly depicted. Also for this quantity the improvement with respect to the case where the particle-wall layer is not considered ($\delta_{pw} = 0$) is significant (not shown). In addition, figure 4.4 shows the compensated profile $\frac{1}{\kappa^*} = (y - \delta_{pw}) \frac{1}{u_\tau^*} \frac{du}{dy}$ for the present DNS. All the profiles have a better agreement with the single-phase cases when corrected for the apparent wall origin δ_{pw} . Notice that the local minimum of the profiles for the cases laden with small particles (D10 and D10_2) occurs at the same wall-normal distance as in the single-phase cases. Finally, the proposed scaling laws are used to derive the following drag law (i.e. the mean wall shear stress $\tau_w = \rho u_\tau^2$), expressed in terms of the friction Reynolds number:

$$\text{Re}_\tau = \frac{\text{Re}_b}{2\xi_{pw}^{1/2}} \left(\frac{1}{\kappa} \left[\ln \left(\text{Re}_\tau \chi^e \xi_{pw}^{3/2} \right) - 1 \right] + B + B_d \right)^{-1}, \quad (4.6)$$

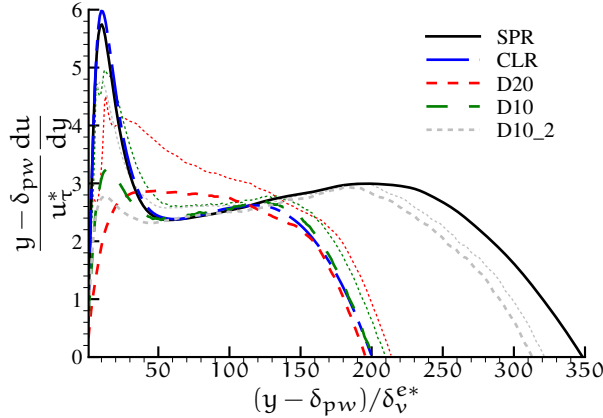


Figure 4.4: Profile of $\frac{1}{\kappa^*} = (y - \delta_{pw}) \frac{1}{u_*^*} \frac{du}{dy}$. The thinnest dotted lines correspond to the *uncorrected* case where $\delta_{pw} = 0$ and the solid lines to the corrected case with $\delta_{pw} = 1.5(\Phi/\Phi_{max})^{1/3} D_p$.

where $\xi_{pw} = (1 - \delta_{pw}/h)$ and $\chi^e = \nu/\nu^e$. Eq. (5.3) is derived in the same way as well-known laws from single-phase flow are derived [34]: by integrating the defect law (eq. (5.2)) over the entire HSR to relate the bulk and centerline velocities, and combining eq. (5.1) and eq. (5.2) to relate the friction and bulk velocities. Note that eq. (5.3) reduces to the well-known relation for single-phase flow when $\Phi \rightarrow 0$. This derivation, together with an alternative, simpler equation to predict the overall drag, are given at the end of this chapter. Figure 4.5 compares the relative difference between the predicted values of Re_τ and the values obtained from the DNS, Re_τ^{dns} . The filled symbols correspond to predictions where only the effective viscosity is taken into account, i.e. $\delta_{pw} = 0$, and the open symbols to predictions where both effects are accounted for. The estimates of the drag improve for the three datasets and the difference with the DNS values is less than 4%. This supports the necessity of accounting for finite-size effects and further validates the proposed scaling. We remark that the implicit formulation of the drag law given by eq. (5.3) can be replaced by a simple explicit power law of Re_τ as a function of Re_b , less sensitive to insufficient inner-to-outer scale separation, which yields similar (and consistently, slightly more accurate at low Reynolds numbers) predictions for the drag; see the last section of this chapter material.

The solution of eq. (5.3), normalized with the corresponding friction Reynolds number for single-phase flow $Re_\tau^{sph} = Re_\tau|_{\Phi=0}$, can be examined to draw general conclusions on the suspension behavior. For constant volume fraction and Reynolds number we conclude that a finite particle size causes a significant increase in drag with respect to the continuum limit due to the formation of a particle-wall layer. As expected, the drag increases monotonically with the particle size (corresponding to an increase of δ_{pw}) and volume fraction (increasing δ_{pw} and ν^e).

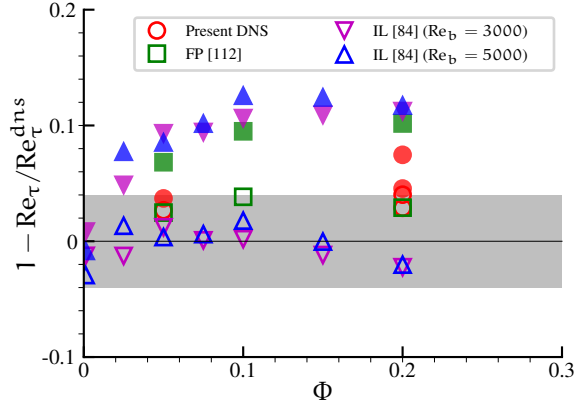


Figure 4.5: Relative difference to the theoretical prediction of friction Reynolds number (the shaded area corresponds to a difference of $\pm 4\%$). Filled symbols correspond to values that were not corrected for the presence of the particle-wall layer (i.e. $\delta_{pw} = 0$). The maximum statistical error in the computation of the overall drag (with 95% confidence interval) from the DNS is below 1%. The corresponding (shifted) error bar is also shown on the left-hand side of the plot legend.

To conclude, we presented scaling laws for the mean velocity and the velocity defect in turbulent channel flow of neutrally-buoyant finite-size spherical particles, which also enables us to accurately predict the total suspension drag. The model quantifies the main finite-size effect present in the flow – a particle-wall layer which always causes an increase in drag, by separating the dynamics of the flow in this layer and the homogeneous suspension region in the core. Exploiting conservation of momentum, this effect can be reduced to an apparent wall location $y = \delta_{pw}$ above which the flow is reasonably well represented by a Newtonian fluid with an effective suspension viscosity ν^e . We validated our predictions for a reasonably wide range of the governing parameters.

DERIVATION OF DRAG LAW

In the single-phase case, one can relate the bulk velocity to the friction velocity from the logarithmic scaling laws for mean velocity and velocity defect. A detailed derivation, together with the inherent assumptions can be found e.g. in [116].

We aim at relating Re_τ to the parameters governing the flow in the overlap region: Re_b , Φ and D_p/h . As for single-phase turbulent channel flow we assume for the homogeneous suspension region that the bulk velocity is well approximated by integrating the velocity defect over the height of the homogeneous suspension region (HSR). This approximation is valid as long as (i) the Reynolds number is sufficiently high that the inner layer of the HSR does not contribute significantly to the bulk velocity and (ii) the virtual wall origin

δ_{pw} is sufficiently small that the flow inside the particle-wall layer contributes little to the bulk velocity. Thus,

$$U_b \approx \frac{1}{h - \delta_{pw}} \left(\int_{\delta_{pw}}^h u \, dy \right). \quad (4.7)$$

The bulk velocity is then estimated by integrating the defect law from δ_{pw} to h (consistency requires that the constant B_d , typically small, is set to 0),

$$U_b \approx \left(U_c - \frac{u_\tau^*}{\kappa} \right). \quad (4.8)$$

Next, the two expressions for the log law, in inner and outer variables respectively, are combined to relate the mean centerline velocity U_c to the apparent wall friction velocity u_τ^* , yielding:

$$\frac{U_c}{u_\tau^*} = \frac{1}{\kappa} \ln \left(\frac{h - \delta_{pw}}{\delta_v^{e*}} \right) + B + B_d \quad (4.9)$$

Combining eq. (4.8) and eq. (4.9) we obtain the following expression for U_b/u_τ^* :

$$\frac{U_b}{u_\tau^*} = \frac{1}{\kappa} \left[\ln \left(\frac{h - \delta_{pw}}{\delta_v^{e*}} \right) - 1 \right] + B + B_d \quad (4.10)$$

Substituting $u_\tau^* = u_\tau (1 - \delta_{pw}/h)^{1/2}$, and $\delta_v^{e*} = \nu_e/u_\tau^*$ in eq. (4.10) we get

$$\frac{U_b}{u_\tau} = \left(\frac{1}{\kappa} \left[\ln \left(\text{Re}_\tau \frac{\nu}{\nu_e} \left(1 - \frac{\delta_{pw}}{h} \right)^{3/2} \right) - 1 \right] + B + B_d \right) \left(1 - \frac{\delta_{pw}}{h} \right)^{1/2} \quad (4.11)$$

After re-arranging, we finally obtain

$$\text{Re}_\tau = \frac{\text{Re}_b}{2\xi_{pw}^{1/2}} \left(\frac{1}{\kappa} \left[\ln \left(\text{Re}_\tau \chi^e \xi_{pw}^{3/2} \right) - 1 \right] + B + B_d \right)^{-1}, \quad (4.12)$$

where $\xi_{pw} = (1 - \delta_{pw}/h)$ and $\chi^e = \nu/\nu_e$. Eq. (4.12) can be solved numerically by substituting $\delta_{pw} = C(\Phi/\Phi_{max})^{1/3} D_p$ and $\nu_e = (1 + (5/4)\Phi/(1 - \Phi/\Phi_{max}))^2 \nu$. The constant $C = O(1)$ was set to 1.5 for all the cases presented in this study, and Φ_{max} to 0.6.

AN ALTERNATIVE CORRELATION FOR THE OVERALL DRAG

Figure 4.6 displays the same quantity as figure 4.5. The difference now is that the estimate is based on an empirical correlation valid for single-phase flow ($\text{Re}_\tau^{sph} \approx 0.09 \text{Re}_b^{0.88}$ [116]),

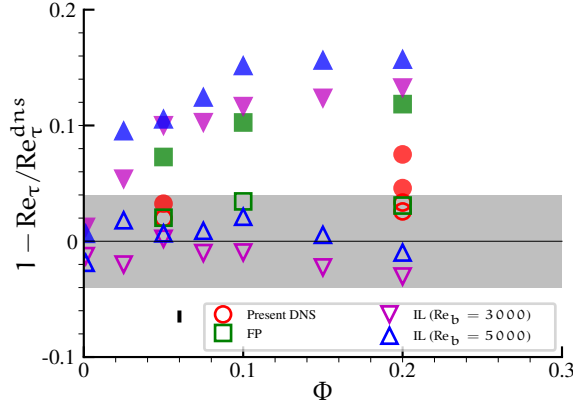


Figure 4.6: Relative difference to the theoretical prediction of friction Reynolds number (the shaded area corresponds to a difference of $\pm 4\%$) when an empirical correlation is used: $\text{Re}_\tau = 0.09(\text{Re}_b \chi^e \xi_{pw})^{0.88} / (\xi^{3/2} \chi^e)$. Filled symbols correspond to values that were not corrected for the presence of the particle-wall layer (i.e. $\delta_{pw} = 0$). The maximum statistical error in the computation of the overall drag (with 95% confidence interval) from the DNS is below 1%. The corresponding (shifted) error bar is also shown on the left-hand side of the plot legend.

which is extended to the case of a turbulent suspension. For the homogeneous suspension region we obtain:

$$\text{Re}_\tau^{\text{hsr}} = \frac{u_\tau^*(h - \delta_{pw})}{\nu^e} \approx 0.09 \left(\frac{U_b(h - \delta_{pw})}{\nu^e} \right)^{0.88}, \quad (4.13)$$

and from this we derive the following explicit, power-law expression for Re_τ :

$$\text{Re}_\tau = \frac{0.09 (\text{Re}_b \chi^e \xi_{pw})^{0.88}}{\xi_{pw}^{3/2} \chi^e}; \quad (4.14)$$

where $\xi_{pw} = (1 - \delta_{pw}/h)$ and $\chi^e = \nu/\nu^e$. Figure 4.6 shows that the empirical correlation given by eq. (5.4) yields similar predictions for the drag as eq. (4.12). In general, the predictions from the empirical correlation are slightly more accurate (i.e., the error is smaller), in particular for the data at the lowest values of Re^{hsr} (see upward- and downward-pointing triangles).

It is interesting to note that the explicit nature of eq. (5.4) enables us to estimate the relative importance of the finite-size effect (ξ_{pw}) and effective suspension viscosity (χ^e) at the given flow rate (quantified by Re_b):

$$\text{Re}_\tau \propto \frac{\text{Re}_b^{0.88}}{\xi_{pw}^{0.62} \chi^e 0.12}. \quad (4.15)$$

The large exponent of ξ_{pw} , 0.62, confirms that the finite-size effect plays an important role. At fixed particle size, however, the effective viscosity still plays a major role in these

dense flows, as $1/\chi^e \sim 1 + \Phi + O(\Phi^2)$ increases faster with Φ than $1/\xi_{pw} \sim 1 + \Phi^{1/3} + O(\Phi^{2/3})$.

5

FINITE-SIZE EFFECTS IN TURBULENT SUSPENSION TRANSPORT

This chapter is adapted from P. Costa et al. "Finite size effects in dense turbulent wall-bounded transport of neutrally-buoyant spheres." In: *Journal of Fluid Mechanics (under review)* (2017).

5.1 INTRODUCTION

Throughout the years many studies on laminar shear flows laden with non-Brownian solid particles have been reported. In these cases one can take advantage of the linearity of the Stokes equations and achieve a rich variety of results by e.g. superposition of several canonical solutions. An iconic example is the effective viscosity of a suspension of non-Brownian spheres in the dilute and Stokes limit, derived by Einstein [39] to be $\mu_e/\mu = 1 + (5/2)\Phi$, with μ being the viscosity of the suspending fluid, and Φ the bulk solid volume fraction. Many studies followed throughout the years (see e.g. [19, 58, 133] for more rheological studies).

Most of the experimental works on particle suspensions have been limited to integral quantities, in particular the total wall shear. Often, the torque measured in a Taylor-Couette system required to keep a certain shear rate is used to measure effective viscosities and obtaining insight in the suspension rheology (see e.g. [5, 67, 133]). Although many important results have been extracted from this approach, more detailed measurements of important features, such as the microscale organisation or the particle dynamics are challenging to obtain.

Lack of direct measurements at the microscale level gave room for important analytical studies that relate the bulk suspension behavior to the particle dynamics. A well-known example is the work of Leighton and Acrivos [88], who introduced the concept of shear-induced migration due to irreversible inter-particle interactions, to explain the migration of particles to the fluid reservoir in their Taylor-Couette experiments.

Great progress on the understanding of the flow dynamics at the particle scale has been achieved through numerical simulations. Here one can measure directly the suspension micro-structure and particle dynamics. In particular for flows in the Stokes regime, one can use very accurate and relatively inexpensive particle-based methods such as Stokesian dynamics [14] to understand in detail the bulk suspension behavior from a microscale perspective. Recent advances in experimental techniques made also possible direct measurements of a suspension micro-structure (see e.g. [13]).

When inertial effects become significant, the governing equations for the fluid phase are non-linear and therefore analytical descriptions, numerical simulations and even experiments become more challenging. Moreover, if the Reynolds number is sufficiently high, the flow becomes turbulent, exhibiting chaotic and multi-scale dynamics. This makes the understanding of these flows even more difficult.

Despite this, significant progress has been made with regard to wall-bounded particle-laden flows in the turbulent regime, in the point-particle limit. Several studies have been carried out analytically (e.g. [100, 120]), numerically [38, 125, 132] and experimentally [45]. As a result, a deep understanding of the mechanisms e.g. leading to preferential accumulation of particles smaller than the Kolmogorov scale depending on their inertia and the local flow characteristics has been achieved. Similar maturity for the cases where

the feedback of particles in the flow or finite size effects are relevant is still far from being accomplished.

The previously mentioned challenges and limitations of experimental and theoretical approaches makes the use of advanced numerical tools a necessity for obtaining detailed information; despite the well-known limitations in terms of Reynolds numbers that can be reached in simulations [118]. Lately, several groups have been successfully using numerical algorithms for interface-resolved direct numerical simulations (DNS) of different turbulent flows laden with finite size particles: examples are suspensions in isotropic turbulence [93, 137], vertical channel flow [143], sedimentation [24, 47], bed load transport [78, 145], channel transport of mono-dispersed particles [149, 153], and recently of poly-disperse [86] and non-spherical particles [4]. Likewise, we use such simulations to study turbulent channel transport of neutrally-buoyant finite size spheres.

Suspensions of neutrally-buoyant particles close to the onset of turbulence have also been explored both experimentally [97] and numerically [92]. A common feature of the results from these studies is the fact that solely an increase in effective viscosity of the suspension does not explain the observed phenomenology, in particular for large particles.

In particle suspension flows a new mechanism for momentum transport emerges in the form of a *particle stress* [11]. It therefore makes sense to follow the idea of Lashgari et al. [84], who distinguished three different flow regimes, depending on the relative importance of viscous, Reynolds and particle stresses to the total stress of the suspension: a laminar (low Reynolds number and low volume fraction), turbulent (high Reynolds number and moderate to low volume fractions) and inertial shear-thickening (high volume fractions), the latest regime being characterized by a significant increase in wall shear that is not accompanied by an increase in the magnitude of the turbulent stresses.

Recently, Picano, Breugem, and Brandt [112] presented detailed direct numerical simulations of turbulent channel flow laden with neutrally-buoyant finite size spheres. They showed that, for fixed Reynolds number and particle size, particle stresses at a volume fraction of about 20% are responsible for a non-monotonic behavior of the near-wall peak in Reynolds shear stresses as a function of the volume fraction. The associated turbulence attenuation is higher than what predicted only by accounting for an effective viscosity. The decrease in the magnitude of the Reynolds stresses is accompanied by a more dominant increase in particle-induced stresses, which ultimately results in an overall drag increase.

This observation is consistent with flow regime map of Lashgari et al. [84] and supported by the recent work of Costa et al. [28]. The authors built up upon the work in [112] by extending the data set to higher Reynolds number and smaller particle sizes. They showed that a layer of near-wall particles causes the suspension to deviate from the continuum limit, where its dynamics is well represented by an effective suspension viscosity. Away from this layer, the suspension mean flow is shown to be well described by an effective suspension viscosity. Based on this idea Costa et al. [28] successfully derived the scaling laws for the mean flow in the overlap region, and accurate correlations capable of predicting the overall drag that the suspension experiences as a function of the three

governing parameters: Re_b , Φ , and D_p/h , respectively the bulk Reynolds number, solid volume fraction and particle size ratio.

Here we investigate how finite size effects change the flow and particle dynamics near the wall, and up to which point it is actually important to consider them in the bulk of the channel. We related the observed mesoscale behavior to the local microscale dynamics. This allowed us to present a clear picture of the sources of finite size effects in a dense turbulent suspension, needed for future modeling efforts.

5.2 COMPUTATIONAL SETUP

The flow dynamics is governed by three parameters: the bulk Reynolds number $Re_b \equiv U_b(2h)/\nu$, the particle size ratio D_p/h , and the bulk volume fraction of solid particles $\Phi = N_p V_p/V_t$ (note that the particles are neutrally-buoyant), where U_b is the flow bulk velocity (forced to be constant in the numerical algorithm), h the half channel height, D_p the particle diameter, N_p the total number of particles, and V_p and V_t the volumes of a particle and of the computational domain. In the present work the bulk volume fraction of solid particles is fixed to $\Phi = 20\%$, and the Reynolds number to $Re_b = 12\,000$, in order to ensure sufficient inner-to-outer scale separation [28]. Two different particle sizes are considered as reported in table 5.1, together with other relevant physical and computational parameters.

The simulations are performed in a domain with dimensions $L_x/h \times L_y/h \times L_z/h = 6 \times 2 \times 3$, using a grid spacing dictated by the number of grid cells required to resolve the flow conforming the spheres: $\Delta x/D_p = 1/16$. Particles are considered to be frictionless, with a dry coefficient of restitution $e_{n,dry} = 0.97$. The interface-resolved simulations presented here are complemented with two single-phase reference cases: the unladen case at the same bulk Reynolds number, denoted SPR (single-phase reference), and the continuum limit where the flow dynamics can be reproduced by a single-phase fluid with the effective viscosity of the suspension at $\Phi = 20\%$, denoted as CLR (continuum limit reference). This simulation corresponds thus to a single-phase flow with bulk Reynolds number $Re_b \nu/\nu^e \approx 6\,400$ and effective viscosity $\nu^e = \nu(1 + \Phi/(1 - \Phi/\Phi_{max}))^2$ obtained from Eilers fit [133], with $\Phi_{max} = 0.6$. We note that data from these simulations have been also presented in the previous chapter.

Due to the large size of these simulations, all spatial averages were computed during run time and averaged in time a posteriori, with samples obtained from a time interval of about $1500h/U_b$, spaced by $7h/U_b$. A total of about 7 million core hours in the super-computer CURIE (thin nodes; B510 bullx) at CEA, France, and Beskow (Cray XC40) at KTH, Sweden were used.

Case	Re_b	h/D_p	D_p/δ_v^{sph}	Φ (%)	$N_x \times N_y \times N_z$	N_p
D10	12 000	36	9.7	20	$3456 \times 1152 \times 1728$	640 000
D20	12 000	18	19.4	20	$1728 \times 576 \times 864$	80 000
SPR	12 000	–	–	–	$1728 \times 576 \times 864$	0
CLR	6 400	–	–	–	$1152 \times 384 \times 576$	0

Table 5.1: Physical and computational parameters of the DNS data sets. δ_v^{sph} ($\gtrsim \delta_v$) denotes the viscous wall unit for the corresponding single-phase flow at the same Re_b , estimated from $Re_\tau^{sph} = 0.09Re_b^{0.88}$ [116]. N_p denotes the number of particles, $N_{x/y/z}$ denotes the number of grid points in the $x/y/z$ directions.

5.3 RESULTS

NEAR-WALL DYNAMICS – THE MAIN CAUSE OF FINITE SIZE EFFECTS

We will here refer to *finite-size effects* as the causes for the meso or macroscale-averaged flow statistics to be different from those obtained from the continuum limit approximation in which the suspension is modeled as a Newtonian fluid with an effective viscosity due to the presence of the particles.

Costa et al. [28] showed that a layer of particles, flowing near the wall with significant (apparent) slip velocity, is responsible for an additional increase in drag which cannot be modeled by an effective suspension viscosity. By accounting for this effect, the authors were able to scale the profiles of mean velocity and velocity defect ($U_c - u$, where U_c is the mean centerline velocity) for a wide range of combinations of Re_b , Φ and D_p/h . The theory in Costa et al. [28] assumes that the domain can be split into two regions, bounded at a wall-normal distance $y = \delta_{pw}$: a region away from the wall, denoted homogeneous suspension region (HSR) ($y > \delta_{pw}$) where the mean flow of the suspension is well represented by the continuum limit of a Newtonian fluid with effective viscosity ν^e , and a region close to the wall denoted particle-wall layer (PWL) ($y < \delta_{pw}$) where the difference between the mean flow of the two phases, at the mesoscale level, makes this assumption invalid. By exploiting the stress budget, the authors could derive scaling laws for the mean velocity and velocity defect in the HSR, provided that, like in a single-phase turbulent channel, inner-to-outer scale separation is satisfied. In other words, the friction Reynolds number based on the scaling parameters of the homogeneous suspension region needs to be sufficiently high. These are a channel height corrected for a virtual-wall origin, $h - \delta_{pw}$, the friction velocity taken from the profile of the total stresses at $y = \delta_{pw}$, $u_\tau^* =$

Case	Re_τ	Re_τ^e	Re_τ^{e*}
SPR (unladen)	350	350	350
D10	395	209	203
D20	406	215	203
CLR	201	201	201

Table 5.2: Friction Reynolds numbers for the different cases studied. $Re_\tau = u_\tau h/\nu$ is the typical friction Reynolds number defined from the wall friction velocity and fluid viscosity, $Re_\tau^e = Re_\tau \nu/\nu^e$ is instead defined from the suspension effective viscosity and $Re_\tau^{e*} = u_\tau(1 - \delta_{pw}/h)^{1/2}(h - \delta_{pw})/\nu^e = Re_\tau^e(1 - \delta_{pw}/h)^{3/2}$ is defined from a wall friction velocity and channel height corrected for finite-size effects and the effective suspension viscosity.

$\sqrt{u_\tau^2(1 - \delta_{pw}/h)}$ and the effective suspension viscosity ν^e , yielding $Re_\tau^{e*} = u_\tau^*(h - \delta_{pw})/\nu^e$. The relations derived in Costa et al. [28] read,

$$\frac{u}{u_\tau^*} = \frac{1}{\kappa} \ln \left(\frac{y - \delta_{pw}}{\delta_v^{e*}} \right) + B, \quad (5.1)$$

$$\frac{U_c - u}{u_\tau^*} = -\frac{1}{\kappa} \ln \left(\frac{y - \delta_{pw}}{h - \delta_{pw}} \right) + B_d, \quad (5.2)$$

with $\delta_v^{e*} = \nu^e/u_\tau^*$; the coefficients κ , B and B_d retain the values of single-phase flow whereas the effective viscosity is obtained from Eilers fit $\nu^e/\nu = (1 + (5/4)\Phi/(1 - \Phi/\Phi_{max}))^2$ [133]. The virtual wall origin of the HSR is given by $y = \delta_{pw} = C(\Phi/\Phi_{max})^{1/3}D_p$. These scaling laws can be further used to derive a master equation that accurately predicts the overall drag of the suspension, here expressed in terms of a friction Reynolds number:

$$Re_\tau = \frac{Re_b}{2\xi_{pw}^{1/2}} \left(\frac{1}{\kappa} \left[\ln \left(Re_\tau \chi^e \xi_{pw}^{3/2} \right) - 1 \right] + B + B_d \right)^{-1}, \quad (5.3)$$

or, in an explicit form based on a similar correlation for single-phase flow from Pope [116],

$$Re_\tau = \frac{0.09 (Re_b \chi^e \xi_{pw})^{0.88}}{\xi_{pw}^{3/2} \chi^e}, \quad (5.4)$$

where $\xi_{pw} = (1 - \delta_{pw}/h)$ and $\chi^e = \nu/\nu^e$.

Table 5.2 presents the mean wall shear, expressed in terms of the friction Reynolds number $Re_\tau = u_\tau h/\nu$ from the different simulations considered here. As expected from eq. (5.3) and eq. (5.4), the addition of finite size neutrally-buoyant particles results in an increase in drag with respect to the value of 350 of the single phase flow, which (when

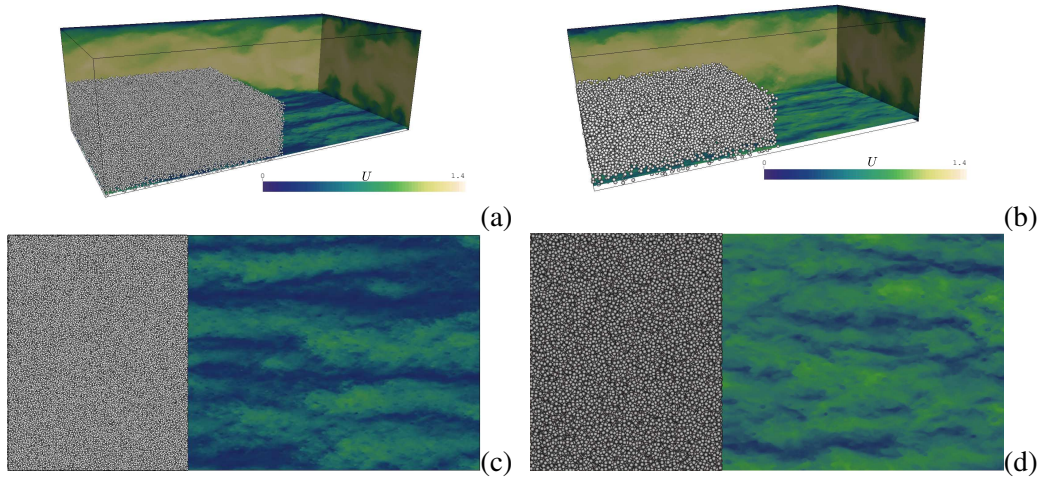


Figure 5.1: Instantaneous snapshots of the flow for cases D10 (a) and D20 (b). The contours show the of magnitude of streamwise velocity (normalized by U_b) in three mutually-perpendicular planes. Particles are illustrated in part of the domain. The bottom plane corresponds to a wall-normal distance of $y = 1.5D_p$, also shown in a 2D perspective in panels (c) (D10) and (d) (D20).

fixing the other governing parameters) increases with increasing particle size. We first note that the smaller the particles, the more the *suspension* friction Reynolds number $Re_\tau^e = Re_\tau \nu / \nu^e$ approaches the value obtained in the continuum limit, CLR; in other words using an effective viscosity provides a better prediction of the total drag. This is a consequence of the smaller finite-size effects that typically occur near the wall [28].

Finally, the third column in the table shows the suspension Reynolds number of the HSR, $Re_\tau^{e*} = Re_\tau^e (1 - \delta_{pw}/h)^{3/2}$, obtained considering both an effective suspension viscosity and a virtual wall origin as explained above (with δ_{pw} computed with $C = 1.5$ and $\Phi_{max} = 0.6$). The friction Reynolds numbers from the interface-resolved simulations are, in this case, equal for both particle sizes and very close to the value of $Re_\tau \nu / \nu^e$ for the CLR case. This strongly supports the proposed correction for finite-size effects.

Figure 5.1 displays snapshots of the flow for the two laden cases, D10 and D20. The top panels show planar sections colored by the streamwise flow velocity, and particle positions only shown for streamwise locations smaller than $0.4L_x$ and wall-normal distance $y < h$. The bottom plane (also shown in the two planar views, in the bottom panels) corresponds to a wall-normal position $y = 1.5D_p$, corresponding to about $y/\delta_\nu = 15$ and 30 for cases D10 and D20. The figures show the typical near-wall low-speed streaks found in single-phase wall-bounded turbulence, also present in these suspensions [112]. Differences in velocity contrast between the two cases can be attributed to the choice of a plane at wall-normal distance that scales with the particle diameter, meaning that, in viscous units, the plane corresponding to case D10 is closer to the wall. However, in

both cases the maximum streak amplitude is achieved at relatively larger wall-normal distances than what is expected for single-phase flows, as illustrated in figure 5.2. This figure depicts contours of autocorrelations of the streamwise suspension velocity (i.e. computed from the fluid flow field with rigid body motion inside the particles) $R_{uu}^z(y, \Delta z) \equiv \langle u'(y, z)u'(y, z + \Delta z) \rangle / \langle u'^2(y) \rangle$, averaged in time and in the streamwise direction for different spanwise separations. Panels (b) and (c) show the results for the interface-resolved simulations D10 and D20. Clearly the near-wall minima – footprint of the low- and high-speed streaks [80], and near-wall property that should scale in inner units – are shifted upwards, and the larger the particles are, the larger this shift is. Figure 5.2 also shows that the smaller the particles are, the closer the suspension dynamics resemble the continuum limit, CLR. This can be seen when comparing panel (d), corresponding to the continuum limit CLR to panels (b) – D10 and (c) – D20. There is a clear qualitative discrepancy between the CLR and the bigger particles (D20), contrasting with a significant quantitative agreement between CLR and the case with small particles (D10). For the case of bigger particles (D20), the wall-normal minimum is located at such a large distance to the wall ($\approx 0.3h$) that inner-to-outer scale separation is compromised. Also, the autocorrelations for the interface-resolved cases show a non-monotonic trend at wall-normal distances $y \lesssim D_p$, where the autocorrelation (for fixed y) reaches a local maximum close to the wall. This can be even better observed from the profile of the integral length scale $L_{xz} = \int_{-L_z/2}^{+L_z/2} R_{uu}^z d(\Delta z)$, indicated by the dashed lines in the figure. This confirms that the flow dynamics in this region is qualitatively different from what a simple continuum rheological description would predict.

FLOW DYNAMICS IN THE PARTICLE-WALL LAYER (PWL)

Next we investigate in more detail the flow dynamics in the particle-wall layer. Panel (a) of figure 5.3 depicts the mean streamwise fluid velocity in inner units. Note that the viscous wall unit used for inner-scaling is defined, for consistency, with the effective suspension viscosity at the same volume fraction, as we are ultimately interested in the deviations of the flow dynamics from the continuum limit. For wall-normal distances $y \gtrsim 10\delta_v^e$, the profile for the case D10 (smaller particles) clearly shows a logarithmic scaling, with a von Kármán constant $\kappa = 0.36$. On the other hand, case D20 does not show a clear logarithmic region because of the larger extent of the PWL [28].

Panel (b) of figure 5.3 presents the difference between the fluid- and solid-phase velocity profiles, expressed in terms of a particle Reynolds number $Re_p = (u_p - u_f)D_p/\nu$. Profiles pertaining to the solid phase are obtained by averaging over the rigid body motion of the particles. Two regions can be clearly distinguished in the figure, roughly separated by the line marking the wall-normal distance $y = D_p$. For $y \gtrsim D_p$, the difference between the velocity of the two phases is small, whereas the profiles clearly deviate for wall-normal distances $y \lesssim D_p$, reaching the highest (apparent) particle-to-fluid slip ve-

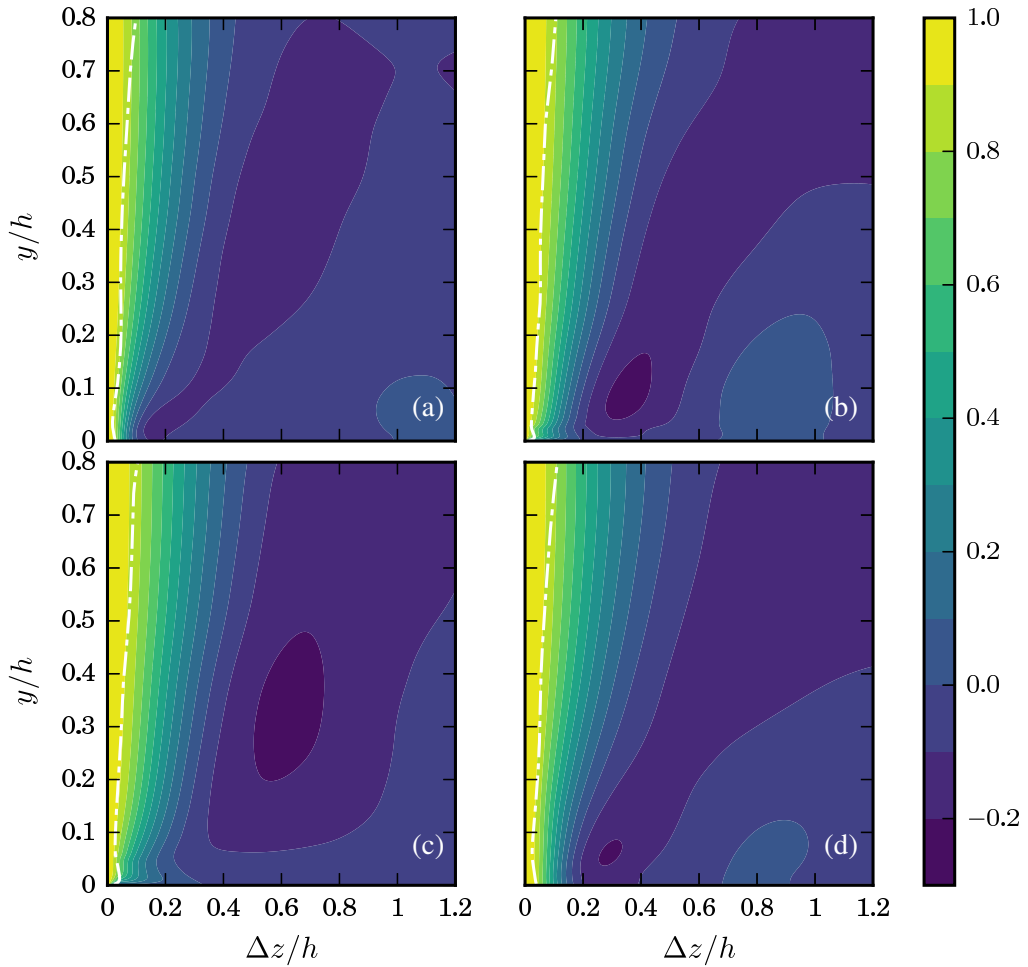


Figure 5.2: Autocorrelations of streamwise velocity R_{uu}^z as a function of the wall-normal distance, y , for spanwise separation distances Δz (both scaled with h) for cases SPR (a), D10 (b), D20 (c) and CLR (d). The dashed lines denote the profile of integral scale $L_{xz}(y)$.

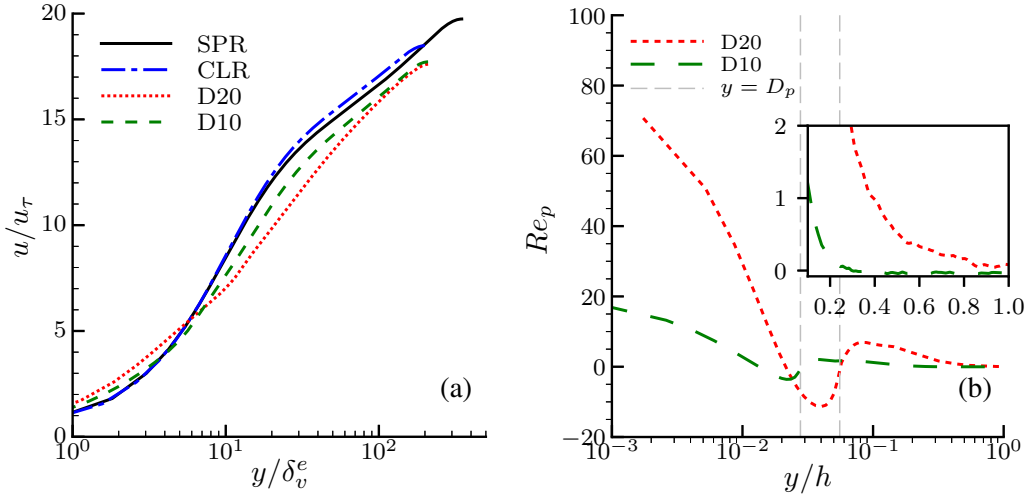


Figure 5.3: (a) Mean streamwise (inner-scaled) fluid velocity and (b) profile of particle Reynolds number based on the (apparent) particle-to-fluid slip velocity $Re_p = (u_p - u_f)D_p/\nu$. Vertical dashed lines indicate the wall-normal distance corresponding to one particle diameter. The inset shows the same quantities, but with a linear-linear scale, to highlight the differences in particle Reynolds number in the bulk.

locity at the wall. This is a signature of particle layering due to the kinematic constraint that the wall imposes on the particles. Particles flowing at the wall acquire most of their linear momentum at wall-normal distances higher than their radius and this is transported uniformly throughout their volume. Conversely, the fluid momentum must vanish at the wall. An important result that figure 5.3 (b) shows (see also its inset) is that the particle Reynolds number in the bulk is virtually zero for case D10, while it still assumes values of $O(1)$ for case D20. This evidence of finite particle inertia in the bulk can result in inertial-shear-thickening effects, see [114]. We will come back to this when the dynamics of the homogeneous suspension region are discussed.

The near-wall layer of particles impacts the scale separation on which the scaling laws for mean velocity are based. It is therefore interesting to understand how the near-wall inhomogeneity affects the particle structure, and how far this inhomogeneity extends in the wall-normal direction. We can quantify this through the angular distribution function at contact (ADF). The ADF measures the probability of finding a particle pair at a fixed distance r , as a function of the polar (θ) and azimuthal (φ) angles, normalized by the values of a random particle distribution. Formally,

$$g(\theta, \varphi) = \frac{1}{r^2 \sin(\theta)} \frac{d^2 N_{\theta, \varphi}}{d\theta d\varphi} \frac{1}{n_0}; \quad n_0 = \frac{N(N-1)}{2V} \quad (5.5)$$

where $N_{\theta, \varphi}$ denotes the number of particles on a segment of a spherical surface of radius $r = D_p/2$, and polar and azimuthal angles within the ranges $\theta' \in [0, \theta]$ and $\varphi' \in [0, \varphi]$.

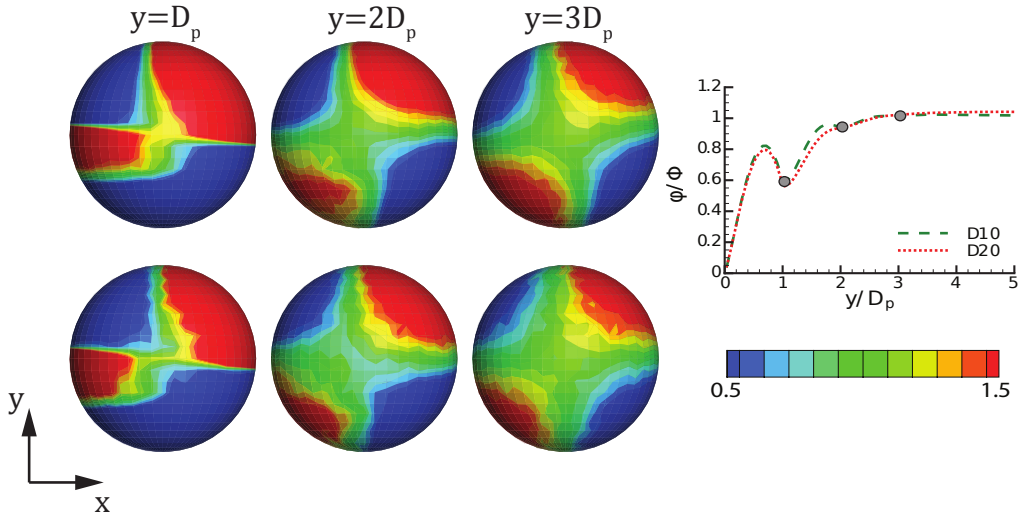


Figure 5.4: Projection onto the $x - y$ plane of the angular distribution function at contact for simulation D10 (top) and D20 (bottom). Statistics are obtained within wall-normal slots of size D_p , centered at $y/D_p = 1, 2$ and 3 (flow is from right to left). The curves on the right are the profiles of the mean local volume fraction, ϕ/Φ versus the wall-normal distance y/D_p , with the markers denoting the locations where the ADF are sampled.

The ADF is computed from the simulation data using bins with wall-normal extent D_p , centered at $y/D_p = 1, 2$, and 3 , i.e. at the same wall-normal distance if scaled with the particle size.

The projection of the ADF onto the $x - y$ plane is displayed in figure 5.4 for the two cases under investigation. For a suspension in homogeneous shear, the particles tend to be preferentially attracted towards each other when located in a compression region (negative local strain) and reciprocally repelled from each other when located in a stretching region [105]. This results in a distribution with two planes of symmetry: two regions of higher clustering in the $xy > 0$ quadrants and two of lower accumulation in the $xy < 0$ quadrants. The inhomogeneity introduced by the wall, bounding the particle trajectories, induces a deviation from this picture. The wall-effect vanishes for wall-normal distances $y/D_p \gtrsim 3$ for both simulations. Interestingly, both ADF agree quantitatively. As the distance from the wall is normalized by the particle diameter, for fixed volume fraction, the wall inhomogeneity affects the particle dynamics at distances proportional to D_p , despite the different local behavior (different wall-normal location in viscous units) of the suspending fluid.

Let us now investigate the influence of the particle-wall layer on the distribution of wall shear-stress. To this end, we report in figure 5.5 contours of the instantaneous wall-shear for the case D20, together with the particle positions close to the wall (shown with transparency). The data reveal a strong correlation between regions of high shear and the particle location. This can explain the increase in drag with respect to predictions from

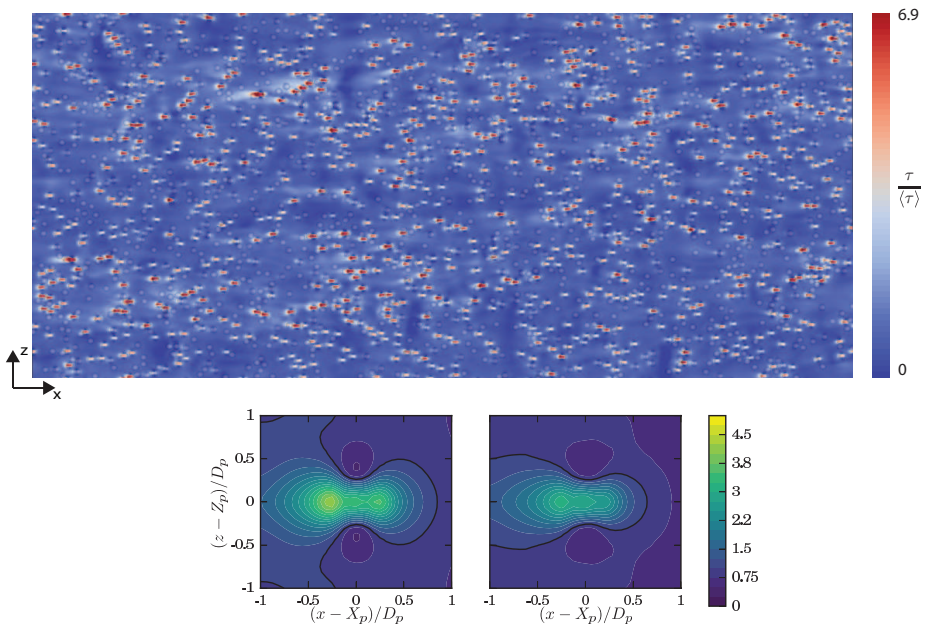


Figure 5.5: Contours of wall shear stresses (normalized with the corresponding mean value) for case D20 (top). Mean wall shear conditioned to the locations of the near-wall particles and normalized with the mean wall shear (bottom) for cases D10 (left) and D20 (right). The data are extracted from the average of the top and bottom walls for one temporal realization.

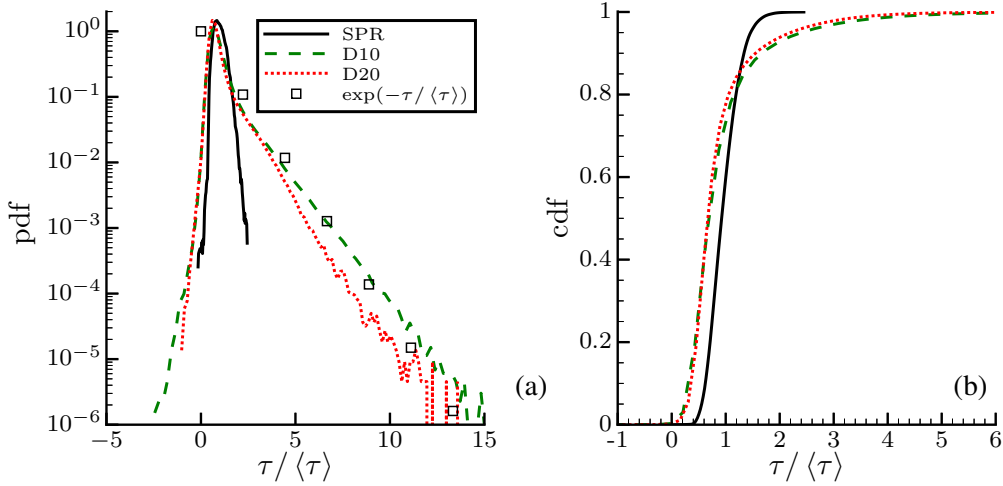


Figure 5.6: (a) Probability density function and (b) corresponding cumulative distribution function of wall shear stress (normalized with its global mean ρu_{τ}^2) for cases D20, D10 and SPR (a).

the continuum limit: high particle-to-fluid apparent slip velocity close to the wall corresponds locally to events of high wall shear stress, which are not present in the ‘equivalent’ single-phase flow with a modified suspension viscosity. Panel (b) of the same figure shows the mean wall shear conditioned to the particle positions. Results for small and large particles show a similar qualitative behavior: the shear is higher than the mean around the particles, except close to the surface of the particle, in the spanwise direction. This is a consequence of the reduction of streamwise velocity as the fluid moves around the particle. The contours of the shear stress for the smaller particles show a higher local increase in shear stress, which is, on the other hand, more localized. In fact, the contribution of these *hot spots* of shear stresses to the total shear is the same for both cases D10 and D20, and quite high: 69%.

The probability density function (pdf) of the shear stress distribution for cases D20, D10 and SPR, presented in figure 5.6, shows a clear difference between the typical distribution of shear stresses for a single-phase flow, and for the particle-laden cases. In the presence of particles, the tails of the pdf are greatly widened, with very high probability of finding values of the shear stress up to 4 times the mean value, and likewise for values lower than the mean, including negative events. We note there that it is reported for single-phase flow that $\tau_w^{+,rms} = \tau_w^{rms} / \langle \tau_w \rangle \approx 0.4$ and that the pdf typically follows a log-normal distribution [109]. Indeed, we obtained a value of $\tau_w^{+,rms} = 0.39$ for case SPR, with a pdf well-fitted by a log-normal distribution (not shown). The hot-spots of high shear cause a striking difference for the laden cases: $\tau_w^{+,rms} = 1.1$ and 1.0 for cases D10 and D20. Moreover, the pdf no longer fits a log-normal distribution. The hot-spots of high wall shear induce a *kink* in the pdf for $\tau \gtrsim \langle \tau \rangle$, resulting in a clear exponential tail,

fitted by $\lambda \exp(-\lambda\tau/\langle\tau\rangle)$ with $\lambda \approx 1$. Further, case D10 shows higher probability of extreme events, (which, again, are more localized). The largest values attained by the shear stress that in single-phase flows do not contribute significantly to the mean shear, account for about 10% of the total in particle-laden channel flows, as shown by the cumulative probability distribution function (cdf) displayed in panel (b).

The results presented so far shed light on the relation between the wall slip velocity $U_{pw} = u_p(y=0)$ and the wall friction u_τ (recall figure 5.3 b). Assuming that (1) the average shear in the hot-spots matches the average wall shear and (2) the particles impose a mean shear that scales with U_{pw}/D_p over an area $D_p L_w$ (L_w being the streamwise extent of the hot-spot, which as seen in figure 5.5 is significantly larger than D_p), we can write:

$$N_{pw} D_p L_w \mu \frac{U_{pw}}{D_p} = \rho u_\tau^2 L_x L_z, \quad (5.6)$$

where N_{pw} is the number of particles in the particle-wall layer. Further noting that $N_{pw} D_p^3 / (D_p L_x L_z) \sim \Phi$, we have

$$\Phi \frac{L_w}{D_p} \frac{U_{pw}}{D_p} \sim \frac{u_\tau^2}{\nu}, \quad (5.7)$$

and finally, assuming that L_w/D_p scales as the mean-free-path in a two-dimensional layer of particles, i.e., $\propto \Phi^{-1/2}$, we obtain

$$\frac{U_{pw}}{u_\tau} = C_{pw} \text{Re}_\tau^p \Phi^{-1/2}, \quad (5.8)$$

with $\text{Re}_\tau^p = u_\tau D_p / \nu$ being particle friction Reynolds number. The data in figure 5.7, including previous cases in literature, confirm the validity of this relation with $C_{pw} \approx 0.2$. The data points that do not follow the predicted scaling correspond to very large particles ($h/D_p = 5$), for which the influence of the outer scales on the near-wall particle dynamics compromises the first assumption above, and to low volume fractions.

HOMOGENEOUS SUSPENSION REGION (HSR)

The contribution of the different stresses to the suspension streamwise momentum transport (i.e. the stress budget) can be derived from volume- and ensemble-averaging the mixture streamwise momentum equation, see [96, 112]. It reads for plane channel flow

$$\langle\tau\rangle = u_\tau^2 \left(1 - \frac{y}{h}\right) = \underbrace{(1 - \phi) \langle -u'_f v'_f \rangle}_{\tau_{Tf}} + \underbrace{(1 - \phi) \nu \frac{d u_f}{d y}}_{\tau_v} + \underbrace{\phi \langle -u'_p v'_p \rangle}_{\tau_{Tp}} + \tau_p, \quad (5.9)$$

where the terms on the right-hand-side denote the fluid Reynolds stresses τ_{Tf} , the viscous stresses τ_v , the particle Reynolds stresses τ_{Tp} , and the particle stresses τ_p , the latter

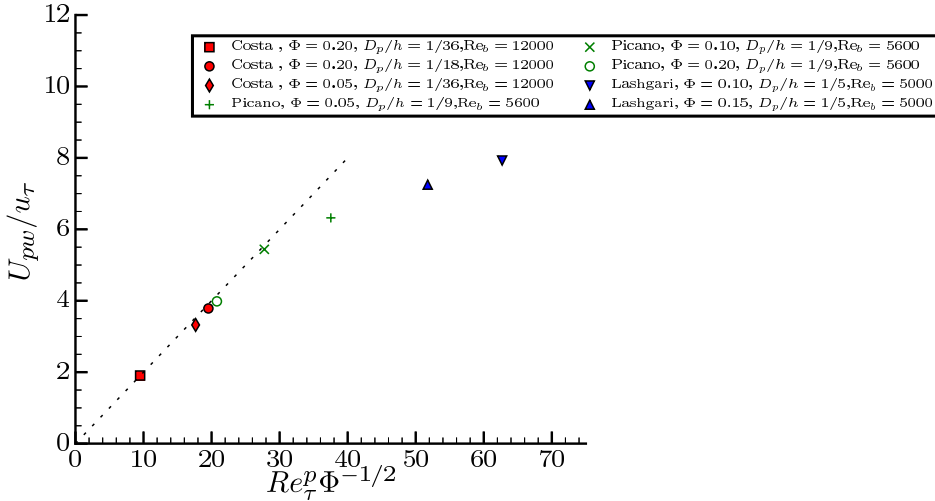


Figure 5.7: Particle-to-fluid slip velocity U_{pw} normalized with the wall friction velocity u_{τ} vs $Re_{\tau}^p \Phi^{-1/2}$ (see definition in the text). To support the validity of the proposed scaling, data from Picano, Breugem, and Brandt [112] and Lashgari et al. [84] are also included.

related to the stresslet, moment of the material acceleration acting on a particle and inter-particle collisions [58]; in the expression above, ϕ denotes the mean local solid volume fraction. The wall-normal profiles of the different contributions to the total stress (obtained dividing eq. (5.9) by $u_{\tau}^2(1 - y/h)$) are reported in figure 5.8. As also observed in [84, 85, 112] the profiles of particle stresses reach a maximum at $y = D_p/2$, at the location of the local maximum of the profiles of the local volume fraction (see figure 5.4), followed by a minimum at $y \sim 2D_p$. Further away from the wall, the profiles follow a trend that resembles the one of the shear-stress profile, suggesting a linear (Newtonian) scaling of the particle stresses with the shear rate. The Reynolds stresses are relatively small in this region, and therefore the local maximum/minimum of the particle stresses is compensated by a local minimum/maximum of the viscous shear stresses. This is caused by the strong shear that the first layer of particles, flowing with significant slip velocity, imposes on the fluid above it.

The deviation from the continuum limit (CLR) can be examined by comparing the sum of the particle and viscous stresses to the profile of viscous stresses in panel (d) of figure 5.8 (note that an effective viscosity incorporates the effects of both viscous and particle stresses). As expected, the case with smaller particles is much closer to this continuum limit than the case with larger particles (see also [28]). For the latter, while the profile pertaining to the viscous contribution in the bulk is still close to the one of case D10, the particle stress contribution is much larger. This difference can be attributed to the *inertial-shear-thickening* mechanism due to excluded volume effects proposed in Picano et al. [114], as the particle Reynolds number based on the particle slip velocity for

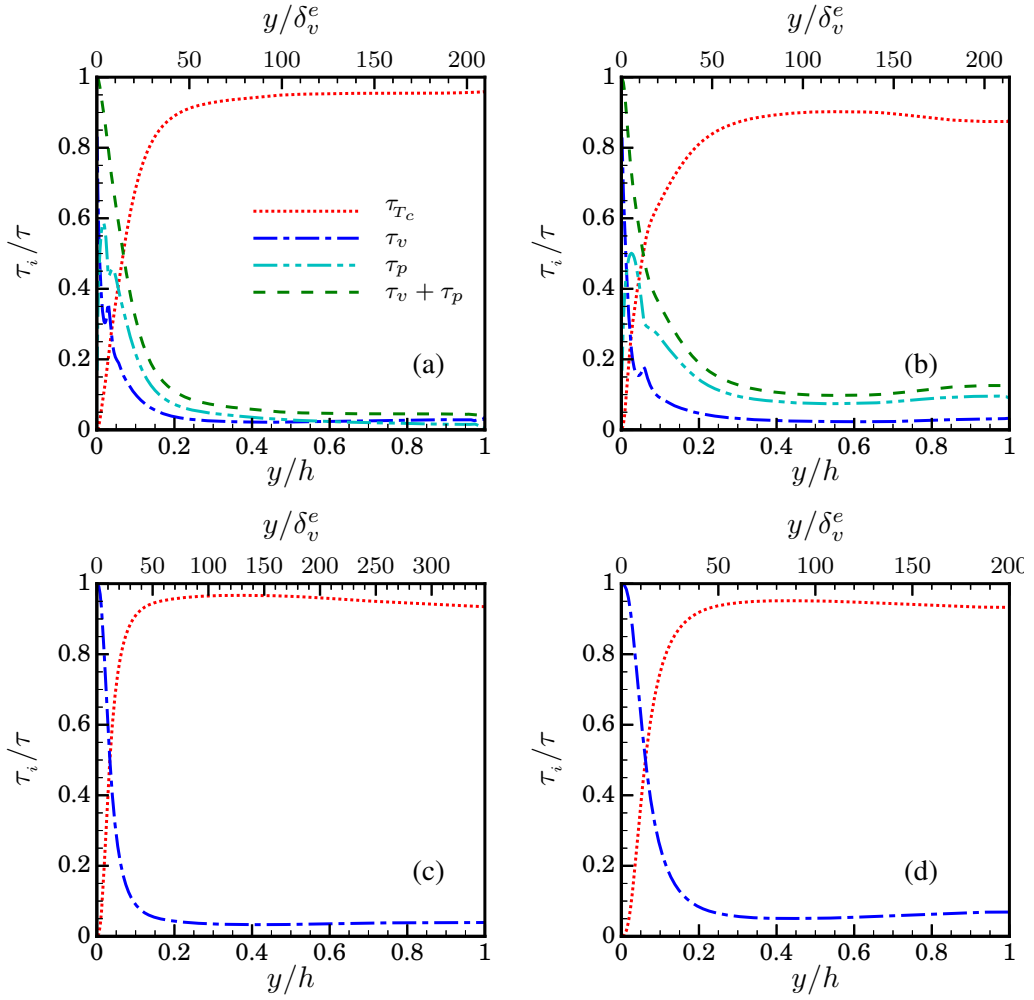


Figure 5.8: Stress contributions $\tau_i(y)/(u_\tau^2(1 - y/h))$ for the different cases D10 (a), D20 (b), SPR (c) and CLR (d), see eq. (5.9). $\tau_{Tc} = \tau_{Tf} + \tau_{Tp}$ denotes the contribution of the Reynolds stresses of the combined phase.

case D20 is much larger (recall figure 5.3 (b)). We should stress here the importance of defining the viscous wall unit from the effective suspension viscosity: if the profiles of cases D10 and D20 would be compared to CLR using the classical inner scaling (where the fluid viscosity and wall friction velocity are used to scale the wall-normal distance) these would not match, as the abscissa on the upper axis y/δ_v^e would have to be multiplied by $\nu^e/\nu = 1.89$ in panels (a) and (b).

As for the other quantities presented so far, we expect the second-order Eulerian statistics for the laden cases to approach those of CLR with decreasing particle size. These are shown in figure 5.9 where we depict the profiles of the root-mean-square (rms) of the fluctuating fluid velocity and Reynolds stresses from the different simulations. When comparing to the single-phase flow statistics we also observe, as reported in Picano, Breugem, and Brandt [112], that the fluctuating fluid velocity close to the wall is enhanced by the presence of the particles.

Let us take one step further and test the scaling arguments of Costa et al. [28] for the second-order statistics. These can be compared directly to the case CLR, as it is meant to be the same flow, finite size effects aside. We therefore correct the wall-normal distance for the presence of the particle-wall layer through a virtual wall origin, δ_{pw} , and correct velocity scale for inner-scaling, $u_\tau^* = u_\tau(1 - \delta_{pw}/h)^{1/2}$ (panels a, c, e and g in the figure). The magnitude of near-wall peaks in streamwise velocity rms, typically located at $y = 12\delta_v \lesssim D_p$, are not recovered in the interface-resolved simulations. Despite this, away from the wall (where the dynamics is only weakly affected by the particle-wall layer due to sufficient scale separation) the profiles show good agreement. Particularly, the profiles pertaining case D10 show a remarkable collapse over the entire outer region for all three components of the velocity rms and Reynolds stresses, even without correction. The same cannot be safely stated for the case with larger particles (D20) where finite size effects, also present away from the particle-wall layer, have an influence on the statistics in the bulk of the flow. Despite these small deviations for case D20, it is clear that, away from the wall, the second-order statistics are described with good approximation by those of a Newtonian fluid with an effective suspension viscosity.

PARTICLE DYNAMICS

Analyzing the mean flow solely in an Eulerian framework does not give direct insights on the dynamics of individual particles. To understand the particle dynamics, we further explore the DNS dataset by computing Lagrangian statistics. We first focus on the evolution of the single-point mean-square displacement of particles in the spanwise direction to prevent biases due to statistical inhomogeneity in the wall-normal, and non-zero mean flow in the streamwise direction (see also Lashgari et al. [85]). This is defined as

$$\langle \Delta z_1^2 \rangle (\Delta t, y) = \langle (z(t + \Delta t) - z(t))^2 \rangle \quad (5.10)$$

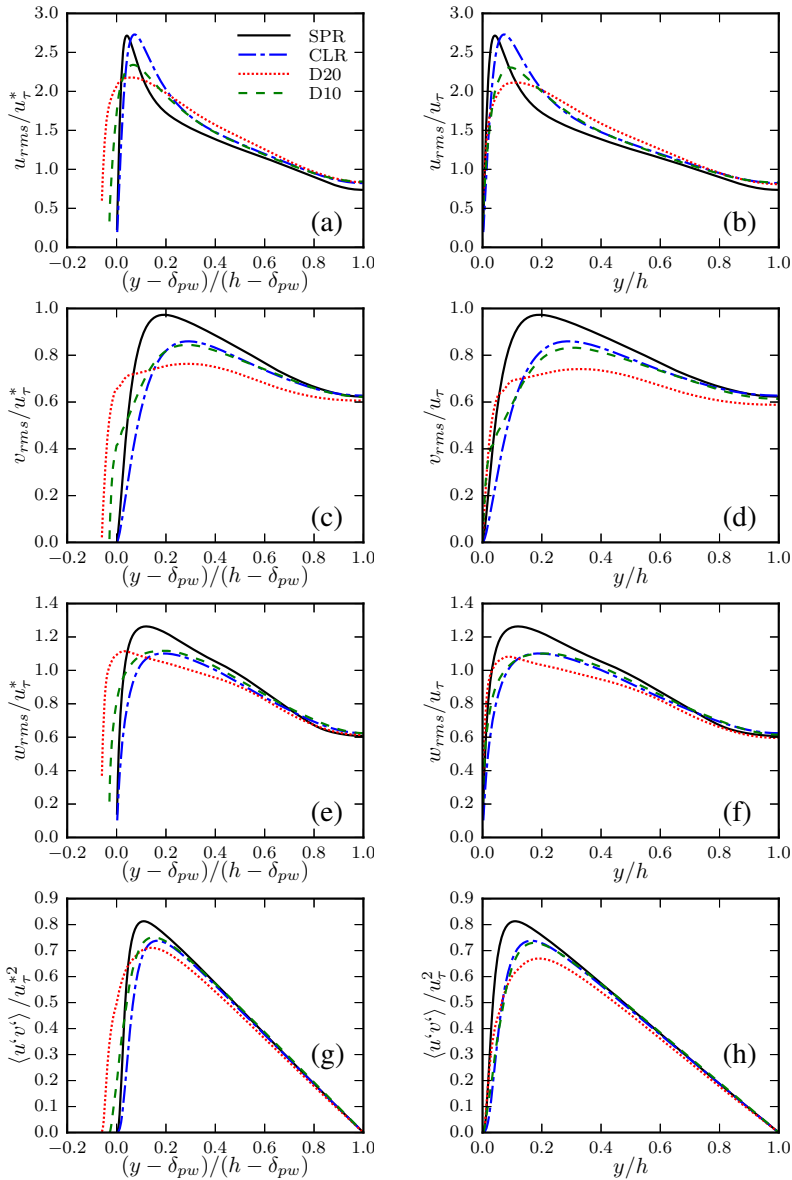


Figure 5.9: Profile of rms of fluctuating streamwise, spanwise and wall-normal fluid velocity from the different simulations. Classical scaling is used in panels (a,c,e,g), whereas the scaling laws of Costa et al. [28] are used in panels (b,d,f,h).

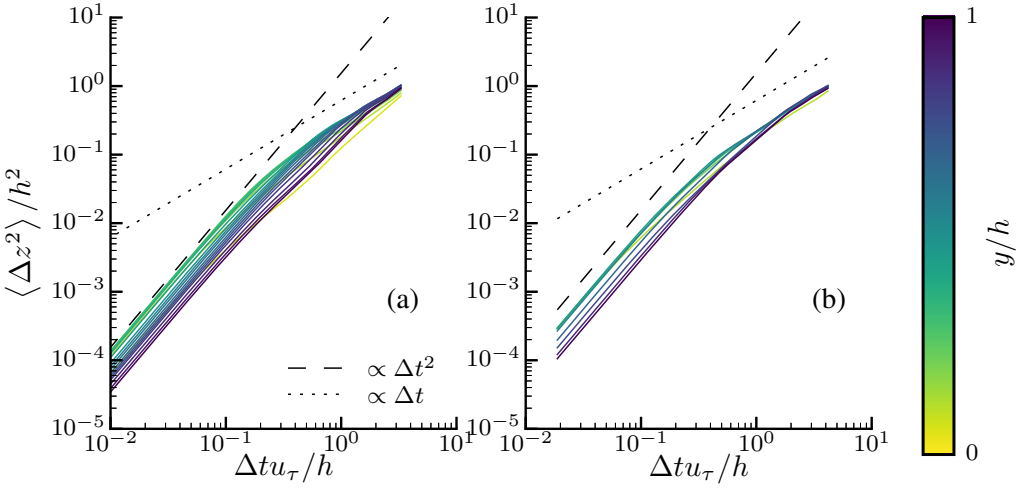


Figure 5.10: Single-particle mean square spanwise displacement $\langle \Delta z^2 \rangle (\Delta t, y)$ normalized with the half channel height h^2 , for cases (a) D10 and (b) D20 versus time in units of the integral time scale h/u_τ . The colors indicate different wall-normal distances.

where $\langle \rangle$ denotes the time average over all particles located in a bin centered at a wall-normal position y at time t and wall-normal extent D_p . This observable is displayed in figure 5.10 versus time in units of a characteristic integral scale of the turbulent fluid motion, h/u_τ . One can observe two well-known regimes: the ballistic regime where the high temporal correlation results in a mean square displacement $\langle \Delta z^2 \rangle \propto \Delta t^2$ and the diffusive regime where the motion decorrelates from the initial sampling instant and $\langle \Delta z^2 \rangle \propto \Delta t$ (see e.g. Sierou and Brady [129]). In the ballistic regime, particles reach the fastest dispersion at the distance from the wall corresponding to the peak in particle velocity rms (see figure 5.9). The diffusion coefficient (slope of the profile in the diffusive regime) is nearly the same for the different cases, away from the wall. Two main mechanisms are responsible for the spanwise particle displacements and the subsequent self-diffusion: (1) short-range inter-particle interactions and (2) interactions with turbulent structures of dimension larger than the particle size. One can picture a sequence of these events as successive random-walk steps during the particle motion. Indeed, Lashgari et al. [85] observed in the turbulent regime an increase of the diffusion coefficient with increasing Reynolds number for fixed volume fraction, and a milder increase with increasing volume fraction at fixed Reynolds number. The smaller diffusion coefficients observed near the wall can therefore be explained by the constraint that the wall confinement imposes on the particle motion and by the reduction of the characteristic turbulent integral scale, estimated as $l_m(y) \sim \min(\kappa y, 0.1h)$, with l_m being a mixing length [116]. The turbulent length scales are hindered up to a point where $l_m \sim D_p$, the value below which turbulent fluctuations have a weak influence on the particle kinematics. Despite the relatively small particle

inertia, the temporal filtering due to the higher response time of the larger particles [62] can also cause a decrease in diffusion coefficient. We expect however the latter effect to be milder, as increasing particle inertia through an increased mass density (while fixing the other governing parameters) has a small influence on spanwise particle dispersion, as shown in Fornari et al. [48].

The diffusion coefficient is larger for the flow with smaller particles (D10), even though the collision probability is larger for the largest particles (as suggested by the asymptotic limit of vanishing particle size at fixed volume fraction, and will be confirmed later). We can therefore conclude that, at the volume fraction under consideration here, the turbulent fluid motion is the main source of self-diffusion and, consequently, larger particles result in slower dispersion. Note also that the diffusive regime is reached away from the wall at times $\Delta t = O(h/u_\tau)$ of the same order as the turnover time of large eddies in the bulk, consistently with this observation.

Further insight into the particle dynamics can be gained by examining the pair-dispersion statistics. The two-point mean spanwise square displacement is displayed in figure 5.11 for two particles at contact at $t = t_0$,

$$\langle \Delta z_2^2 \rangle (\Delta t, y) = \left\langle (\delta z(t_0 + \Delta t) - \delta z(t_0))^2 \right\rangle, \quad (5.11)$$

where δz denotes the spanwise interparticle distance and t_0 the instant at which the particles are in contact. For short time scales, lubrication dominates and the particles display a highly correlated motion. The duration of this regime increases with the distance to the wall. This slower relative dispersion is linked to the decreasing relative inter-particle velocity towards contact with increasing wall-normal distance, to be quantified later. The large particles, case D20, show faster pair dispersion, also due to higher relative inter-particle velocity towards contact: it turns out, as elaborated later when the collisional dynamics is addressed, that this quantity scales with the particle Reynolds number. At later times, the particle dispersion $\langle \Delta z_2^2 \rangle \propto \Delta t^\alpha$, with $2 < \alpha < 3$. Note that for tracer particles in a homogeneous isotropic turbulent flow $\alpha = 3$ for separation distances within the inertial subrange [124]. For larger separation distances the diffusive limit is recovered.

The mean square displacement of tracer particles in turbulence with sub-Kolmogorov separation distance (i.e. in the *dissipation subrange*) grows exponentially in time as the relative particle velocity and the separation are proportional [10, 124]: i.e. $\langle \delta z_2^2 \rangle = \langle \delta z_0^2 \rangle e^{2\Delta t/t_c}$, where t_c is a characteristic inter-particle response time. Although in the present study D_p is $O(10)$ times larger than the smallest turbulence scale, we observe a clear exponential growth at short times, just after the first highly correlated regime when $\langle \Delta z_2^2 \rangle$ is approximately constant. The time at which this exponential regime sets in corresponds to a mean square separation of about $\sqrt{2D_p^2/3}$. This exponential regime is highlighted in the bottom panels of figure 5.11 where the time on the horizontal axis is divided by $\Delta t^l = \Delta t|_{\langle \Delta z_2^2 \rangle = 2D_p^2/3}$. This growth is due to a different mechanism than the one of tracer particles, possibly the combination of a uniform shear force (note that under uni-

form shear δz is proportional to the relative velocity) following a short-range lubrication interaction.

Finally, we investigate the particle collisional dynamics. A collision event takes place when (1) the particles are at sufficiently close distance and (2) their relative velocity drives them towards contact. These two factors are investigated separately. The first by the radial distribution function (RDF), which quantifies the probability of finding a second particle at distance r normalized by the probability of a random distribution of particles:

$$g(r, y) = \frac{1}{4\pi r^2} \frac{dN_r}{dr} \frac{1}{n_0}, \quad (5.12)$$

where N_r denotes the number of particle pairs in a spherical volume of radius r . Thus, if $g(r, y)$ assumes values larger than 1, particles are preferentially sampled. The second observable is the distribution of the relative particle velocity projected in the direction of the line-of-centers $\Delta v^{n,-}$, given for two particles i, j with velocities $\mathbf{u}_{i/j}$ and positions $\mathbf{x}_{i/j}$ by:

$$\Delta v^{n,-}(r, y) = \max \left\{ 0, -(\mathbf{u}_j - \mathbf{u}_i) \cdot \frac{\mathbf{x}_j - \mathbf{x}_i}{|\mathbf{x}_j - \mathbf{x}_i|} \right\}; \quad (5.13)$$

where the $\max\{\}$ operator samples the relative velocity *towards* contact, as the superscript ‘ $-$ ’ suggests. The product of these quantities measures the rate at which particles approach each other. Its value for $r = D_p$ is the so-called collision kernel, κ_c , the probability of a collision event.

As for the dispersion statistics, we take into account the inhomogeneity in the wall-normal direction by averaging in wall-parallel bins with wall-normal extent $2D_p$. Figure 5.12 presents the radial distribution function, negative particle relative velocity and the approach rate at contact $r = D_p$. The profile of $\Delta v^{n,-}$ shows that the dominant mechanism driving particles towards each other is shear from particles at different wall-normal locations. Note that the shear rate away from the PWL is similar for both simulations considered (see figure 5.8 and table 5.2). Assuming that particles are driven towards each other by shearing a layered arrangement of particles:

$$\Delta v^{n,-} \propto D_p \frac{\partial u}{\partial y} \sim D_p \frac{u_\tau}{h}, \quad (5.14)$$

with u_τ/h an estimate of the shear rate in the bulk of the flow. This scaling is tested in the inset of panel (b) and (c), yielding a better agreement of the profiles of $\Delta v^{n,-}$ and κ_c , despite the differences in $g(D_p)$. Note that u_τ/h is approximately the same for both cases (table 5.2). The higher values of g at close distances for case D20 are also compatible with this picture, as larger particles are more prone to be driven towards each other by a shear-induced relative motion.

Figure 5.13 shows contour plots of the same quantities, as a function of the separation distance r and of the wall-normal coordinate y . The contours of g show that this quantity

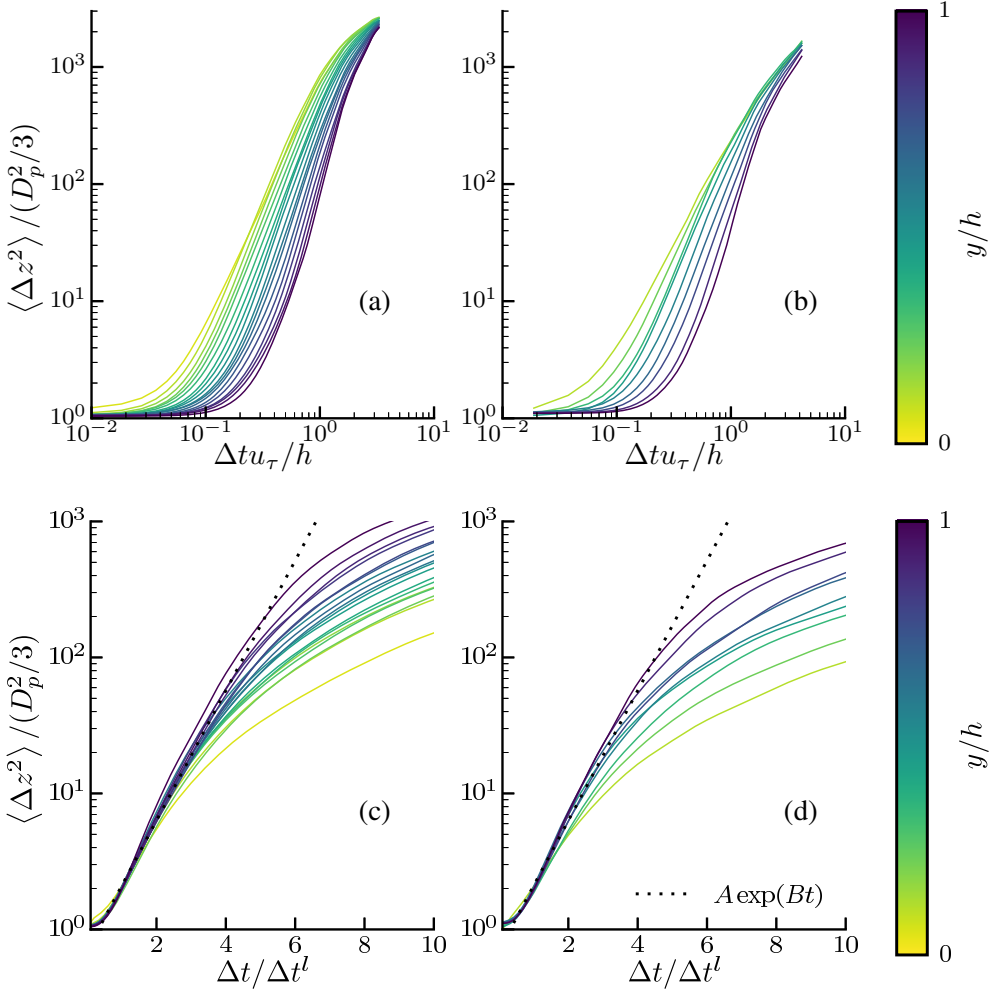


Figure 5.11: Two-particle mean square spanwise displacement $\langle \Delta z^2 \rangle (\Delta t, y)$ normalized with the mean initial spanwise square distance at contact $D_p^2/3$ for (a) case D10 and (b) case D20 versus time normalized with by the integral time scale h/u_τ . The different lines are color-coded to indicate the particle wall-normal distance. Panels (c) and (d) illustrate the initial exponential scaling by plotting the same quantity versus $\Delta t^l = \Delta t|_{\langle \Delta z^2 \rangle = 2D_p^2/3}$ (see discussion in the text). The dotted-lines indicate the fitting function $A \exp(Bt)$ with $A = 0.7$ and $B = 1.1$.

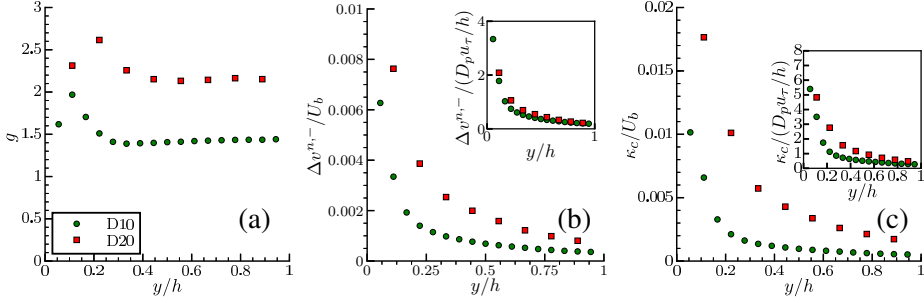


Figure 5.12: (a) radial distribution function $g(D_p)$ at contact; (b) normal relative velocity at contact $\Delta v^{n,-}(D_p)/U_b$ and (c) collision kernel κ_C/U_b versus the outer-scaled wall-normal distance y/h . The insets of panels (b) and (c) show the same quantity scaled with the velocity scale $u_\tau D_p/h$, see eq. (5.14).

is weakly dependent on the wall-normal coordinate, with local maxima at $r/D_p \approx 1$ and 2, consistent with the presence of statistically significant particle pairs and triplets. It is also interesting to notice that the global maximum of g occurs at a finite distance to the wall. Comparing the two simulations, the maximum is located at the same wall-normal distance when scaled with the particle diameter $y \sim 3D_p$, in agreement with the observation above that wall-confinement effects are noticeable at distances proportional to the particle diameter (see figure 5.4). The maxima of $g(r)$ correspond therefore to the optimal trade-off between high shear (driving particles at different wall-normal locations towards each other) and low confinement; indeed further away from the wall, where the mean shear is relatively low, g becomes almost independent of y . The maxima of g close to the wall also suggest that larger particles have higher probability of forming particle pairs, and lower probability of forming triplets.

Panels (c) and (d) of the same figure display contours of $\Delta v^{n,-}$. For fixed separation distance r , the average inter-particle approaching velocity decreases with the wall-normal distance, which can be explained by a decreasing local shear rate: the lower the shear, the smaller shear-induced differences of the particle relative velocities. Notice also that the variations of $\Delta v^{n,-}$ with y are stronger close to the wall. The negative relative particle velocity is larger for the largest particles, case D20, over the entire flow, consistent with the scaling suggested in eq. (5.14). Finally, we report the rate-of-approach $\Delta v^{n,-}g$ in panels (e) and (f). Clearly, the differences in g discussed above induce significant differences in this quantity only close to contact. At larger separation, the behavior of $\Delta v^{n,-}g$ is dictated by $\Delta v^{n,-}$.

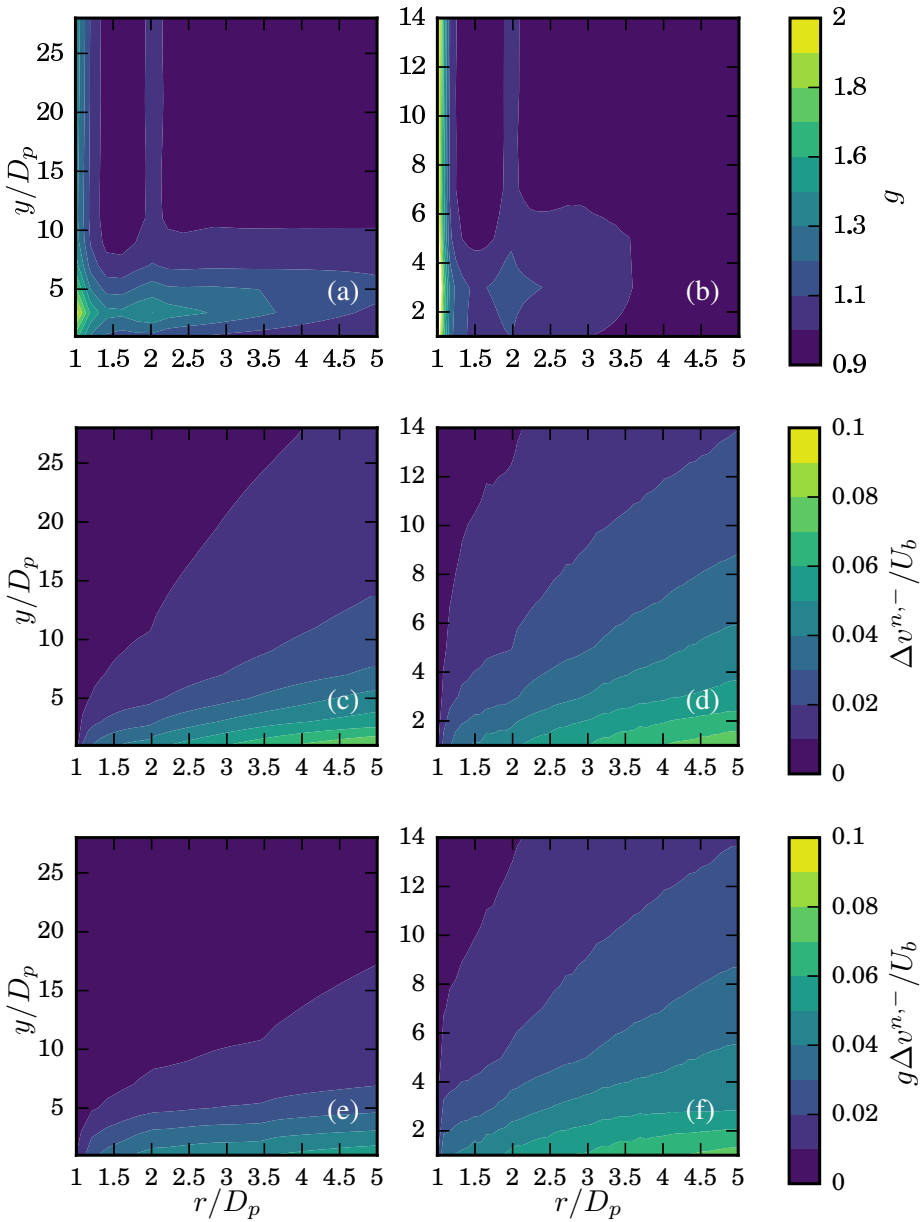


Figure 5.13: Contour plot of radial distribution function, g (top), negative relative velocity $\Delta v^{n,-}/U_b$ (middle), and rate-of-approach $g\Delta v^{n,-}/U_b$ (bottom) for simulation D10 (panels on the left: a,c,e) and D20 (panels b,d,f) as a function of the wall-normal coordinate (y) and separation (r) scaled with the particle diameter D_p .

5.4 CONCLUSIONS AND OUTLOOK

We performed interface-resolved direct numerical simulations of turbulent channel flow of suspensions of neutrally-buoyant spherical particles. Two flow cases are considered, with same Reynolds number and volume fraction, and particle size varied by a factor of 2. The simulations are compared to two single-phase reference simulations: (1) the unladen case and (2) the continuum limit of a Newtonian fluid with a viscosity corresponding to the effective viscosity of the suspension under investigation in a laminar shear flow.

As observed in [28], the main finite size effect in the zero- and first-order Eulerian statistics originate from the near-wall dynamics, in the near-wall particle layer. We show here that the larger the particles are, the further away from the wall the effects of the particle layer are significant. The near-wall inhomogeneity due to the geometrical constraints is felt at distances that scale with the particle size at fixed volume fraction, seemingly independent of the local fluid flow dynamics. This results in a smaller inner-to-outer scale separation for the flow with larger particles, clearly featured in several flow statistics.

Particles at the wall with significant particle-to-fluid slip velocity create *hot-spots* of high local wall shear (on average about 4 times larger than the mean) which contribute significantly to the mean wall-stress. These hot-spots show higher magnitude of the wall stress for small particles, which are, consistently, more localized. Their contribution to the mean wall shear is nearly the same for both particle sizes considered, about 70%. Also interesting to note is the highly increased probability of local shear stresses lower than the mean, and even negative (i.e., instantaneous flow reversal). These hot-spots change considerably the distribution of shear stresses, resulting in a pdf with wide exponential tails and rms values, $\tau_w^{rms} \approx \tau_w$, in contrast to what found in canonical single-phase wall-bounded turbulent flows, where the pdf is well fitted by a log-normal distribution and $\tau_w^{rms} \approx 0.4\tau_w$. To quantify, the probability of finding a value of the shear stress of about 2 times the total mean is negligible in the reference single-phase flow, whereas it becomes of the order of 10% in the particle-laden flows. These findings are used to derive a scaling law for the wall particle-to-fluid apparent slip velocity as a function of the flow governing parameters.

Profiles of particle Reynolds number based on the particle slip velocity present values in the bulk of $O(1)$ for the case with large particles, and very close to zero for the suspension with smaller particles. This finite particle Reynolds number for case D20 can explain the significantly larger contribution of particle stresses to the total stresses with respect to the continuum limit reference. This can be attributed to the inertial shear-thickening mechanism described in [114], where finite inertia effectively increases the particles' excluded volume.

Finite-size effects in the bulk of the flow are apparent in the second-order statistics, as shown by the profiles of the fluid velocity rms and Reynolds stresses. For these, we have tested the scaling arguments of [28] and found that accounting for the particle-wall layer is a sufficient correction for the case with smaller particles, $D_p/\delta_v \approx 10$ (in fact,

the finite size effects are relatively small in the bulk flow and using an effective viscosity only can still provide reasonable estimates). The flow with larger particles ($D_p/\delta_v \approx 20$), however, shows clear deviations from the continuum limit in the bulk of the channel also with the proposed rescaling, despite the fact that the correction for the particle-wall layer is sufficient for the lower-order statistics.

When investigating the particle dynamics, we compute statistics in wall-parallel bins of small wall-normal extent to take into account the effects of an inhomogeneous mean flow. Single-point dispersion statistics show that the spanwise particle dispersion coefficient is fairly independent of the wall-normal location, except very close to the wall. The spanwise particle dispersion is attributed to particle-turbulence interactions because of, first, the smaller diffusion coefficient near the wall and second, the larger diffusion coefficients for the smaller particles. The first effect is a consequence of the smaller spectrum of turbulence scales capable of disrupting the particle motion, whereas the second to the wider range of scales able to significantly displace the particles.

Conversely, the two-point dispersion statistics strongly depend on the wall-normal location and thus on the local shear rate. Higher shear rates induce larger relative velocities which result in faster dispersion. Even though the particles have a finite size, their dispersion statistics at short times show an exponential growth of the absolute displacement with time – as observed for point-particles with sub-Kolmogorov separation distances. The mechanism is, however, different. In this case short-range inter-particle interactions are likely the cause. Faster pair-dispersion for the larger particles is linked to the larger inter-particle interaction velocity.

Finally we investigated the particle collisional dynamics. Larger particles show higher mean values of relative velocity towards contact, consistent with the picture of shear-induced contacts. This also explains the higher probability of finding pair of larger particles at close distance. Wall-normal variations in collision probability are therefore a consequence of the variations in local shear, and thus the larger particles collide more frequently than the small particles.

In this work, we have explored the advantages of massively parallel simulations, which allow for a multi-scale, three-dimensional and time-resolved picture of a system with well-defined physical parameters. This and similar studies show that the community have reached a point when simulations of interface-resolved particle-laden flows are possible. Such simulations, yet computationally expensive, can serve as valuable tool for validation of simpler two-way coupling algorithms and perhaps Eulerian models; we believe this type of simulations will spawn several investigations aiming at better models.

6

CONCLUSIONS & FUTURE PERSPECTIVES/OUTLOOK

6.1 CONCLUSIONS

Our first objective was developing an efficient numerical algorithm for massively-parallel interface-resolved simulations of particle-laden flows. Secondly, the algorithm had to be complemented with a realistic and computationally efficient collision model for short-range particle-particle and particle-wall interactions in viscous fluids. These were the two ingredients required for achieving the main objective of this work: studying the physics of turbulent suspensions of mono-dispersed, spherical and neutrally-buoyant particles.

With data obtained from DNS we could use insights at the microscopic level for explaining the flow behavior at meso and macroscopic scales, which is typically interesting for engineering applications. Let us wrap-up our main achievements/findings in what follows.

DEVELOPMENT OF A MASSIVELY-PARALLEL NUMERICAL ALGORITHM FOR INTERFACE-RESOLVED SIMULATIONS OF PARTICLE-LADEN FLOWS

Starting point for this PhD thesis was a numerical algorithm capable of simulating up to 10 000 particles, which led to the work in [112]. Although possible, the simulation required a significant computational effort due to limitations in the (1D) Poisson solver, and memory handling in the particle treatment. For this reason the numerical code was re-written, targeting these two main problems and achieving several performance improvements along the way. The result was a memory-efficient and faster code, *InterPartS*, described in chapter 2; at this moment we can safely state that $O(10^6)$ particles can be simulated; One of the simulations presented in this thesis achieved a number of particles $N_p = 640\,000$. General features of our algorithm, worth highlighting here, are:

- 2D parallel Poisson solver, implemented with the aid of the `2dcomp&fft` routines [90]. This circumvents the restriction in terms of the number of `mpi` tasks per computational subdomain inherent to a 1D Poisson solver (the number of grid points in the wall-normal direction must be divisible by the number of tasks).
- Particle-related data is handled from the perspective of *a particle*, using FORTRAN derived types. This greatly simplifies communication of particle information between tasks.
- Efficient particle memory handling, by restricting the size of particle-related arrays to a value close to the average number of particles in each computational subdomain.
- Communication of Eulerian fluid data required for forcing made through 2-cell halo regions. This led to a major speedup and improved scalability with respect to an implementation of particle-related communication in a Lagrangian framework.
- OpenMP extension, making hybrid calculations possible, if required.

The distributed-memory parallelization performed well in terms of scalability, showing good weak and strong scaling for problem sizes of the order that we are interested in simulating (chapter 2). Moreover, the code performed well when compared to other state-of-the-art implementations for the benchmark case of decaying homogeneous isotropic turbulence laden with heavy, finite-size particles.

COLLISION MODEL FOR PARTICLE-PARTICLE AND PARTICLE-WALL INTERACTIONS

We have developed a model for short-range particle-particle and particle-wall interactions. We were interested in capturing accurately the macroscopic behavior of particle-particle and particle-wall collisions of large (i.e. non-Brownian) particles in viscous flows. In particular, for the type of flows of our interest, we were interested in accurately reproducing lubrication interactions and solid-solid contact. Moreover, we aimed at implementing a simple approach, that would not compromise the efficiency of the overall numerical algorithm. We considered an approach that could reproduce basic important physical mechanisms, though many extensions to more complex physics (such as rolling resistance, static/dynamic friction and more) are straightforward to implement.

The model combines a linear soft-sphere collision model, widely used in e.g. gas-solid or dry granular flows, ([63, 94]) with an analytical closure model for particle-particle/-wall lubrication interactions. It allows the time step of the integration of the particle motion to be stretched to a multiple of the time step of the Navier-Stokes solver. This was shown to be required in order to reproduce realistically the bouncing motion of a sphere colliding onto a wall, because the Navier-Stokes solution should be allowed to gradually relax during the sudden change in particle velocity. If not, the drag force acting on the particle is over-estimated. We validated it against several benchmark experiments, such as the bouncing motion of a sphere immersed in a viscous fluid, colliding onto a planar surface, immersed head-on particle-particle and particle-wall collisions, and oblique particle-wall collisions.

We should remark that although friction has been neglected (i.e. coefficient of sliding friction in our model $\mu_c = 0$) in our simulations of turbulent suspension flows, it can be important in dense suspensions [127], or even for achieving a stable sediment bed in a channel flow simulation with mobile particles subjected to gravity: if no wall friction force acts on the particles touching the bottom wall, the bed would slide.

TURBULENT CHANNEL TRANSPORT OF NEUTRALLY-BUOYANT PARTICLES

We performed massively-parallel state-of-the-art simulations of turbulent channel transport of neutrally-buoyant particles, in itself an achievement from a computational point of view. The focus on this case study was two-fold. First – upscaling, which led to the extension of well-known scaling laws for single-phase turbulent channel flows to a particle suspension. And second, describing finite-size effects.

In regard to the scaling laws for turbulent particle suspensions, we derived the scaling relations for the mean flow velocity and the velocity defect. From these we derived an equation capable of predicting the overall flow drag. The velocity profiles and overall drag measured from DNS showed excellent agreement with our model predictions. We note that our simulations were complemented with the ones of references [84, 112], resulting in a total of 19 DNS for which the new equation for predicting the overall flow drag was tested.

It turns out that a relatively simple model can explain the observed mesoscopic flow behavior. The key ingredient is to split the flow in two regions; a *homogeneous suspension region*, where the mean flow behavior is close to that of a Newtonian fluid with an effective suspension viscosity, and a *particle-wall layer* of particles flowing near the wall, where a discrepancy between the phases causes a deviation from this continuum limit.

The study on finite-size effects focused on a flow for fixed Reynolds number and volume fraction, a turbulent and moderately dense flow (20% solid volume fraction); the particle size was varied by a factor of two. Inspired by the findings of the study on the mean flow scaling, we investigated the dynamics of the particle-wall layer and the homogeneous suspension region. It turns out that particles flowing near the wall with high apparent slip velocity cause major changes in the pdf of wall shear stress, which is no longer described by the well-known log-normal distribution for single-phase flow. Second-order Eulerian statistics are consistent with the derived scaling laws for the mean velocity. Moreover, our results show that particle-turbulence interactions are the main causes for particle dispersion, and not particle-particle interactions. The particle collisional dynamics are driven by shear-induced particle interactions: particles with slight wall-normal offset in their position are brought together by local shear.

6.2 OUTLOOK

There are two types of recommendations for future work that should be stated here: improvements in the numerical method and its implementation, and flows that can be addressed in future research.

On the implementation side, there are a few parts of the algorithm with room for improvement. Although we do not provide solutions for all of them, it is worth pin-pointing the problems:

- Due to the way the algorithm has been implemented, particles in each task must be ordered by increasing global ID, after their positions are updated. This is needed for computing in parallel sums over the entire Lagrangian grid for a certain particle. Although a binary search algorithm is used in order to make the re-ordering more efficient, it still comprises a significant overhead. Changing the way integrals over the entire particle are calculated in parallel, such that particles do not have to be ordered, would lead to a significant improvement in computational performance.

- Improve communication of particle data for the forcing algorithm. As previously mentioned, although efficient, the communication through 2-cell halos faces a spiky downside: it does not scale down with decreasing number of particles. A more clever (which likely will be more complex) implementation, which uses solely the Eulerian points that are required for calculations, could be implemented, such that only the data needed for performing interpolation/spreading operations are communicated.
- When it comes to halo-exchange and *all-to-all* communication operations, one should explore MPI-3 routines from which memory-sharing tasks can benefit. Two tasks that need to communicate and share the same memory (e.g. corresponding to two CPUs in the same node of a supercomputer) can simply access it directly without copying it. The implementation scalability should benefit from this.

Throughout the course of this work, the developed numerical algorithm was applied to turbulent suspension flows. In parallel, and in collaboration with other researchers, it has been extended to non-spherical [3, 4] and poly-dispersed flows [86], albeit still neutrally-buoyant particles. The effect of varying the particle-to-fluid mass density ratio in a turbulent channel flow has also been studied in [48]. A natural step forward is to introduce gravity, and study in an interface-resolved sense turbulent sediment transport. This has been done in the framework of this work, and a small data base with fully-developed flows was generated, but further post-processing is required. As a teaser for a future study, figure 6.1 shows a visualization of the flow field for such a simulation.

In regard to the developed scaling laws, it would be good to measure experimentally these flows to further scrutinize the theory, and to investigate if it still holds at higher Reynolds number. Such experiments¹ are in reach of several groups. Moreover, it is also relevant to have this scaling reproduced by other groups that can simulate this flow with a different numerical method.

At the end of chapter 2, we presented the preferred type of problem for this method. Some suggestions here can broaden the range of applicability of our algorithm without compromising too much the computational efficiency (or even improving it). Interesting feature that could follow are (i) implementing the IBM in non-uniform grids while still enforcing the conservation of total force/torque acting on the particle after interpolating/spreading, as done in [70, 115], and (ii) including an added-mass-like term in the temporal integration of the particle motion to improve the stability of the numerical method for very light particles $\rho_p/\rho_f < 0.3$ [139]. The first feature would improve the computational efficiency of the algorithm when the resolution required to resolve the flow near the wall is larger than what is needed to resolve the flow around the particles. The second feature allows for studying turbulent flows with very light, rigid particles. This is relevant for

¹ Pressure drop measurements, and a methodology for measuring the mean velocity using index-matched particles and particle-image velocimetry.

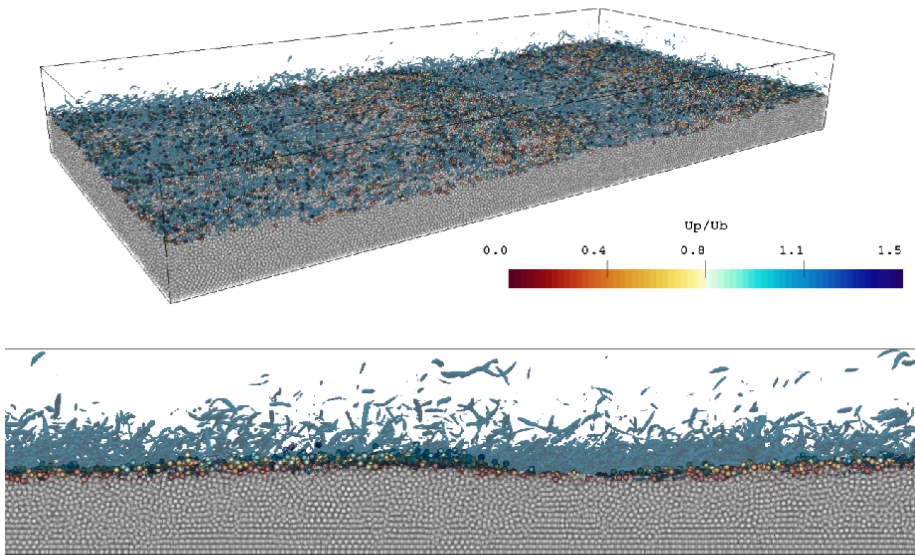


Figure 6.1: Flow visualization of an interface-resolved DNS of turbulent sediment transport. The blue iso-surfaces correspond to a constant value of the second invariant of the velocity gradient tensor Q , and particles are colored by their streamwise velocity (gray particles have zero velocity with single floating-point precision). It consists of an open-channel flow with Reynolds number based on the channel height of $Re_b = U_b h / \nu = 3\,000$, laden with 512 000 particles with density $\rho_p = 2.1\rho_f$, size $D_p/h = 1/32$ and total solid volume fraction of $\Phi = 50\%$. The average bed height corresponds to $h_b/h = 0.64$ and the friction Reynolds number estimated from the extrapolation of the Reynolds stress profile to the bed location is $Re_\tau = 357$. The flow was resolved in a computational grid with $N_x \times N_y \times N_z = 4096 \times 2048 \times 512$.

instance for spherical bubbles with surfactants, which tend to behave like a solid sphere [89].

REFERENCES

- [1] A. A. Amsden and F. H. Harlow. “A simplified MAC technique for incompressible fluid flow calculations.” In: *Journal of Computational Physics* 6.2 (1970), pp. 322–325.
- [2] A. M. Ardekani and R. H. Rangel. “Numerical investigation of particle–particle and particle–wall collisions in a viscous fluid.” In: *Journal of Fluid Mechanics* 596 (2008), pp. 437–466.
- [3] M. N. Ardekani, P. Costa, W.-P. Breugem, and L. Brandt. “Numerical study of the sedimentation of spheroidal particles.” In: *International Journal of Multiphase Flow* 87 (2016), pp. 16–34.
- [4] M. N. Ardekani, P. Costa, W.-P. Breugem, F. Picano, and L. Brandt. “Drag reduction in turbulent channel flow laden with finite-size oblate spheroids.” In: *Journal of Fluid Mechanics* 816 (2017), pp. 43–70.
- [5] R. A. Bagnold. “Experiments on a gravity-free dispersion of large solid spheres in a Newtonian fluid under shear.” In: *Proceedings of the Royal Society of London A: Mathematical, Physical and Engineering Sciences*. Vol. 225. 1160. The Royal Society. 1954, pp. 49–63.
- [6] S. Balachandar and J. K. Eaton. “Turbulent Dispersed Multiphase Flow.” In: *Annual Review of Fluid Mechanics* 42.1 (2010), pp. 111–133.
- [7] S. Balachandar and J. K. Eaton. “Turbulent dispersed multiphase flow.” In: *Annual Review of Fluid Mechanics* 42 (2010), pp. 111–133.
- [8] G. Barnocky and R. H. Davis. “Elastohydrodynamic collision and rebound of spheres: Experimental verification.” In: *Physics of Fluids* 31 (1988), p. 1324.
- [9] A. B. Basset. *A treatise on hydrodynamics: with numerous examples*. Vol. 2. Deighton, Bell and Company, 1888.
- [10] G. K. Batchelor. “The effect of homogeneous turbulence on material lines and surfaces.” In: *Proceedings of the Royal Society of London A: Mathematical, Physical and Engineering Sciences*. Vol. 213. 1114. The Royal Society. 1952, pp. 349–366.
- [11] G. K. Batchelor. “The stress system in a suspension of force-free particles.” In: *Journal of Fluid Mechanics* 41.03 (1970), pp. 545–570.
- [12] G. K. Batchelor and A. A. Townsend. “Decay of turbulence in the final period.” In: *Proceedings of the Royal Society of London A: Mathematical, Physical and Engineering Sciences*. Vol. 194. 1039. The Royal Society. 1948, pp. 527–543.

- [13] F. Blanc, E. Lemaire, A. Meunier, and F. Peters. “Microstructure in sheared non-Brownian concentrated suspensions.” In: *Journal of Rheology* 57.1 (2013), pp. 273–292.
- [14] J. F. Brady and G. Bossis. “Stokesian dynamics.” In: *Annual Review of Fluid Mechanics* 20 (1988), pp. 111–157.
- [15] L. Brendel and S. Dippel. “Lasting contacts in molecular dynamics simulations.” In: *NATO ASI Series E Applied Sciences-Advanced Study Institute* 350 (1998), pp. 313–318.
- [16] H. Brenner. “The slow motion of a sphere through a viscous fluid towards a plane surface.” In: *Chemical Engineering Science* 16.3 (1961), pp. 242–251.
- [17] W.-P. Breugem. “A combined soft-sphere collision/immersed boundary method for resolved simulations of particulate flows.” In: *ASME 2010 3rd Joint US-European Fluids Engineering Summer Meeting collocated with 8th International Conference on Nanochannels, Microchannels, and Minichannels*. American Society of Mechanical Engineers. 2010, pp. 2381–2392.
- [18] W.-P. Breugem. “A second-order accurate immersed boundary method for fully resolved simulations of particle-laden flows.” In: *Journal of Computational Physics* 231.13 (2012), pp. 4469–4498. ISSN: 0021-9991.
- [19] E. Brown and H. M. Jaeger. “Shear thickening in concentrated suspensions: phenomenology, mechanisms and relations to jamming.” In: *Reports on Progress in Physics* 77.4 (2014), p. 046602.
- [20] T. M. Burton and J. K. Eaton. “Fully resolved simulations of particle-turbulence interaction.” In: *Journal of Fluid Mechanics* 545 (2005), pp. 67–111.
- [21] E. Calzavarini, R. Volk, M. Bourgoïn, E. L  v  que, J.-F. Pinton, and F. Toschi. “Acceleration statistics of finite-sized particles in turbulent flow: the role of Fax  n forces.” In: *Journal of Fluid Mechanics* 630 (2009), pp. 179–189.
- [22] J. Capecelatro and O. Desjardins. “An Euler–Lagrange strategy for simulating particle-laden flows.” In: *Journal of Computational Physics* 238 (2013), pp. 1–31.
- [23] S. Chen and G. D. Doolen. “Lattice Boltzmann method for fluid flows.” In: *Annual Review of Fluid Mechanics* 30.1 (1998), pp. 329–364.
- [24] A. Chouippe and M. Uhlmann. “Forcing homogeneous turbulence in direct numerical simulation of particulate flow with interface resolution and gravity.” In: *Physics of Fluids (1994-present)* 27.12 (2015), p. 123301.
- [25] M. Cisse, H. Homann, and J. Bec. “Slipping motion of large neutrally buoyant particles in turbulence.” In: *Journal of Fluid Mechanics* 735 (2013), R1.

- [26] M. D. A. Cooley and M. E. O'Neill. "On the slow motion generated in a viscous fluid by the approach of a sphere to a plane wall or stationary sphere." In: *Mathematika* 16.1 (1969), pp. 37–49.
- [27] P. Costa, B. J. Boersma, J. Westerweel, and W.-P. Breugem. "Collision model for fully resolved simulations of flows laden with finite-size particles." In: *Phys. Rev. E* 92 (5 Nov. 2015), p. 053012.
- [28] P. Costa, F. Picano, L. Brandt, and W.-P. Breugem. "Universal Scaling Laws for Dense Particle Suspensions in Turbulent Wall-Bounded Flows." In: *Physical Review Letters* 117 (13 Sept. 2016), p. 134501.
- [29] P. Costa, F. Picano, L. Brandt, and W.-P. Breugem. "Finite size effects in dense turbulent wall-bounded transport of neutrally-buoyant spheres." In: *Journal of Fluid Mechanics (under review)* (2017).
- [30] C. T. Crowe, M. P. Sharma, and David E. Stock. "The particle-source-in cell (PSI-CELL) model for gas-droplet flows." In: *Journal of Fluids Engineering* 99.2 (1977), pp. 325–332.
- [31] P. A. Cundall and O. D. L. Strack. "A discrete numerical model for granular assemblies." In: *Geotechnique* 29.1 (1979), pp. 47–65.
- [32] S. L. Dance and M. R. Maxey. "Incorporation of lubrication effects into the force-coupling method for particulate two-phase flow." In: *Journal of Computational Physics* 189.1 (July 2003), pp. 212–238.
- [33] R. H. Davis, J.-M. Serayssol, and E. J. Hinch. "Elastohydrodynamic collision of two spheres." In: *Journal of Fluid Mechanics* 163 (1986), pp. 479–97.
- [34] R. B. Dean. "Reynolds number dependence of skin friction and other bulk flow variables in two-dimensional rectangular duct flow." In: *Journal of Fluids Engineering* 100.2 (1978), pp. 215–223.
- [35] N. G. Deen, M. Van Sint Annaland, M. A. van der Hoef, and J. A. M. Kuipers. "Review of discrete particle modeling of fluidized beds." In: *Chemical Engineering Science* 62.1-2 (Jan. 2007), pp. 28–44.
- [36] J. J. Derksen. "Highly resolved simulations of solids suspension in a small mixing tank." In: *AIChE Journal* 58.10 (2012), pp. 3266–3278.
- [37] J. J. Derksen. "Simulations of granular bed erosion due to a mildly turbulent shear flow." In: *Journal of Hydraulic Research* 53.5 (2015), pp. 622–632.
- [38] J. K. Eaton and J. R. Fessler. "Preferential concentration of particles by turbulence." In: *International Journal of Multiphase Flow* 20 (1994), pp. 169–209.
- [39] A. Einstein. "Über die von der molekularkinetischen Theorie der Wärme geforderte Bewegung von in ruhenden Flüssigkeiten suspendierten Teilchen." In: *Annalen der Physik* 322.8 (1905), pp. 549–560.

- [40] A. Einstein. “On the theory of the Brownian movement.” In: *Annalen der Physik* 4.19 (1906), pp. 371–381.
- [41] S. Elghobashi. “On predicting particle-laden turbulent flows.” In: *Applied Scientific Research* 52.4 (1994), pp. 309–329.
- [42] H. Enwald, E. Peirano, and A.-E. Almstedt. “Eulerian two-phase flow theory applied to fluidization.” In: *International Journal of Multiphase Flow* 22 (1996), pp. 21–66.
- [43] E. A. Fadlun, R. Verzicco, P. Orlandi, and J. Mohd-Yusof. “Combined immersed-boundary finite-difference methods for three-dimensional complex flow simulations.” In: *Journal of Computational Physics* 161.1 (2000), pp. 35–60.
- [44] Z.-G. Feng, E. E. Michaelides, and S. Mao. “A Three-Dimensional Resolved Discrete Particle Method for Studying Particle-Wall Collision in a Viscous Fluid.” In: *Journal of Fluids Engineering* 132.9 (2010), p. 091302.
- [45] J. R. Fessler, J. D. Kulick, and J. K. Eaton. “Preferential concentration of heavy particles in a turbulent channel flow.” In: *Physics of Fluids (1994-present)* 6.11 (1994), pp. 3742–3749.
- [46] S. F. Foerster, M. Y. Louge, H. Chang, and K. Allia. “Measurements of the collision properties of small spheres.” In: *Physics of Fluids* 6.3 (1994), p. 1108.
- [47] W. Fornari, F. Picano, and L. Brandt. “Sedimentation of finite-size spheres in quiescent and turbulent environments.” In: *Journal of Fluid Mechanics* 788 (2016), pp. 640–669.
- [48] W. Fornari, A. Formenti, F. Picano, and L. Brandt. “The effect of particle density in turbulent channel flow laden with finite size particles in semi-dilute conditions.” In: *Physics of Fluids* 28.3 (2016).
- [49] Message Passing Interface Forum. *MPI: A Message-Passing Interface Standard*. English. Version Version 3.1. Message Passing Interface Forum. June 2015.
- [50] R. O. Fox. “Large-eddy-simulation tools for multiphase flows.” In: *Annual Review of Fluid Mechanics* 44 (2012), pp. 47–76.
- [51] R. Gatignol. “The Faxén formulas for a rigid particle in an unsteady non-uniform Stokes-flow.” In: *Journal de Mécanique théorique et appliquée* 2.2 (1983), pp. 143–160.
- [52] R. Glowinski, T.-W. Pan, T. I. Hesla, and D. D. Joseph. “A distributed Lagrange multiplier/fictitious domain method for particulate flows.” In: *International Journal of Multiphase Flow* 25.5 (1999), pp. 755–794.
- [53] G. H. Golub and C. F. Van Loan. *Matrix Computations*. Vol. 3. JHU Press, 2012.
- [54] P. Gondret, M. Lance, and L. Petit. “Bouncing motion of spherical particles in fluids.” In: *Physics of Fluids* 14 (2002), p. 643.

- [55] D. Grasso, K. Subramaniam, M. Butkus, K. Strevett, and J. Bergendahl. “A review of non-DLVO interactions in environmental colloidal systems.” In: *Reviews in Environmental Science and Biotechnology* 1.1 (2002), pp. 17–38.
- [56] T. Gröger, U. Tüzün, and David M. Heyes. “Modelling and measuring of cohesion in wet granular materials.” In: *Powder Technology* 133.1 (2003), pp. 203–215.
- [57] P. Gualtieri, F. Picano, G. Sardina, and C. M. Casciola. “Exact regularized point particle method for multiphase flows in the two-way coupling regime.” In: *Journal of Fluid Mechanics* 773 (2015), pp. 520–561.
- [58] E. Guazzelli and J. F. Morris. *A physical introduction to suspension dynamics*. Vol. 45. Cambridge University Press, 2011.
- [59] R. E. Hampton, A. A. Mammoli, A. L. Graham, N. Tetlow, and S. A. Altobelli. “Migration of particles undergoing pressure-driven flow in a circular conduit.” In: *Journal of Rheology* 41.3 (1997), pp. 621–640.
- [60] J. B. Herbich. *Handbook of dredging engineering*. McGraw-Hill Companies, 1992.
- [61] H. Hertz. “Ueber die Berührung fester elastischer Körper.” In: *Journal für die reine und angewandte Mathematik* 92 (1882), pp. 156–171.
- [62] J. O. Hinze. *Turbulence*. Vol. 218. McGraw-Hill classic textbook reissue series. McGraw-Hill, 1975.
- [63] M. A. van der Hoef, M. Van Sint Annaland, and J. A. M. Kuipers. “Computational fluid dynamics for dense gas–solid fluidized beds: a multi-scale modeling strategy.” In: *Chemical Engineering Science* 59.22 (2004), pp. 5157–5165.
- [64] H. H. Hu. “Direct simulation of flows of solid-liquid mixtures.” In: *International Journal of Multiphase Flow* 22.2 (1996), pp. 335–352.
- [65] H. H. Hu, N. A. Patankar, and M. Y. Zhu. “Direct numerical simulations of fluid–solid systems using the arbitrary Lagrangian–Eulerian technique.” In: *Journal of Computational Physics* 169.2 (2001), pp. 427–462.
- [66] J. C. R. Hunt, A. A. Wray, and P. Moin. “Eddies, streams, and convergence zones in turbulent flows.” In: (1988).
- [67] M. L. Hunt, R. Zenit, C. S. Campbell, and C. E. Brennen. “Revisiting the 1954 suspension experiments of RA Bagnold.” In: *Journal of Fluid Mechanics* 452 (2002), pp. 1–24.
- [68] E. Izard, T. Bonometti, and L. Lacaze. “Modelling the dynamics of a sphere approaching and bouncing on a wall in a viscous fluid.” In: *Journal of Fluid Mechanics* 747 (2014), pp. 422–446.
- [69] P. S. Jackson. “On the displacement height in the logarithmic velocity profile.” In: *Journal of Fluid Mechanics* 111 (Oct. 1981), pp. 15–25. ISSN: 1469-7645.

- [70] J. Jang and C. Lee. “An immersed boundary method for nonuniform grids.” In: *Journal of Computational Physics* (2017).
- [71] D. J. Jeffrey. “Low-Reynolds-number flow between converging spheres.” In: *Mathematika* 29 (1982), pp. 58–66.
- [72] A. A. Johnson and T. E. Tezduyar. “Simulation of multiple spheres falling in a liquid-filled tube.” In: *Computer Methods in Applied Mechanics and Engineering* 134.3-4 (1996), pp. 351–373.
- [73] G. G. Joseph and M. L. Hunt. “Oblique particle–wall collisions in a liquid.” In: *Journal of Fluid Mechanics* 510.1 (2004), pp. 71–93.
- [74] G. G. Joseph, R. Zenit, M. L. Hunt, and A. M. Rosenwinkel. “Particle-wall collisions in a viscous fluid.” In: *Journal of Fluid Mechanics* 433 (2001), pp. 329–346.
- [75] T. von Kármán. “von: Mechanische Ähnlichkeit und Turbulenz. Nachr. Ges. Wiss. Göttingen, math.-phys. Kl.(1930) 58–76.” In: *Proc. 3. Int. Cong. Appl. Mech* (1930), pp. 322–346.
- [76] T. Kempe and J. Fröhlich. “An improved immersed boundary method with direct forcing for the simulation of particle laden flows.” In: *Journal of Computational Physics* 231.9 (2012), pp. 3663–3684.
- [77] T. Kempe and J. Fröhlich. “Collision modelling for the interface-resolved simulation of spherical particles in viscous fluids.” In: *Journal of Fluid Mechanics* 709 (2012), pp. 445–489.
- [78] A. G. Kidanemariam and M. Uhlmann. “Direct numerical simulation of pattern formation in subaqueous sediment.” In: *Journal of Fluid Mechanics* 750 (2014), R2.
- [79] A. G. Kidanemariam and M. Uhlmann. “Interface-resolved direct numerical simulation of the erosion of a sediment bed sheared by laminar channel flow.” In: *International Journal of Multiphase Flow* 67 (2014), pp. 174–188.
- [80] J. Kim, P. Moin, and R. Moser. “Turbulence statistics in fully developed channel flow at low Reynolds number.” In: *Journal of Fluid Mechanics* 177 (1987), pp. 133–166.
- [81] S. Kim and S. J. Karrila. *Microhydrodynamics: principles and selected applications*. Courier Corporation, 2013.
- [82] A. N. Kolmogorov. “The local structure of turbulence in incompressible viscous fluid for very large Reynolds numbers.” In: *Dokl. Akad. Nauk SSSR*. Vol. 30. 4. JSTOR. 1941, pp. 301–305.

- [83] R. A. Lambert, F. Picano, W.-P. Breugem, and L. Brandt. “Active suspensions in thin films: nutrient uptake and swimmer motion.” In: *Journal of Fluid Mechanics* 733 (Oct. 2013), pp. 528–557. ISSN: 1469-7645.
- [84] I. Lashgari, F. Picano, W.-P. Breugem, and L. Brandt. “Laminar, Turbulent, and Inertial Shear-Thickening Regimes in Channel Flow of Neutrally Buoyant Particle Suspensions.” In: *Physical Review Letters* 113 (25 2014), p. 254502.
- [85] I. Lashgari, F. Picano, W.-P. Breugem, and L. Brandt. “Channel flow of rigid sphere suspensions: Particle dynamics in the inertial regime.” In: *International Journal of Multiphase Flow* 78 (2016), pp. 12–24. ISSN: 0301-9322.
- [86] I. Lashgari, F. Picano, P. Costa, W.-P. Breugem, and L. Brandt. “Turbulent channel flow of a dense binary mixture of rigid particles.” In: *Journal of Fluid Mechanics* 818 (2017), pp. 623–645.
- [87] D. Legendre, R. Zenit, C. Daniel, and P. Guiraud. “A note on the modelling of the bouncing of spherical drops or solid spheres on a wall in viscous fluid.” In: *Chemical Engineering Science* 61.11 (2006), pp. 3543–3549.
- [88] D. Leighton and A. Acrivos. “The shear-induced migration of particles in concentrated suspensions.” In: *Journal of Fluid Mechanics* 181 (1987), pp. 415–439.
- [89] V. G. Levich. *Physicochemical hydrodynamics*. Prentice hall, 1962.
- [90] N. Li and S. Laizet. “2DECOMP & FFT-a highly scalable 2d decomposition library and FFT interface.” In: *Cray User Group 2010 conference*. 2010, pp. 1–13.
- [91] X. Li, M. L. Hunt, and T. Colonius. “A contact model for normal immersed collisions between a particle and a wall.” In: *Journal of Fluid Mechanics* 691 (Dec. 2011), pp. 123–145.
- [92] V. Loisel, M. Abbas, O. Masbernat, and E. Climent. “The effect of neutrally buoyant finite-size particles on channel flows in the laminar-turbulent transition regime.” In: *Physics of Fluids* 25.12 (2013), p. 123304.
- [93] F. Lucci, A. Ferrante, and S. Elghobashi. “Modulation of isotropic turbulence by particles of Taylor length-scale size.” In: *Journal of Fluid Mechanics* 650 (2010), pp. 5–55.
- [94] S. Luding. “Introduction to discrete element methods: Basic of contact force models and how to perform the micro-macro transition to continuum theory.” In: *European Journal of Environmental and Civil Engineering* 12.7-8 (2008), pp. 785–826.
- [95] K. Luo, Z. Wang, J. Fan, and K. Cen. “Full-scale solutions to particle-laden flows: Multidirect forcing and immersed boundary method.” In: *Physical Review E* 76.6 (2007), p. 066709.

- [96] M. Marchioro, M. Tanksley, and A. Prosperetti. “Mixture pressure and stress in disperse two-phase flow.” In: *International journal of multiphase flow* 25.6 (1999), pp. 1395–1429.
- [97] J.-P. Matas, J. F. Morris, and É. Guazzelli. “Transition to Turbulence in Particulate Pipe Flow.” In: *Physical Review Letters* 90 (1 2003), p. 014501.
- [98] N. Maw, J. R. Barber, and J. N. Fawcett. “The oblique impact of elastic spheres.” In: *Wear* 38.1 (1976), pp. 101–114.
- [99] M. R. Maxey. “Simulation Methods for Particulate Flows and Concentrated Suspensions.” In: *Annual Review of Fluid Mechanics* 49 (2017), pp. 171–193.
- [100] M. R. Maxey and J. J. Riley. “Equation of motion for a small rigid sphere in a nonuniform flow.” In: *Physics of Fluids (1958-1988)* 26.4 (1983), pp. 883–889.
- [101] J.-P. Minier and E. Peirano. “The pdf approach to turbulent polydispersed two-phase flows.” In: *Physics reports* 352.1 (2001), pp. 1–214.
- [102] R. Mittal and G. Iaccarino. “Immersed Boundary Methods.” In: *Annual Review of Fluid Mechanics* 37.1 (Jan. 2005), pp. 239–261.
- [103] J. J. Monaghan. “Smoothed particle hydrodynamics and its diverse applications.” In: *Annual Review of Fluid Mechanics* 44 (2012), pp. 323–346.
- [104] G. E. Moore et al. “Cramming more components onto integrated circuits.” In: *Proceedings of the IEEE* 86.1 (1998), pp. 82–85.
- [105] J. F. Morris. “A review of microstructure in concentrated suspensions and its implications for rheology and bulk flow.” In: *Rheologica Acta* 48.8 (2009), pp. 909–923.
- [106] J. C. B. de Motta, W.-P. Breugem, B. Gazanion, J.-L. Estivalezes, S. Vincent, and E. Climent. “Numerical modelling of finite-size particle collisions in a viscous fluid.” In: *Physics of Fluids* 25.8 (2013), pp. 083302–083302–9.
- [107] J. C. B. de Motta, J.-L. Estivalezes, E. Climent, and S. Vincent. “Local dissipation properties and collision dynamics in a sustained homogeneous turbulent suspension composed of finite size particles.” In: *International Journal of Multiphase Flow* 85 (2016), pp. 369–379.
- [108] J. Brändle de Motta et al. “Assessment of methods for fully resolved simulations of particle-laden turbulent flows.” In: (*in preparation*) (2017).
- [109] R. Örlü and P. Schlatter. “On the fluctuating wall-shear stress in zero pressure-gradient turbulent boundary layer flows.” In: *Physics of Fluids* 23.2 (2011), p. 021704.
- [110] N. A. Patankar, P. Singh, D. D. Joseph, R. Glowinski, and T.-W. Pan. “A new formulation of the distributed Lagrange multiplier/fictitious domain method for particulate flows.” In: *International Journal of Multiphase Flow* 26.9 (2000), pp. 1509–1524.

- [111] V. C. Patel, W. Rodi, and G. Scheuerer. “Turbulence models for near-wall and low Reynolds number flows—a review.” In: *AIAA J.* 23.9 (1985), pp. 1308–1319.
- [112] F. Picano, W.-P. Breugem, and L. Brandt. “Turbulent channel flow of dense suspensions of neutrally buoyant spheres.” In: *Journal of Fluid Mechanics* 764 (Feb. 2015), pp. 463–487. ISSN: 1469-7645.
- [113] F. Picano, G. Sardina, P. Gualtieri, and C. M. Casciola. “Anomalous memory effects on transport of inertial particles in turbulent jets.” In: *Physics of Fluids* 22.5 (2010), p. 051705.
- [114] F. Picano, W.-P. Breugem, D. Mitra, and L. Brandt. “Shear Thickening in Non-Brownian Suspensions: An Excluded Volume Effect.” In: *Physical Review Letters* 111 (9 2013), p. 098302.
- [115] A. Pinelli, I. Z. Naqavi, U. Piomelli, and J. Favier. “Immersed-boundary methods for general finite-difference and finite-volume Navier–Stokes solvers.” In: *Journal of Computational Physics* 229.24 (2010), pp. 9073–9091.
- [116] S. B. Pope. *Turbulent Flows*. IOP Publishing, 2001.
- [117] C. Pozrikidis. *Boundary integral and singularity methods for linearized viscous flow*. Cambridge University Press, 1992.
- [118] A. Prosperetti. “Life and death by boundary conditions.” In: *Journal of Fluid Mechanics* 768 (Apr. 2015), pp. 1–4. ISSN: 1469-7645.
- [119] A. Prosperetti and H. N. Oguz. “Physalis: a new $O(N)$ method for the numerical simulation of disperse systems: potential flow of spheres.” In: *Journal of Computational Physics* 167.1 (2001), pp. 196–216.
- [120] M. W. Reeks. “On the dispersion of small particles suspended in an isotropic turbulent fluid.” In: *Journal of Fluid Mechanics* 83.03 (1977), pp. 529–546.
- [121] J.B. Ritz and J.P. Caltagirone. “A numerical continuous model for the hydrodynamics of fluid particle systems.” In: *International Journal for Numerical Methods in Fluids* 30.8 (1999), pp. 1067–1090.
- [122] I. Roghair, Y. M. Lau, N. G. Deen, H. M. Slagter, M. W. Baltussen, M. v S. Annaland, and J. A. M. Kuipers. “On the drag force of bubbles in bubble swarms at intermediate and high Reynolds numbers.” In: *Chemical Engineering Science* 66.14 (2011), pp. 3204–3211.
- [123] A. M. Roma, C. S. Peskin, and M. J. Berger. “An adaptive version of the immersed boundary method.” In: *Journal of Computational Physics* 153.2 (1999), pp. 509–534.
- [124] J. P. L. C. Salazar and L. R. Collins. “Two-particle dispersion in isotropic turbulent flows.” In: *Annual Review of Fluid Mechanics* 41 (2009), pp. 405–432.

- [125] G. Sardina, P. Schlatter, L. Brandt, F. Picano, and C. M. Casciola. “Wall accumulation and spatial localization in particle-laden wall flows.” In: *Journal of Fluid Mechanics* 699 (2012), pp. 50–78.
- [126] U. Schumann and R. A. Sweet. “Fast Fourier transforms for direct solution of Poisson’s equation with staggered boundary conditions.” In: *Journal of Computational Physics* 75.1 (1988), pp. 123–137.
- [127] R. Seto, R. Mari, J. F. Morris, and M. M. Denn. “Discontinuous shear thickening of frictional hard-sphere suspensions.” In: *Physical Review Letters* 111.21 (2013), p. 218301.
- [128] A. J. Sierakowski and A. Prosperetti. “Resolved-particle simulation by the Physalis method: Enhancements and new capabilities.” In: *Journal of Computational Physics* 309 (2016), pp. 164–184.
- [129] A. Sierou and J. F. Brady. “Shear-induced self-diffusion in non-colloidal suspensions.” In: *Journal of Fluid Mechanics* 506.1 (2004), pp. 285–314.
- [130] J. A. Simeonov and J. Calantoni. “Modeling mechanical contact and lubrication in Direct Numerical Simulations of colliding particles.” In: *International Journal of Multiphase Flow* 46 (Nov. 2012), pp. 38–53.
- [131] A. J. Smits, B. J. McKeon, and I. Marusic. “High-Reynolds Number Wall Turbulence.” In: *Annual Review of Fluid Mechanics* 43.1 (2011), pp. 353–375.
- [132] A. Soldati and C. Marchioli. “Physics and modelling of turbulent particle deposition and entrainment: Review of a systematic study.” In: *International Journal of Multiphase Flow* 35.9 (2009), pp. 827–839.
- [133] J. J. Stickel and R. L. Powell. “Fluid Mechanics And Rheology of Dense Suspensions.” In: *Annual Review of Fluid Mechanics* 37.1 (2005), pp. 129–149.
- [134] S. Takagi, H. N. Oguz, Z. Zhang, and A. Prosperetti. “PHYSALIS: A new method for particle simulation: Part II: Two-dimensional Navier–Stokes flow around cylinders.” In: *Journal of Computational Physics* 187.2 (2003), pp. 371–390.
- [135] A. Ten Cate, C. H. Nieuwstad, J. J. Derksen, and H. E. A. Van den Akker. “Particle imaging velocimetry experiments and lattice-Boltzmann simulations on a single sphere settling under gravity.” In: *Physics of Fluids* 14.11 (2002), pp. 4012–4025.
- [136] A. Ten Cate, J. J. Derksen, L. M. Portela, and H. E. A. Van Den Akker. “Fully resolved simulations of colliding monodisperse spheres in forced isotropic turbulence.” In: *Journal of Fluid Mechanics* 519 (2004), pp. 233–271.
- [137] A. Ten Cate, J. J. Derksen, L. M. Portela, and H. E. A. Van Den Akker. “Fully resolved simulations of colliding monodisperse spheres in forced isotropic turbulence.” In: *Journal of Fluid Mechanics* 519 (2004), pp. 233–271.

- [138] F. Toschi and E. Bodenschatz. “Lagrangian properties of particles in turbulence.” In: *Annual Review of Fluid Mechanics* 41 (2009), pp. 375–404.
- [139] S. Tschisgale, T. Kempe, and J. Fröhlich. “A non-iterative immersed boundary method for spherical particles of arbitrary density ratio.” In: *Journal of Computational Physics* (2017).
- [140] Y. Tsuji, T. Kawaguchi, and T. Tanaka. “Discrete particle simulation of two-dimensional fluidized bed.” In: *Powder Technology* 77.1 (1993), pp. 79–87.
- [141] M. Uhlmann. *Simulation of particulate flows on multi-processor machines with distributed memory*. Ciemat, 2004.
- [142] M. Uhlmann. “An immersed boundary method with direct forcing for the simulation of particulate flows.” In: *Journal of Computational Physics* 209.2 (2005), pp. 448–476.
- [143] M. Uhlmann. “Interface-resolved direct numerical simulation of vertical particulate channel flow in the turbulent regime.” In: *Physics of Fluids (1994-present)* 20.5 (2008), p. 053305.
- [144] S. Vincent, J. C. B. de Motta, A. Sarthou, J.-L. Estivaleres, O. Simonin, and E. Climent. “A Lagrangian VOF tensorial penalty method for the DNS of resolved particle-laden flows.” In: *Journal of Computational Physics* 256 (2014), pp. 582–614.
- [145] B. Vowinckel, T. Kempe, and J. Fröhlich. “Fluid–particle interaction in turbulent open channel flow with fully-resolved mobile beds.” In: *Advances in Water Resources* 72 (2014), pp. 32–44.
- [146] A. W. Vreman. “Particle-resolved direct numerical simulation of homogeneous isotropic turbulence modified by small fixed spheres.” In: *Journal of Fluid Mechanics* 796 (2016), pp. 40–85.
- [147] A. W. Vreman. “A staggered overset grid method for resolved simulation of incompressible flow around moving spheres.” In: *Journal of Computational Physics* 333 (2017), pp. 269–296.
- [148] O. R. Walton. “Numerical simulation of inelastic, frictional particle-particle interactions.” In: *Particulate two-phase flow* 25 (1993), pp. 884–911.
- [149] L.-P. Wang, C. Peng, Z. Guo, and Z. Yu. “Flow Modulation by Finite-Size Neutrally Buoyant Particles in a Turbulent Channel Flow.” In: *Journal of Fluids Engineering* 138.4 (2016), p. 041306.
- [150] P. Wesseling. *Principles of Computational Fluid Dynamics*. Vol. 29. Springer Science & Business Media, 2009.
- [151] F.-L. Yang and M. L. Hunt. “Dynamics of particle-particle collisions in a viscous liquid.” In: *Physics of Fluids* 18 (2006), p. 121506.

- [152] K. Yeo and M. R. Maxey. “Numerical simulations of concentrated suspensions of monodisperse particles in a Poiseuille flow.” In: *Journal of Fluid Mechanics* 682 (Sept. 2011), pp. 491–518. issn: 1469-7645.
- [153] W. Yu, I. Vinkovic, and M. Buffat. “Finite-size particles in turbulent channel flow: quadrant analysis and acceleration statistics.” In: *Journal of Turbulence* 17.11 (2016), pp. 1048–1071.
- [154] Z. Zhang and A. Prosperetti. “A second-order method for three-dimensional particle simulation.” In: *Journal of Computational Physics* 210.1 (2005), pp. 292–324.
- [155] Q. Zhou and L.-S. Fan. “A second-order accurate immersed boundary-lattice Boltzmann method for particle-laden flows.” In: *Journal of Computational Physics* 268 (2014), pp. 269–301.

ACKNOWLEDGMENTS

Surely I would not have reached this point without the friendship and support of many. In a way, this thesis was written a bit by you, and a bit for you.

The first words of gratitude go to Wim-Paul Breugem, my daily supervisor. Thank you for your guidance and giving me the freedom to find my way around this project. Your creativity and analytical precision were very important for the success of this work. A great example is the equation for the overall flow drag (eq. 5.3), derived by you when the PRL draft was mostly ready. Without modification, it matched the DNS data, tied the PRL together, kicking eq. 5.4 to supplemental material. Here we are, after so many discussions, leading to several consensuses (sometimes consensus in our disagreements!). Thanks again!

I would like to thank my promotors, Bendiks Jan Boermsa and Jerry Westerweel, who whenever needed gave some good, inspiring advise. Bendiks Jan, thank you for the very solid tips when it comes to high performance computing, without which getting the PRACE grant awarded would have been extremely hard. Not all professors, presidents of a department, show immediate availability to profile the FORTRAN code of a PhD student! Jerry, our discussions were more centered on the flow physics and academia in general. Muito obrigado pelos sólidos e inspiradores conselhos!

Around half-way of my PhD, I had the opportunity of collaborating closely with Luca Brandt from KTH Mechanics in Stockholm, and Francesco Picano from Padova University. Our collaboration lead to a set of works that speaks for itself. Thanks Luca and Francesco for the nice discussions and ambitious goals that pushed the work further. I extend my gratitude to the PhD students at KTH with whom I closely worked, Mehdi Ni-azi Ardekani, Iman Lashgari and Walter Fornari. Being the only PhD student ‘working on particles’ in our lab in Delft, our few discussions were quite stimulating. Thanks also to the other people at KTH which made my 2-week work visit very pleasant!

Thank you Jorge Motta from CORIA, France and Jos Derksen from Aberdeen, UK, for the collaboration in the workshop *High Performance Computations for Fluid Dynamics Interface treatment and finite size particles – Interface treatment and finite size particles* held in November 2014 in Toulouse. Thanks also to all the organizers, in particular Nicolas Renon for the support with the EOS supercomputer.

Thank you Yacine Ould-Rouis, from Maison de la Simulacion, in Saclay, France for fruitful discussions and hands-on actions that lead to a great improvement in the DNS code performance.

Throughout the course of my PhD I was fortunate enough to run simulations on five different supercomputers. I would like to acknowledge in particular the computing time provided by SURFSARA, in the Dutch national supercomputer Cartesius; CURIE CEA

(Paris) under the PRACE grant SEDTRANS and the PDC Center for High Performance Computing at KTH (Stockholm) for the computing time.

The working environment at the lab is awesome. An awesomeness report would lead to another book, likely with more pages. Thank you Gosse, Jerke, Greta, Ankur, Pepijn, Norbert, Sedat, Mike, Melika, Arati, Daniele, Mark Franken, Andries, Maurice, Arnoud, Yoshi, Ernst Jan, Mark Tummers, Ruud, René Delfos, Mathieu, Caroline, Ria, Rob, Willem, Manu, Marieke, Sita, Jasper Tomas, Jasper Ruijok, Koen, Gijis, Elert, Christian Potma, Christian Poelma, Daniel Tam, Gerrit, Gem, Soeren, Ema, Saad, Florian, René van Hout, Gerben, Mohamed, Yuk Man, Göktürk, Ozge, Dries, Henk, Manu, Edwin and Jan for making it so! Thank you *GoT* group, together with Daniele and Greta for hours of entertainment; Henk, one of the few numericist specimen in the lab, for many pleasant discussions; Manu for the great help in adjusting me smoothly in the lab; Caroline for the administrative and lunch box support; and Arnoud for being such a great company at the office since day one! Also, thank you Lyckle Drost and Sander de With for the stimulating discussions while working together on your Master Thesis project.

To all the amazing friends I made in Delft, thank you. In particular my best friends Boris, Eduardo and Alexis. Two of you shall be my paranymphs.

Thanks Carlos da Silva, Mário Costa and Pedro Coelho, for encouraging and helping me to make the start of my PhD project in Delft possible. Aos meus queridos amigos, com quem aprendi a trabalhar ‘sempre no arame’: Alex, Fred, Mósca, Caio, Ramos, António, Miguel, David, Adriano, Nuno Gil, Hugo, Marco, Gaspar, Max e Bernardo, um fortíssimo obrigado. Ditto para os meus amigos de longa data que muito me marcaram, Serafim, Boquinhas, Alves e Cláudia. Um grande abraço.

À Vilborg muito obrigado por tudo de bom que me trazes, tens trazido, e que o futuro trará. Três tempos verbais que por esta altura já dominaste!

Finalmente, obrigado àqueles que sempre me deram e darão até ao fim aquela força, conforto e tranquilidade quando tudo parece tão difícil. À minha querida família, Mãe, Ricardo, avó Mita, avô Mões, avô Zé e tia Natália. Nunca ambicionaram mais nada de mim que não a minha simples felicidade.

This work was supported by the Portuguese Foundation for Science and Technology, FCT, under the grant SFRH/BD/85501/2012.

Pedro Costa
Lisbon, May 2017

CURRICULUM VITÆ

PERSONAL INFORMATION

FULL NAME: Pedro Simões Costa

BIRTH DATE: 15-06-1989

NATIONALITY: Portuguese

EDUCATION

2013-2017: PhD Research Scholar in the Laboratory for Hydro & Aerodynamics,
Process & Energy Dpt., Delft University of Technology, The Netherlands.

2011-2012: MSc in Mechanical Engineering, Instituto Superior Técnico, Portugal;
ERASMUS Exchange Student, Delft University of Technology, The Netherlands
(in 2011, for six months).

2007-2010: BSc in Mechanical Engineering, Instituto Superior Técnico, Portugal.

LIST OF PUBLICATIONS

- [7] J. Brändle de Motta, P. Costa, J. J. Derksen, L.-P. Wang, W.-P. Breugem, J.-L. Estivaleres, S. Vincent, E. Climent, P. Fede, P. Barbaresco, and N. Renon. “Assessment of methods for fully resolved simulations of particle-laden turbulent flows.” In: (*in preparation*) (2017)
- [6] P. Costa, F. Picano, L. Brandt, and W.-P. Breugem. “Finite size effects in dense turbulent wall-bounded transport of neutrally-buoyant spheres.” In: *Journal of Fluid Mechanics* (*under review*) (2017)
- [5] I. Lashgari, F. Picano, P. Costa, W.-P. Breugem, and L. Brandt. “Turbulent channel flow of a dense binary mixture of rigid particles.” In: *Journal of Fluid Mechanics* 818 (2017), pp. 623–645
- [4] M. N. Ardekani, P. Costa, W.-P. Breugem, F. Picano, and L. Brandt. “Drag reduction in turbulent channel flow laden with finite-size oblate spheroids.” In: *Journal of Fluid Mechanics* 816 (2017), pp. 43–70
- [3] P. Costa, F. Picano, L. Brandt, and W.-P. Breugem. “Universal scaling laws for dense particle suspensions in turbulent wall-bounded flows.” In: *Physical Review Letters* 117.13 (2016), p. 134501
- [2] M. N. Ardekani, P. Costa, W.-P. Breugem, and L. Brandt. “Numerical study of the sedimentation of spheroidal particles.” In: *International Journal of Multiphase Flow* 87 (2016), pp. 16–34
- [1] P. Costa, B. J. Boersma, J. Westerweel, and W.-P. Breugem. “Collision model for fully resolved simulations of flows laden with finite-size particles.” In: *Physical Review E* 92.5 (2015), p. 053012